Self-interference 3D localization microscopy in the near-infrared for deep tissue single-particle tracking

Karen Caicedo Santamaria

THÈSE PRÉSENTÉE

POUR OBTENIR LE GRADE DE

DOCTEUR
DE L'UNIVERSITÉ DE BORDEAUX

ECOLE DOCTORALE DES SCIENCES PHYSIQUES ET DE L'INGENIEUR

LASERS, MATIÈRE ET NANOSCIENCES

Par **Karen CAICEDO**

Microscopie de localisation 3D par auto-interférence dans le proche infrarouge pour le suivi de particules uniques dans les tissus profonds

---

Sous la direction de : **Laurent COGNET**

Soutenance le 16 mars 2023

Membres du jury :

Mme. Catherine TARDIN	Maîtresse de Conférences UTIII Institut de Pharmacologie et de Biologie Structurale	Rapporteur
M. Mathieu COPPEY	Directeur de Recherche CNRS Institut Curie	Rapporteur
Mme. Cécile ZAKRI	Professeure UB Centre de Recherche Paul Pascal	Présidente
Mme. Melissa INFUSINO	Professeure USFQ Universidad San Francisco de Quito	Examinatrice
M. Pierre BON	Chargé de Recherche CNRS Institut de Recherche XLIM	Examinateur
M. Laurent COGNET	Directeur de Recherche CNRS Université de Bordeaux	Directeur

To my mom

Acknowledgments

This manuscript represents the hard work I performed during more than three years of my life. During that time, I not only learned about science, but also about life and people, about how to overcome problems, and how to become a better person. I want to thank God for letting me experience this crazy thing called life. I hope you give me the strength to be loving even when is painful, and cheerful even when there is only suffering. I want to thank my mom for being always by my side. You are one of the kindest people I've ever known, and from you I learned that serving others is the best purpose I can give to my life. You are the best mom I could have ever had. I love you. I want to thank to my grandparents, Estuardo and Azucena, who are my most precious treasure. Thank you for loving me so much and raising me as your own kid. Thank you for having dedicated your life to the family and educating us with so many good values. I love you. Thank you to all my family for being so supportive, especially during the hard times.

I also want to thank my supervisors, Laurent and Pierre, for had given me the opportunity to be part of this project. Thank you Laurent for giving shape to the project and teaching me so many lessons. Thank you Pierre for the discussions you had with me where I learned so much. Thank you to all the jury members who took time to read my thesis, and be part of my defense.

Thank you to my best friends: Carla, Katherine, Maria Gracia, Apolline, Blanca, Marco, and Naveen. You are my chosen family. I love you all for the unique people you are, each of you with a wonderful heart. Thank you to all my friends and colleagues: Alberto, Somen, Adeline, Benjamin, Enakshi, Chiara, Akhtar, Antony, Quentin, Aurelien, Cami, Guillaume, and Jean Baptiste. You made my days in the lab. Life was more fun with you. Thank you to all the staff in LP2N for helping me every time I needed a hand with something. Thank you to Alessandro, Melissa, Ashod and Dario for always making me love science. I admire you so much.

Abstract

Fluorescence microscopy has achieved over the last decade super-resolution localization of single emitters with numerous applications in biological imaging. However, dynamic 3D localization of single emitters at depth in living biological tissues remains a challenge. A few years ago, our team developed the SELFI method (self-interference 3D super-resolution microscopy), allowing the 3D localization of single molecules in specimens and multicellular tissues in the visible wavelength range. In this thesis, we extend the applicability of SELFI in the near-infrared (NIR) region for dynamic studies, where the fluorescence of single-walled carbon nanotubes (SWCNT) is intense. SWCNTs are indeed used as fluorescent probes for dynamic studies in deep biological tissue, as they allow excellent tissue penetration, low light scattering and reduced tissue absorption. The objective of this work is to develop NIR SELFI for single particle tracking applications using SWCNTs in living brain tissue. SELFI uses a diffraction grating placed in the optical path of the sample image, generating an interference pattern without significant spreading of the intensity distribution generated by the image of a point emitter. A single image obtained with NIR SELFI then contains two independent pieces of information: the intensity distribution to extract the lateral super-localization of the emitter and the curvature of the wavefront (provided by the interfringes) to obtain the axial super-localization of the emitter. To adapt SELFI to the super-localization of single SWCNTs, we designed and implemented an optical system adapted to near-infrared emission. The experiments performed allowed to obtain 3D resolutions of about 50 nm considering emitters at 985 nm. We then performed the 3D tracking of individual SWCNTs at video rate in complex environments, including agarose gels, before applying the method in organotypic rat brain slices.

Résumé

La microscopie de fluorescence a réussi à atteindre au cours de la dernière décennie la localisation super-résolutive d'émetteurs uniques avec de nombreuses applications en imagerie biologique. La localisation dynamique en 3D d'émetteurs et en profondeur dans des tissus biologiques vivants reste cependant un défi. Il y a quelques années, notre équipe a développé la méthode SELFI (self-interference 3D super-resolution microscopy), permettant la localisation 3D de molécules uniques dans des spécimens et des tissus multicellulaires dans le domaine de longueurs d'onde visibles. Dans cette thèse, nous étendons les capacités de SELFI dans la région du proche infrarouge (NIR) pour des études dynamiques, où la fluorescence des nanotubes de carbone monoparois (SWCNT) est intense. Les SWCNT sont en effet désormais utilisés comme sondes fluorescentes de mobilité des tissus biologiques en profondeur, car ils permettent une excellente pénétration des tissus, une faible diffusion de la lumière et une absorption réduite par les tissus. L'objectif de ce travail est ainsi de développer le SELFI NIR pour des applications de suivi de particules uniques utilisant les SWCNTs dans des tissus cérébraux vivants. SELFI utilise un réseau de diffraction placé sur le chemin optique de l'image de l'échantillon, générant un motif d'interférence sans étalement significatif de la distribution d'intensité de l'image d'émetteurs ponctuels. Une seule image obtenue avec SELFI NIR contient alors deux informations indépendantes : la distribution d'intensité pour extraire la super-localisation latérale de l'émetteur et la courbure du front d'onde (fournie par les interfranges) permettant d'obtenir la super-localisation axiale de l'émetteur. Pour adapter SELFI à la super-localisation de SWCNT uniques, nous avons conçu et mis en œuvre un système optique adapté à une émission dans le proche infrarouge. Les expériences réalisées montrent que la résolution 3D obtenue avec le SELFI NIR est d'environ 50 nm pour une émission autour de 985 nm. Nous avons ensuite effectué le suivi 3D de SWCNTs individuels à une fréquence vidéo dans des environnements complexes, dont des gels d'agarose, avant d'appliquer la méthode dans des tranches de cerveau organotypiques de rat.

Contents

Introduction

In many branches of contemporary research, there is a critical need to comprehend the specific structural characteristics and dynamical behavior of nano-architectures through microscopical imaging. However, optical microscopy has long been facing a fundamental constrain in resolution: the *diffraction limit*, which does not allow to produce images of observed specimens with dimensions below ∼200 nm (i.e., $\sim \lambda/2$, with λ the emission wavelength), down to the nanometer scale. Fortunately, with the advent of super-resolution microscopy techniques, among them *single-molecule localization microscopy* (SMLM), the resolution of optical microscopes has recently been pushed down to nanoscale sizes in an effort to enable contactless and distant inspections of specimens in their natural surroundings, including live samples. SMLM is now revolutionizing the fields of physics, chemistry, biology and the bio-medical sciences.

SMLM can be employed in two branches of application: single-molecule super-resolution imaging (SMSRI) and single-particle tracking (SPT). SMSRI essentially uses the photocontrolled emission of fluorescent molecules in order to gain spatial sparsity, and generate images of objects at the molecular level [1]. Whereas SPT primarily involves recording single-particle diffusion in a continuous way in long video frames, followed by super-localization analysis of the single emitter in each video frame and reconstruction of its trajectory with specialized algorithms [2,3]. The collection of localization points along trajectories can then be used to deduce dynamically super-resolved images of the local environment explored by the particles.

The design, development and application of SMLM approaches dedicated to the use or study of synthetic nanomaterials is a vibrant field of research and has shown great promise for several types of nanomaterials, such as spherical nanoparticles (e.g. semiconductor quantum dots, polimer particles, gold or silver nanoparticles, etc.), 2-D hexagonal boron nitride (h-BN), supramolecular polymer-based nano-assembly, gold nanorods [4–8] and single-walled carbon nanotubes (SWCNTs). For many nanomaterials, however, SMLM is challenging due to the limited photoluminiscent brightness and high photobleaching properties of the nano-objects, as well as the difficulty of labeling them with fluorophores. In contrast, SWCNTs display rich optical (no photobleaching or self-blinking), physical and chemical potentialities together with unique

sensing capacities. They are also versatile near-infrared (NIR) emitters covering the biological/telecom windows. As a consequence, the characterization of SWCNTs with super-resolution techniques in terms of exciton localization, quenching or luminescent defects, and more generally photophysical properties, has emerged and triggered strong interest due to the implications for many applications in materials science, nanoelectronics, photonics, quantum information and biophotonics, for example. Additionally, it is important to note that many super-resolution microscopy approaches applied to other nanomaterials mentioned above were typically constrained to the study of some of the internal structures of these nanostructures, while SWCNTs have shown the supplementary ability to generate super-resolution data for complex environments and in the NIR regime. This makes them particularly attractive for high-resolution bio-imaging.

Nevertheless, all the efforts described above have been mostly limited to the two lateral dimensions of localization, being the third dimension a challenge still to overcome up to this point, especially in complex and thick samples. The studies performed with 2D microscopy are incomplete because they lack to provide the 3D complexity of the environments studied. The need to have a 3D view of microscopical and nanoscopical structures is unequivocal as it resembles more to reality. This was the motivation for our research team to have developed a new 3D SMSRI technique which allows us to obtain a more accurate picture of the topology and dynamics of the nanostructures explored: Self-interference (SELFI) 3D localization microscopy for visible wavelengths [9], and NIR in the present thesis project. More precisely, in this thesis, SELFI NIR was extended to applications on SPT of carbon nanotubes inside biological tissue.

In the following pages, we briefly review the different SMSRI techniques in 2D. Then, we present the research performed by using 2D SPT of SWCNTs for biological tissue investigations. After, we show some of the 3D SMSRI techniques available as well as their drawbacks when it comes to fluorescence microscopy in bio-tissue in the NIR domain.

A brief overview of 2D SMSRI techniques

The different SMSRI techniques are the following: (direct) stochastic optical reconstruction microscopy ((d)STORM) [10, 11] which involves stochastically emitting molecules, photoactivated localization microscopy (PALM) [12–14] based on the photoconversion of autofluorescent proteins, and points accumulation for imaging in nanoscale topography (PAINT) [15] involving the imaging of dyes that transiently bind and quickly dissociate from their targets. SMSRI methods require stochastic on/off photodynamics (blinking events) for specific fluorophores, reflecting the limitations in the choice of probe molecule. However, all these SMSRI techniques today

share one limitation, which is that they use fluorescent molecules (common organic labels or autofluorescent proteins) emitting in the visible and far-red ranges (400–750 nm) of the electromagnetic spectrum. In fact, SMLM has rapidly expanded the super-resolution domain thanks to the design and development of a variety of photoswitchable emitters, all in the visible or far-red region. This limitation attracted a lot of attention in the scientific community and encouraged the identification and development of NIR emitters [31,32]. In this context, SWCNTs are appealing candidates as one of the most emblematic classes of NIR nanoprobes.

Single-particle tracking of SWCNTs inside biological architectures

It is well-established that information about the local structural architecture of complex environments can be better revealed at the nanoscale regime by single-particle tracking (SPT) [16, 17] compared to other fluorescence microscopy methods such as fluorescence correlation spectroscopy [18, 19] or fluorescence recovery after photobleaching [20], which offer only ensemble averaging information. In fact, SPT can be seen as a parent methodology of SMLM [21, 22]. SPT primarily involves recording single-particle diffusion in a continuous way in multiple video frames, followed by super-localization analysis of the single emitter in each video frame and reconstruction of its trajectory with specialized algorithms [2, 3]. The collection of localization points along trajectories can then be used to deduce dynamically super-resolved images of the local environment explored by the particles, as in SMSRI. For instance, SPT has been used to examine the random diffusion of single dye molecules in order to reveal dynamic information from various processes and systems, such as in crystalline hosts [23], ordered mesoporous structures [24, 25], catalytic conversions [26] and heterogeneous biological architectures [27, 28].

In this context, the development of SPT using SWCNT-based NIR video microscopy has allowed novel discoveries in different systems, including isolated cells and thicker 3D biological tissues [27–29]. In the following lines, we focus on one of the main topics of research in our team, which is the application of SWCNTs with SPT for the exploration of the brain extracellular space (ECS), where combining SWCNT assets and a super-resolution methodology has been the key feature.

The brain ECS, which is the space in between brain cells, is crucial as it occupies one fifth of the brain's volume yet its morphology and physiology are still poorly understood. Through the super-resolved tracking analysis of SWCNTs diffusing in the brain ECS, our team has revealed the topology and diffusion properties of the ECS in different brain conditions (see Fig.1) [28, 30, 31].

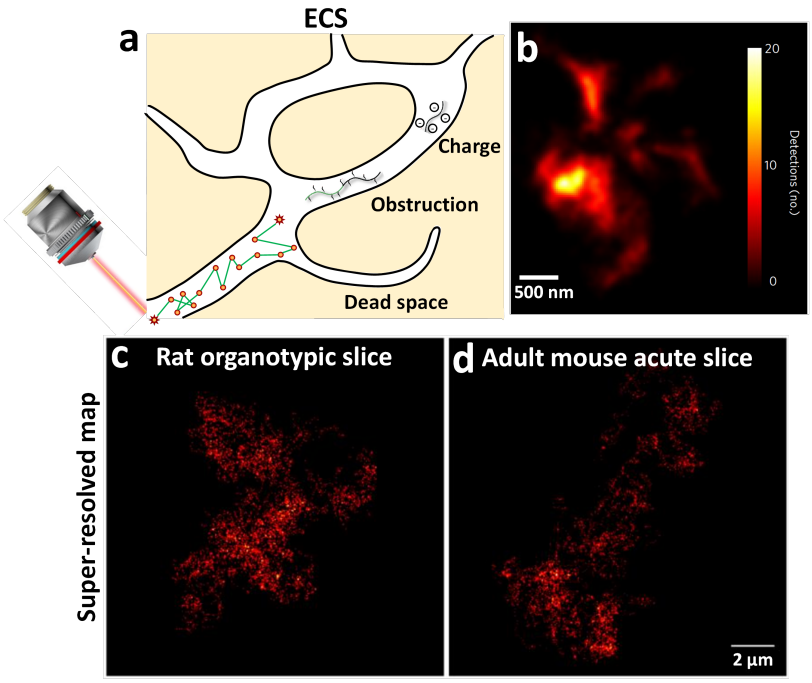

Figure 1: Mapping extracellular space (ECS). (a) Schematic depiction of SWCNTs' diffusion in ECS. Connecting lines in the trajectories do not depict the exact diffusion path but are just for visualizing purposes. (b–d) Diffusion-analyzed super-resolved images of individual SWCNTs in the ECS of a rat organotypic slice and an adult mouse acute slice; (b) reproduced with permission from [28] copyright 2017, Springer Nature and (c,d) reproduced with permission from [30] copyright 2020, Elsevier.

SWCNTs diffusing in ECS were super-localized and trajectories containing large amounts of information reconstructed. SWCNT tracking exhibits three decisive advantages over other emitters for such applications: first, their NIR emission perfectly matches the transparency window of biological tissues, allowing biological tissue to be imaged at depth (several tens of micrometers, i.e., several cellular layers). This is a stringent requirement when the elucidation of tissue architectures is targeted. Second, the high brightness and perfect photostability of individual SWCNTs' photoluminiscence allows ultra-long trajectories to be recorded (tens of thousands of points imaged at video rate). Third, the 1D character of the nanotubes is a unique feature that allows them to enter tiny channels of complex structures [32] thanks to their nanometer diameters while spending enough time there to explore their environment extensively thanks to their lengths (100 nm to micrometer lengths). As a result, trajectories contain an extensive number of localizations in local environments, enough to reveal both dimensions and diffusion properties. Super-resolved maps can thus be computed by cumulating the nanotube localizations, as in SMLM methodologies (Fig.1.c, d). Godin et al. [28] demonstrated this approach in acute rat brain slices with a sub-wavelength precision of ∼50 nm. They could then estimate the local dimensions of

the brain ECS by analyzing the "shape" of the local area explored by the SWCNTs. A refined, non-parametric method to analyze such local areas was later proposed by Paviolo et al. [30]. From the mean-square displacement analysis, the instantaneous diffusion coefficient could also be calculated. Comparison of rat organotypic tissue with mouse acute slices led to the revelation of the highly heterogeneous and tortuous features of ECS at the nanoscale level.

In another work, Soria et al. [31] investigated brain ECS modifications in the context of α-synuclein-induced neurodegeneration. For this, dopaminergic neuronal loss was induced in the substantia nigra of adult mice through unilateral inoculation of Lewy body fractions derived from Parkinson's patients [33]. SWCNTs were tracked in acute slices of Lewy body-inoculated mice with a subwavelength precision of around 50 nm. Local, instantaneous, super-resolved diffusivity maps of ECS were created for both healthy and degenerative substantia nigra displaying heterogeneity in the ECS, as confirmed by electron microscopy in fixed tissues. The quantitative analysis showed that the diffusion in healthy brains was slower than in Lewy body-inoculated pathology mice. This work demonstrated that hyaluronan plays the central role for the variations in the ECS microenvironment and can have a severe impact on brain pathologies. This novel knowledge based on the combination of carbon nanotube imaging and super-resolution methodologies opens the route for the investigation of the physiological and pathological factors leading to different neurodegenerative diseases such as Alzheimer's, Parkinson's and Huntington's diseases.

The strategies discussed above can lead the way to applications involving other 1D and 2D nanostructures, including semiconducting nanocrystals, h-BN and quantum dots, for instance [34–36]. Although many technical and equipment challenges have already been successfully overcome in the quest towards further improvement of spatiotemporal resolution, 3D spatial super-resolution has been an issue to this day. Reason why we have worked on SELFI as an approach to 3D SMLM during the course of the present thesis project, more precisely oriented towards SPT of SWCNTs in complex biological media, which we foresee as the key for better understanding of biological environments [9, 37] and complex nanostructures.

3D single-molecule super-resolution imaging techniques

In the present section, we review some of the most commonly used 3D super-resolution techniques already existent, their different working principles, advantages and drawbacks.

PSF engineering methods

One way to recover the axial position of an emitter is by introducing an optical aberration along the optical axis so that the PSF has deterministic shapes for the different z positions. One technique is to add a cylindrical lens between the objective

and the tube lens in the microscope producing astigmatism from where it is possible to differentiate each axial position [11, 38], as observed in Fig.2.a. This technique reaches a lateral resolution of 10 nm and an axial resolution of 20 nm for 1000 detected photons. Another popular PSF engineering methods is the Double Helix (DH). DH consists in adding a phase mask in the Fourier plane at the microscope exit [39]. Fig.2.b shows the DH setup. The phase mask changes the PSF shape such as now it has two lobes forming a double-helix shape when reconstructing the PSF in 3D. The emitter's axial position is obtained from the rotation angle formed by the two lobes. The resolution reached with this method is ∼10 nm laterally, and ∼20 nm axially [37]. Nevertheless, these methods might not be optimal when working deep into biological structures as tissue itself introduces aberrations, making it more difficult to understand whether the aberration comes from the sample or the optical setup. Additionally, broadening the PSF or dividing its photons budget into two is not ideal when working in fluorescence microscopy as the photon budget is already low.

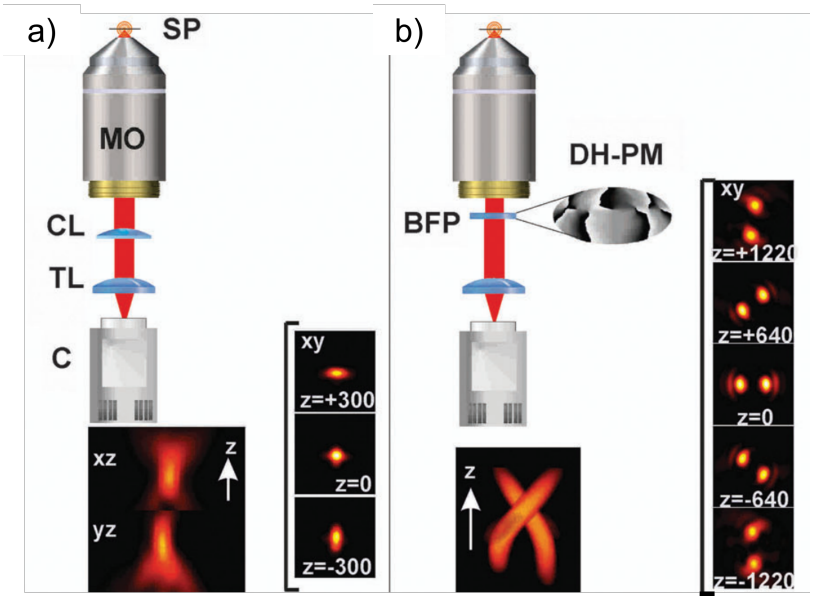

Figure 2: PSF engineering methods for 3D SMSRI. a) The astigmatic-based 3D imaging setup consists in adding a cylindrical lens to the optical path. The axial position is encoded in the astigmatism added to the PSF. (b) The double helix PSF shaping technique consists of a phase mask placed in the Fourier plane at the microscope exit to give the PSF a two-lobes shape where the axial position of the emitter is encoded in the inclination of the lobes (figure extracted from Phys. Chem. Chem. Phys. 2014 [40]).

Multiple plane imaging methods

Imaging the emitter in several focal planes is one way to acquire a precise 3D localization. By doing this, we may eliminate the uncertainty caused by the PSF's

symmetry with respect to the plane of focus and take advantage of the PSF's variance along z. Splitting the fluorescence beam in half and collecting the fluorescence on two cameras conjugated to two distinct planes of the sample is one example of multiplane imaging for 3D localization [41, 42]. This method, called biplane imaging is shown in Fig.3.a. We also have the multifocus microscopy approach, which consists in using a phase mask to split the emission into nine planes, enabling a full reconstruction of the 3D PSF as well as accurate z localization [40]. However, since the signal comming from the fluorescent sample is split into several imaging planes, this method is limited to very bright emitters.

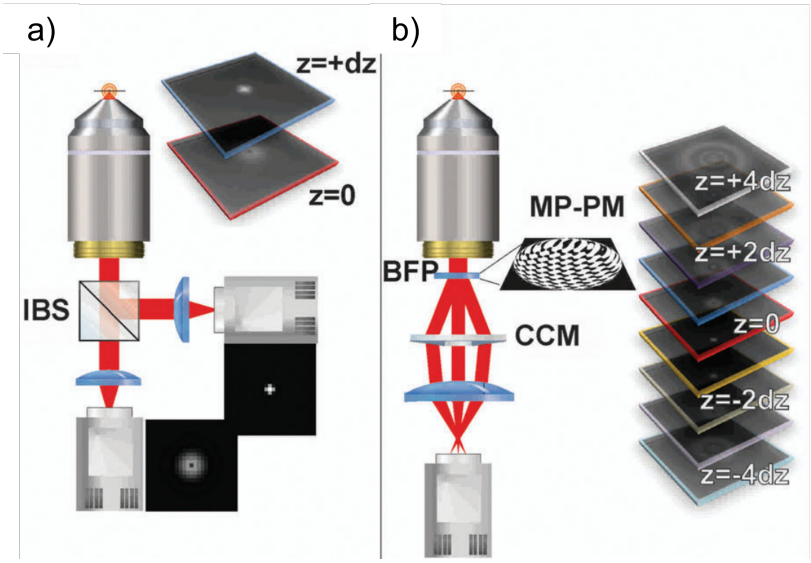

Figure 3: Multiple plane imaging methods for 3D SMSRI. a) The biplane imaging configuration consists of an intensity beam splitter which divides the emission into two, and the cameras are positioned so that they image two distinct focal planes of the object space. This allows for a precise axial localisation of the emitter due to the sampling of the PSF on two separate focal planes. b) The multifocus microscopy method divides the emission into nine central orders using a phase mask positioned at the microscope exit. The different diffraction orders are adjusted for the various defocusing powers, allowing for a full three-dimensional sample of the PSF and accurate axial localization (figure extracted from Phys. Chem. Chem. Phys. 2014 [40]).

Interferometric imaging methods

Self-interference, i.e. interference of the fluorescent beam with itself, is another way to obtain the axial localization of the emitter. This is the principle behind the approach presented in this thesis, and detailed in chapter 1, but also behind iPALM (interferometric Photoactivated Localization Microscopy) [43]. Two objectives are used in iPALM's optical setup in a 4Pi configuration [44] to collect the fluorescence released by a single molecule.

The two fluorescent beams captured by the two objectives are merged, as shown in Fig.4, to interfere in three distinct ways on three detectors using a spectrum beam splitter. The amplitudes of the interferences gathered on each camera are used to calculate a molecule's axial location by using a calibration signal. A molecule emitting 1500 photons may be localized with an accuracy of less than 10 nm for a photon budget thanks to the iPALM. However, this method is constrained by the 225 nm depth of field. The 4Pi-SMS (4Pi-single marker switching) method, which may be used to image live samples, increases the depth of field to 1 μm [45].

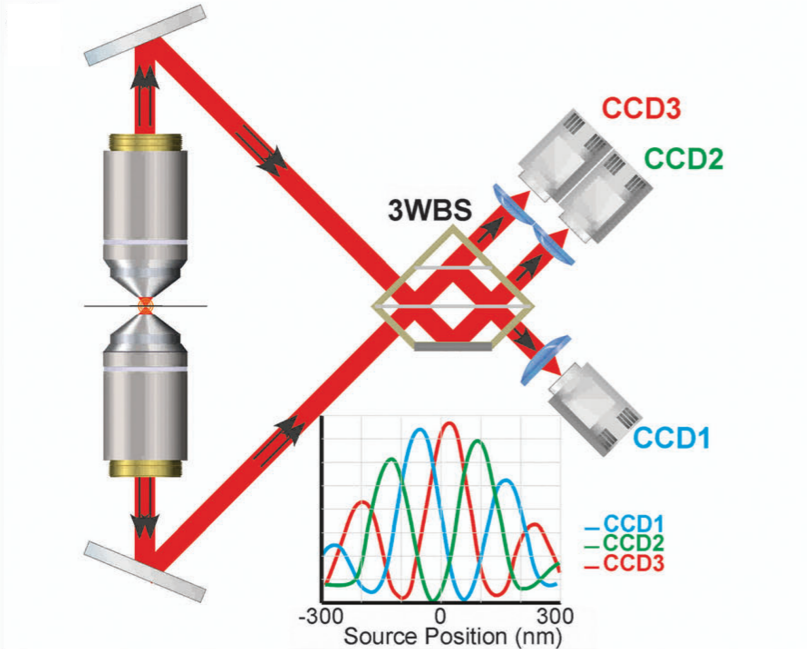

Figure 4: The iPALM setup is an example of interferometric imaging method. The light coming from the sample and gathered by the two objectives interferes by using a three-way beam splitter. The signal captured by the three cameras is afterwards compared to a calibration signal to determine the emitter's axial position (figure extracted from Phys. Chem. Chem. Phys. 2014 [40]).

Supercritical angle fluorescence (SAF) technique

Another approach to determine the emitter's axial position is to use the sample-coverslip refractive index mismatch in the interface and measure the coupling of emitted light into the coverslip. Following the Snell-Descartes law, any light emitted at an angle greater than the critical angle ($\theta_c \sim 61^\circ$ relative to the vertical for a water/glass interface) for emitters farther away that λ from the coverslip will be completely internally reflected back into the sample. λ being the emission wavelength. However, light out of the critical angle, i.e. "supercritical" light, couples to the coverslip and can be collected by using high numerical aperture objectives. By putting an annular filter in the back focal plane, the supercritical and "undercritical" components of the

fluorescence can be distinguished, and axial position can be determined without suffering a significant signal loss as in the total internal reflection fluorescence (TIRF) case by comparing the total fluorescence to the undercritical-only fluorescence [37]. This method is called supercritical angle fluorescence (SAF), and it is portrayed in Fig.5. This technique has been proven to work for in vitro 3D origami nanostructure research and single-molecule imaging extremely close to the cell boundary [37, 46, 47].

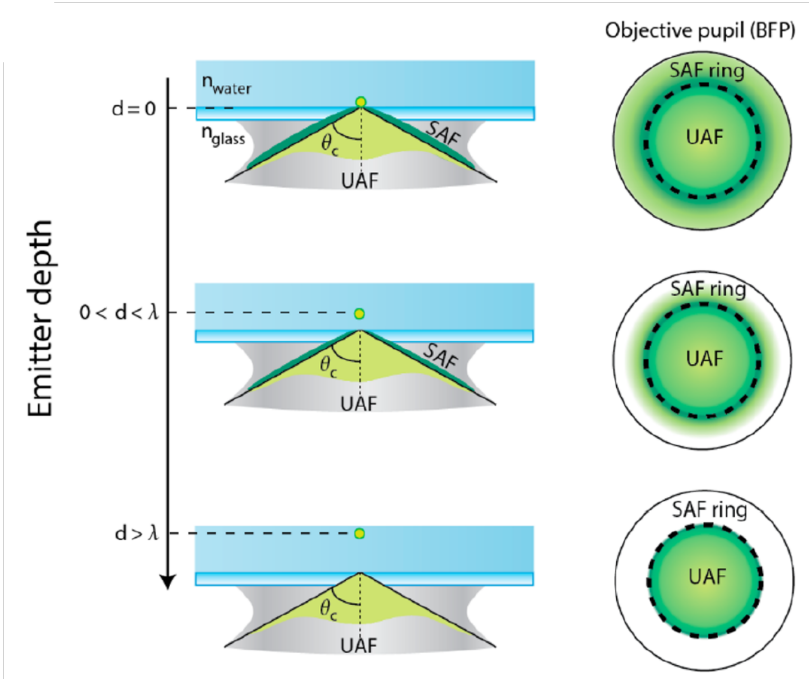

Figure 5: The supercritical angle fluorescence (SAF) consists in coupling emitters close to the coverslip and collect the SAF as well as "undercritical" fluorescence. Axial position determination is possible due to the fast decline of the supercritical to undercritical light ratio as the emitter is further from the coverslip (figure extracted from Chem. Rev. 2017 [37]).

As we just saw through all the methods discussed above, nanoscopy enables access to the precise localization of molecules in biological materials, whether they are living or not. Nevertheless, these complex systems have been researched on the single-cell level or on the first cell layers of a tissue sample so far, but in order to understand *in vivo* environments, it is vital to take into account cells in their natural state, i.e. inside a three-dimensional structure like an organ or organelle. Although there have been techniques such as chemical clarity of tissue [48] and expansion microscopy [49] that, when applied together, make it possible to study entire organs, the tissue modification makes it incompatible with imaging living samples.

Super-resolution microscopy can be used on tissue samples without the need to modify it. However, the intricacy of biological tissue hinders the fluorescence signal's effective transmission given that dense biological samples are not transparent in the

visible range of wavelengths (not so in the NIR), as it will be discussed in more detail in chapter 1. As a result, the current 3D super-resolution techniques are limited by the complexity of bio-tissue. As fluorescent signal is dim, it becomes complex to use multi-planar microscopy which separates the photons on the different imaging planes. And the aberrations present in the sample make it difficult to use PSF shaping techniques to localize molecules deep in the tissue given that the presence of these aberrations alters the necessary deterministic shaping for localization.

In this thesis, we present a 3D super-localization technique to perform single-molecule imaging deep within intact biological tissue: SELFI. More precisely, we extend the capability of SELFI to the near-infrared region where SWCNTs are strong emitters. SWCNTs are indeed now used as fluorescent probes of biological tissue at depth, as they allow excellent tissue penetration, low light scattering, and reduced absorption by the tissue. The aim of this work is to develop NIR SELFI for single-particle tracking applications of SWCNTs in live brain tissues.

Manuscript organization

This manuscript is organized in three chapters. The first chapter introduces SELFI as a technique to obtain 3D super-resolution localization. We first explain the theoretical working principle behind SELFI. After, we discuss the experimental aspects to design the SELFI optical setup. Then, we show the performance characterization of SELFI by showing results on the localization of near-infrared and far-red fluorescent emitters.

The second chapter explains how the analysis method works to obtain 3D super-resolution from SELFI images. First, we show how we model SELFI images. After, we discuss how the parameters setting is performed as well as how lateral super-localization is done. Then, we exhibit how to obtain the axial localization of single emitters. Finally, we briefly discuss about an alternative method on how to achieve axial localization through machine learning.

The third chapter consists on the applications of near-infrared SELFI to carbon nanotubes. We first present a brief overview of SWCNTs and their properties. After, we show 3D super-resolution localization of immobilized SWCNTs. Finally, we expose the results we obtained when using SELFI for 3D single-particle tracking of SWCNTs in different media, including living brains.

Chapter 1

Self-interference 3D super-resolution in the near-infrared regime

Fluorescence microscopy in conjunction with super-localization has been advantageous when it comes to study structures of biological systems with unprecedented sub-wavelength precision. This task is now well mastered in two dimensions, but in three dimensions, super-localization remains challenging. In fact, the recovery of localizations along the axial dimension is currently restricted to studies within isolated cells or the first cellular layer in multicellular samples, as well as studies in transformed tissue [49, 50]. Nevertheless, three dimensional super-resolution microscopy arises from a profound quest to better understand the features and functioning of biological configurations. In particular, one area of application which is of interest in our research team is the brain extracellular space [28,30–32,51,52]. However, imaging biological tissue always carries issues to overcome. On one hand, there are sample limitations caused by the damage produced when the organic body to study, such as the brain, is sliced into sections to obtain samples hundreds of microns thick, Fig.1.1.a. The cells on the sample's surface die and the superficial layer of the sample is no longer representative of healthy tissue. Therefore, there is a need to image far from the superficial layers to reach untouched living cells [28]. On the other hand, there are optical limitations induced by the sample on the light passing through it, such as aberrations, scattering and absorption, Fig.1.1.b. Consequently, when fluorescent nanoparticles are introduced into the tissue, their emission suffers photon loss. All these challenges have been the motivation for our research team (Nano-BioMicroscopy at LP2N) to develop a novel three dimensional super-resolution microscopy technique, self-interference (SELFI), insensitive to aberrations and maximizing the collection of signal.

Another important concern taken into account during the development of this

thesis is which fluorescent nanoparticles to use since our goal is to go as deep into the tissue as possible. Subsequently, we must consider the *tissue transparency window*, defined as the range of wavelengths where light has its maximum penetration in biological tissue, which corresponds to the near-infrared regime [53–55]. Due to these reasons, we have decided to use single-walled carbon nanotubes, which happen to be strong emitters in the NIR [56,57]. More precisely, for (6,5) SWCNTs, the emission is $\sim$ 985 nm, and are used for deep tissue imaging in thesis project [28,30,58]. SWCNTs are indeed now used as fluorescent probes of biological tissue at depth, as they allow excellent tissue penetration, low light scattering, and reduced absorption by the tissue. Fig.1.1.c shows the absorbance spectrum of brain slices (black) in contrast to the photoluminiscence spectrum of one SWCNT in the extracellular space (purple) when excited with an 845 nm laser (red), see chapter 3 for more details [28]. As observed, both the SWCNT emission as well as its excitation are not absorbed by the brain. Therefore, nanotubes can be well excited when being inside multicellular structures, and their emission is successfully transmitted as it propagates through the tissue.

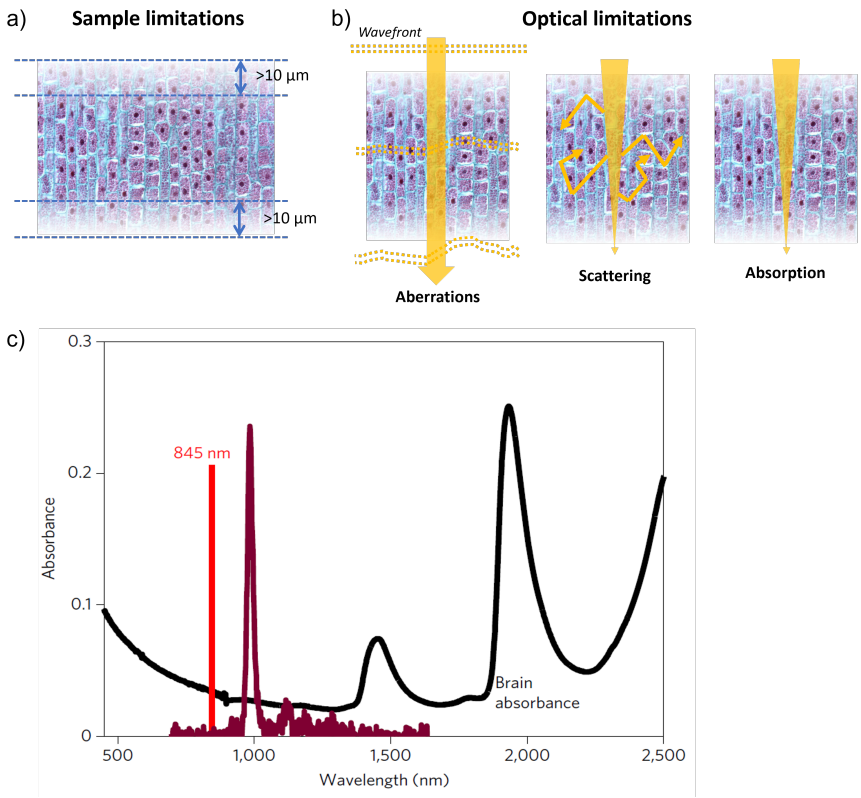

Figure 1.1: Constraints during biological tissue imaging. a) Sample limitations due to surface damaged tissue during the slicing process. b) Optical limitations, such as aberrations, scattering and absorption of the light inside the tissue. c) Absorbance spectrum of 1 mm thick brain slice (black) and photoluminescence spectrum of a single (6,5) SWCNT in the extracellular space (purple) on 845 nm laser excitation (red) (figure extracted from Nature Nanotechnology, 2017 [28]).

At first, SELFI was specifically conceived for emission in the visible range under the context of super-resolution microscopy in fixed tissues [9]. In this work, we have extended SELFI to deep tissue 3D single-particle tracking (SPT) based on NIR emitters, which encompasses specific technical constrains based on the NIR wavelength range. Noteworthy, SELFI applied to SPT in the near-infrared to obtain 3D trajectories is something that has never been done before. Ergo, the final aim of the present thesis project is to redesign and build SELFI to make it suitable for carbon nanotubes for 3D single-particle tracking applications deep into live brain tissue.

In the present chapter, we describe the optical strategy that we use to perform 3D super-resolution localization microscopy in the near-infrared: SELFI NIR. We start by discussing the physical concepts and principles behind 3D super-resolution localization of point-like fluorescent emitters by self-interference. To do so, we explain the role of intensity and phase in localization as they carry the lateral position (x, y) and axial position (z) information, respectively. After, we illustrate how self-interference of electromagnetic waves is generated from a conceptual as well as theoretical point of view. This leads us to the discussion of how to retrieve the 3D localization of a point source from self-interfered signal. Then, we describe the experimental design of SELFI NIR optical setup, and the instrumental considerations to build an optimal optical system. We also explain how to experimentally position the diffraction grating used to produce self-interference. This step is crucial since it determines the quality of the z-localization resolution. Finally, we describe the performance characterization of 3D localization with SELFI. To do so, we have used PbS/CdS (lead (II) sulfide / cadmium sulfide) quantum dots (QDs) emitting in the NIR ($\sim$1040 nm) because, although the final goal is to use SELFI on SWCNTs, QDs are spherical point-like emitters, thus more geometrically simple in contrast to the one-dimensional feature of carbon nanotubes, which is an additional complexity. What is more, the question of which nanoparticles to use is also linked to availability. In particular, during the course of this project, we had access to PbS/CdS QDs, nevertheless, the batch of particles was damaged during the shipping process from the United States (their origin place) to our laboratory in France. All this took place during the Covid-19 crisis, and unfortunately, we could not get a new batch to replace the damaged one due to some difficulties we faced during the pandemic. Therefore, we could not use them for all the tests we envisioned to perform because of their poor brightness in liquids. We only used these QDs when they are immobile and fixed to the coverslip surface. For characterization, TetraSpeck were also used, which are fluorescent nanobeads emitting in the far-red ($\sim$680 nm), opening the possibilities for two-colors (far-red and near infrared) SELFI. The characteristics and specifications of both fluorophores, PbS/CdS QDs and TetraSepck nanobeads are also mentioned.

In summary, three different nanoparticles are used during the course of this thesis

project: PbS/CdS QDs, TetraSpeck, and SWCNTs. For SPT in inert media, we have used HiPco (6,5) SWCNTs coated on DOC. For SPT in deep biological tissue experiments, CoMoCAT (6,5) SWCNTs coated on PLPEG were the ones used. A detailed discussion on SWCNTs in presented in chapter 3. In the following pages, colormaps of excitation versus emission spectra of PbS/CdS QDs (Fig.1.2), TetraSpeck Fig.1.3, and CoMoCAT (6,5) PLPEG SWCNTs (Fig.1.4), are shown.

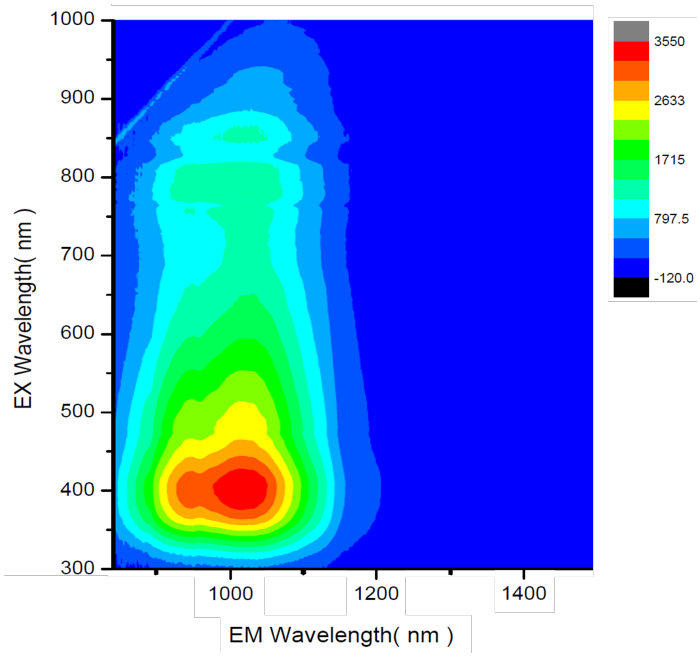

Figure 1.2: Colormap of excitation and emission for PbS/CdS QDs.

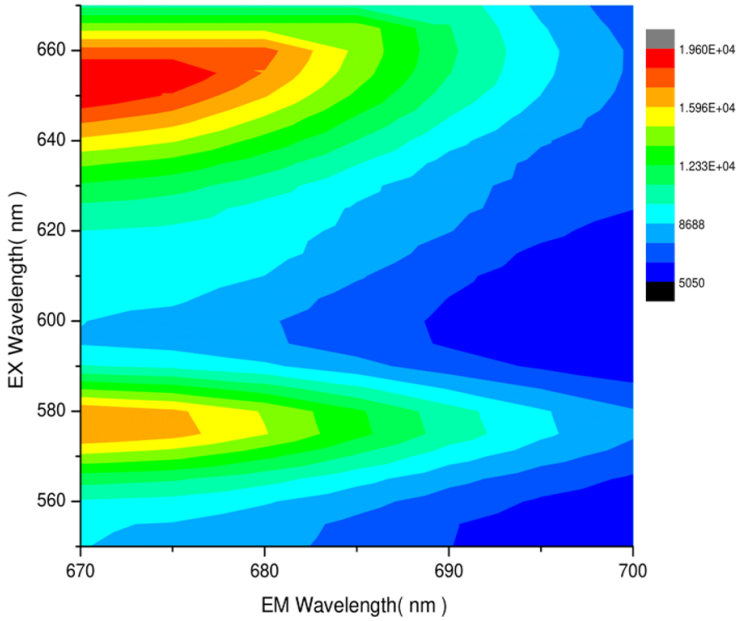

Figure 1.3: Colormap of excitation and emission for TetraSpeck nanobeads.

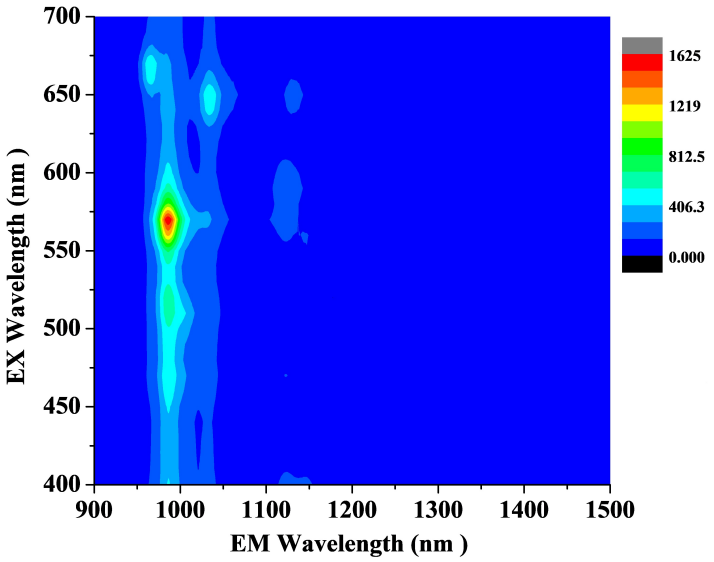

Figure 1.4: Colormap of excitation and emission for pristine CoMoCAT SWCNTs coated on PLPEG.

1.1 Super-resolution localization by self-interference

In this section, we briefly study the working principle of 3D self-interference super-resolution localization. This presentation of SELFI has been inspired by the work performed during the PhD thesis of Jeanne Linarès-Loyez. We explore the correlation between intensity and phase with 3D localization. After, we explain the formation of self-interference from a geometrical and theoretical point of view, and we finalize with how to determine the emitter localization from its self-interfered signal.

1.1.1 Concept of super-localization in two dimensions

The image of a point source seen through any optical device is not the point itself but rather a distribution of intensity called *point spread function* (PSF), and is the three-dimensional diffraction pattern of the light emitted by the object observed. In the case of microscopes, a fraction of the light coming from a point-like emitter in the sample passes through the objective until it reaches the tube lens, which focuses the image of the point source in the image plane. The emitter's light waves diffract and converge at the focal point, resulting in an interference pattern of concentric rings of light encircling a central, bright disk, being this the (x, y) projection of the PSF and called Airy disk. Fig.1.5.a shows two PSF images corresponding to its (x, y) as well as its (y, z) projections. The Airy disk radius, known as the *diffraction limit* (DL),

displayed in Fig.1.5.b, is calculated through the expression

$$DL = \frac{1.22\lambda}{2NA}, \tag{1.1}$$

where λ is the emission wavelength, and NA is the numerical aperture of the objective, which measures the capacity of the objective to collect light. More precisely, since the objective has a finite aperture, there is a maximum angle that limits the light that can actually enter through the objective. The NA is a theoretical parameter, defined on geometrical and optical considerations displayed in Fig.1.6. The NA can be calculated through the expression

$$NA = n \sin\theta,$$

where n represents the refractive index of immersion medium, and θ the angular aperture of the objective.

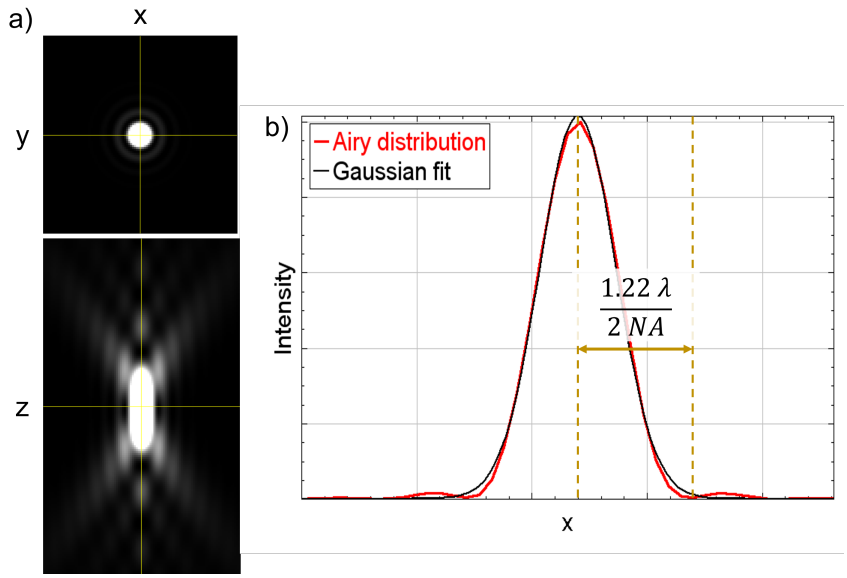

Figure 1.5: a) Simulation of a point spread function of a point-like emitter (λ = 980 nm, similar to SWCNTs) when observed with a microscope of $NA = 1.27$. b) A computer-generated image of an Airy disk distribution of intensity in a PSF in comparison to a Gaussian fit.

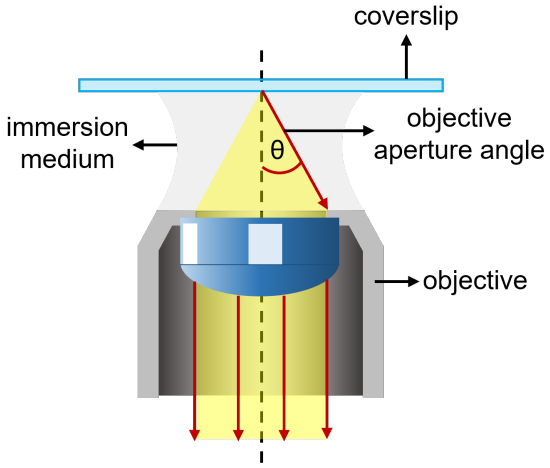

Figure 1.6: Schematic representation of how the light coming from the sample is gathered by the objective. The amount of light collected depends on the objective aperture angle.

A fundamental concept to understand when it comes to microscopy is the resolution of the images produced. The resolution of a microscope is the minimum distance between two object points necessary to distinguish them from one another. And in 1879, it was Rayleigh who suggested a rule, now called the Rayleigh criterion, which states that the image of the points is resolved if the points are separated by a distance equal to Eq.1.1 [3, 59, 60]. Therefore, the PSF dimensions determine how blurry or well resolved is an image produced by any optical system. One can observe from Eq.1.1 that the DL is directly proportional to the emission wavelength, and inversely proportional to NA. Thus, to increase the resolution by decreasing the DL, we have two ways of doing so: by decreasing the wavelength or increasing the NA. Take an optimal example where $\lambda \sim 500$ nm (visible) and $NA \sim 1.22$ (high NA), this gives a resolution of ~ 250 nm. Improving the resolution by means of the emission wavelength and NA has reached its limit. However, there is another way to achieve subdiffraction resolution by using stochastic fluorophore activation and basic data processing, this is known as single-molecule localization microscopy (SMLM) and it will be explained in more detail in the following paragraphs. Experimentally, the resolution is not entirely defined by the Rayleigh criterion since there are some other factors that affect it, such as a poor signal coming from the emitter compared to the amount of noise (represented by the signal-to-noise ratio, defined as the ratio between number of photons in the signal and noise), sampling of the signal in the camera pixels, presence of optical aberrations, optical alignment drift, etc. In fluorescence microscopy, noise may appear in the images due to two different reasons: first, intrinsic shot noise from the signal, i.e. the fluctuations in the flux of photons coming from any source of light, and that follows a Poisson distribution. Second, background noise that can come from different sources, such as the noise in the detector which

contains thermal electrons generated in a sensor and readout noise. We also have background produced by light pollution in the detector, such as ambient light or light from the excitation source. Not to mention the background coming from the sample as well, such as autofluorescence or out-of-focus fluorescence [2, 3, 61].

If we consider the image of a single emitter, one can determine its position with better accuracy than the diffraction limit. To do that, we first approximate and fit the Airy distribution of intensity to a less complex function: 2D Gaussian distribution, as displayed in Fig.1.5.b. We can observe from Fig.1.5.b that the performance of approximation of the PSF to a Gaussian works remarkably good. However, a full description of the PSF function will be discussed in the annex of this thesis. Then, we use a least square fitting to determine the centroid of the Gaussian, which corresponds to the (x, y) position of the point emitter, as is shown in Fig.1.7. The microscopy methods that allow to carry out this process are called SMLM, Fig.1.8.a [37]. SMLM can be used in two sets of applications: one is single-particle tracking (SPT), which consists in localizing a single moving particle over time, being able to reconstruct its trajectory with nanometric resolution, Fig.1.8.b. Other is single-molecule super-resolution imaging (SMSRI), in this case we localize many particles individually while they are separated from one another due to their blinking properties, Fig.1.8.c. Examples of SMSRI techniques are (direct) stochastic optical reconstruction microscopy ((d)STORM) [10,11], photoactivated localization microscopy (PALM) [12–14], points accumulation for imaging in nanoscale topography (PAINT) [15], and other related techniques [4, 62, 63].

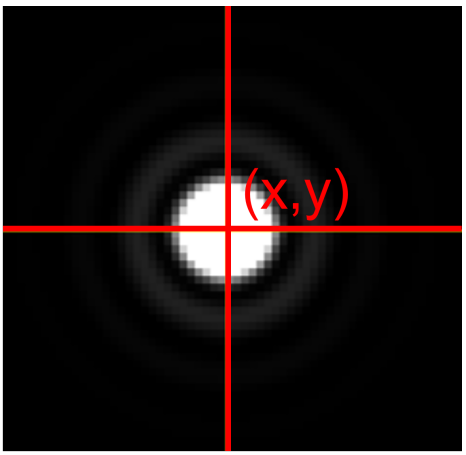

Figure 1.7: The centroid of the 2D Gaussian fitted to the PSF gives the position of the emitter itself.

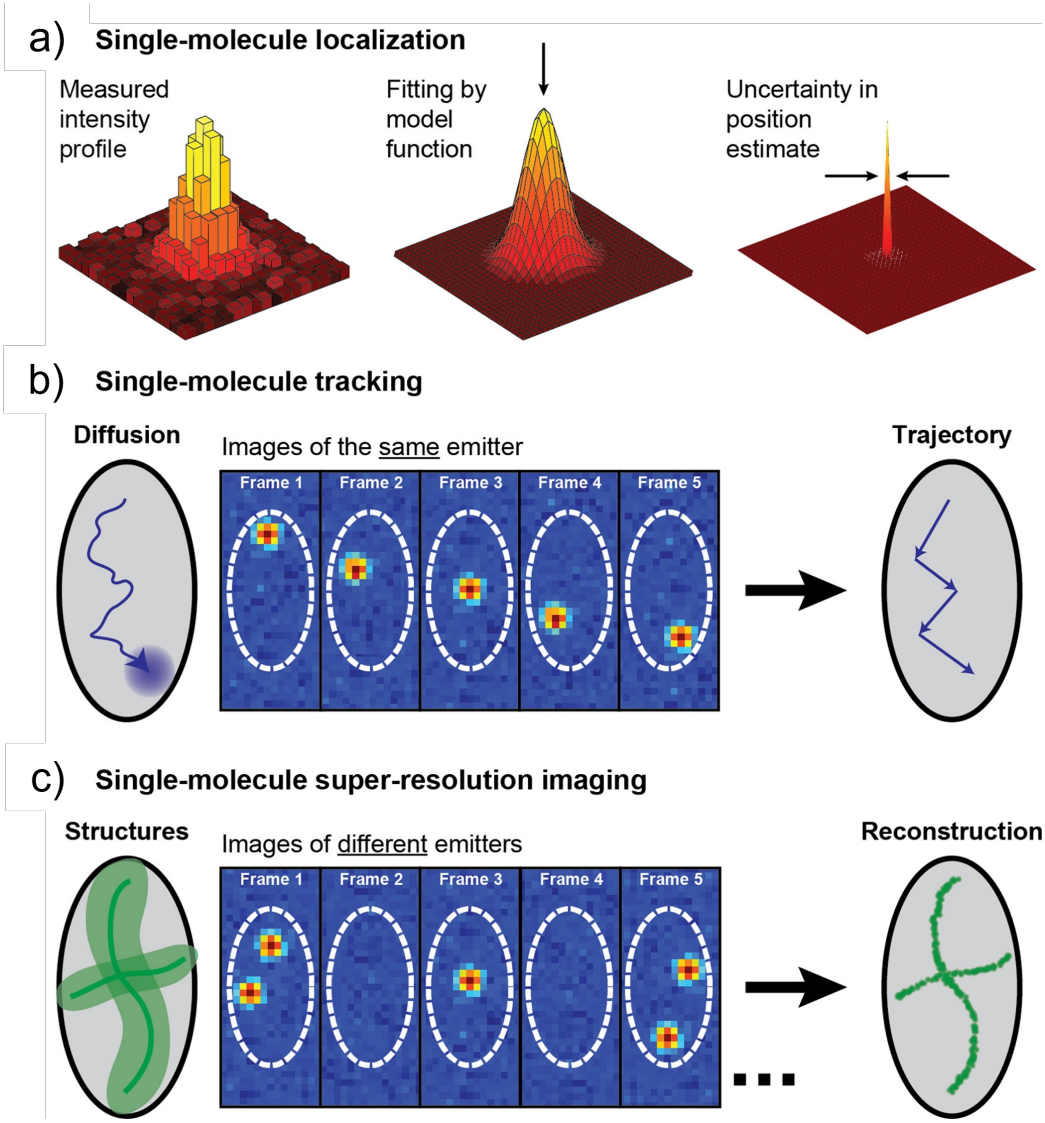

Figure 1.8: a) Working principle of single-molecule localization microscopy, b) single-particle tracking, and c) super-resolution microscopy (figure extracted from Nature Nanotechnology, 2017 [37]).

An essential topic we will discuss in the following lines is how to appropriately sample the PSF in the camera pixels to optimize the resolution of the optical setup. Photon budget from fluorescent nanoparticles emission is low, however, a good sampling of the signal in the detector's pixels is necessary to attain super-localization. This concept can be understood in a very simple way: suppose the self-interfered PSF formed in the camera is contained in one pixel, in this case, we would not be able to localize the point-like emitter beyond the pixel size. On the other hand, if the PSF occupies at least two pixels (most preferably three pixels) of the camera, we would be able to fit the intensity profile to a Gaussian and apply 2D super-localization, Fig.1.9. This reasoning is supported by the Nyquist-Shannon theorem, which states that the sampling rate should be higher than double the maximum frequency present in the

spectrum of the signal to have good signal sampling and avoid information loss [64]. The Nyquist-Shannon theorem is expressed through a simple expression,

$$\nu > 2\nu_N,$$

where ν is known as the Nyquist rate (sampling rate required for a frequency not to alias), and ν_N is called Nyquist frequency (maximum frequency that will not alias given ν). Given that DL, given by Eq.1.1, is the maximum frequency we want to sample, then $\nu_N = 1/DL$, and ν must be equal to N pixels per DL, i.e. $\nu = N/DL$. Thus, following the Nyquist-Shannon theorem:

$$\frac{N}{DL} > \frac{2}{DL} \quad \Longrightarrow \quad N \geq 3.$$

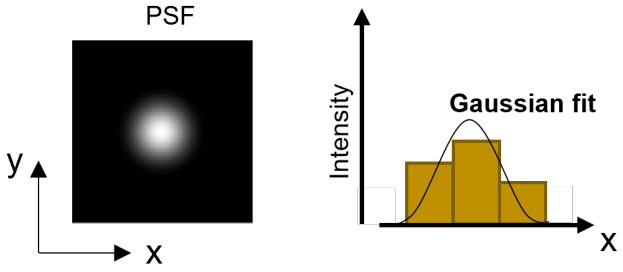

Figure 1.9: Sampling of the PSF (simulation) among the pixels in the camera.

We now explore how noise influences resolution when using SMLM. Shot noise affects the localization precision by scaling it as $N_{ph}^{-1/2}$, where N_{ph} is the number of photons in the signal, while the background noise scales the precision as N_{ph}^{-1} [65]. An additional source of noise can be considered for a finer description of the localization precision: pixelation noise, consisting on the increment of localization error due to the finite size of the pixels in the detector, and caused by the uncertainty about where within the pixel did the photon detected arrive [65]. Eq.1.2 gives a full representation of the localization error (Δx) in 2D considering shot noise, background noise, and pixelation,

$$\langle (\Delta x)^2 \rangle = \frac{s^2 + a^2/12}{N_{ph}} \left(\frac{16}{9} + \frac{8\pi s^2 b^2}{a^2 N_{ph}} \right), \tag{1.2}$$

where s is the standard deviation of the Gaussian fit, a is the pixel size, and b in the number of background noise photons [2]. Moreover, the 2D SMLM analysis method using least square Gaussian fits has been demonstrated to successfully agree with the predictions of Eq.1.2 for photon budget > 500 [65], proving that this localization method is robust and agrees with the predictions of theory when having different sources of noise while performing imaging experiments. This is the reason why we have chosen to use least square Gaussian fitting when applying SMLM in this thesis project, and a more detailed explanation of the analysis process is given in chapter 2.

Under the frame of this thesis, we will be focusing on the applications of SELFI on single-particle tracking in the near-infrared to reconstruct three dimensional trajectories. To assess the resolution attainable with SELFI, we calculate both the precision (standard deviation, SD) and accuracy (root mean square error, RMSE) of the localization. The SD gives us information regarding the reproducibility of the localization analysis process, whereas the RMSE tells us how close is the position determined with the localization code when compared to the real position. Also, sampling will be of high relevance in section 1.2 where we discuss how we experimentally designed our optical setup.

1.1.2 Concept of super-localization in three dimensions

As mentioned in the introduction chapter, there are different strategies to determine the axial position of a fluorescent emitter, such as the double-helix phase mask (DH), cylindrical lens (CL), and multiplane imaging (MP). However, these methods are not optimal for fluorescence microscopy since they exhibit some disadvantages: CL and DH broaden the PSF in a depth-dependent manner, while MP splits the photon budget of the emitter, which implies a depletion in the resolution. Moreover, none of these methods work well with aberrations and low photon budget, which is the case when imaging deep inside tissue. In contrast, our strategy is based on SELFI due to a few advantages, such as the fact that it does not broaden the PSF, is not aberration dependent, and is suitable for low signal, which allows us to use on applications of deep tissue biological imaging.

To understand the approach we use to retrieve the z-position of an emitter, let's consider what happens when the emitter is observed through the microscope. The PSF of the point source formed at the exit of the microscope can be approximated, as discussed above, to a Gaussian distribution, Fig.1.10. We will thus model the image formation of a point emitter by a Gaussian beam.

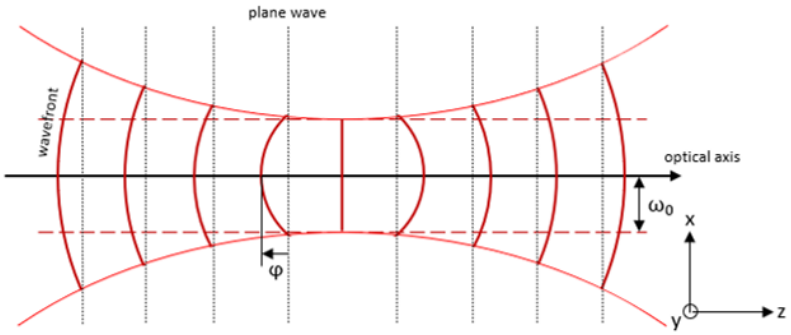

Figure 1.10: Gaussian beam approximation of the image a point source observed through a microscope.

The electromagnetic field of the image formed in a (x, y, z) point in space is written as $PSF(x, y, z) = |PSF|(x, y, z) \exp(-i\varphi(x, y, z))$, and the intensity is approximated to the following Gaussian function [66]:

$$|PSF|^2(r, z) \approx \frac{2P}{\pi\omega^2(z)} \exp\left(-\frac{2r^2}{\omega^2(z)}\right), \tag{1.3}$$

where

$$\omega(z) \approx \omega_0 \left[1 + \left(\frac{2z}{k\omega_0^2}\right)^2\right] \quad \text{and} \quad \omega_0 = \frac{DL}{\sqrt{2\ln 2}}, \tag{1.4}$$

$r^2 = x^2 + y^2$, P is the intensity power of the beam, $k = 2\pi/\lambda$ wave vector, and $DL = 1.22\lambda/2NA$. $\varphi(x, y, z)$ contains the information regarding the phase evolution along the optical axis of propagation and the wavefront curvature ($R(z)$) [66]:

$$\varphi(r, z) = kz - \arctan\frac{2z}{k\omega_0^2} + \frac{kr^2}{2R(z)}, \tag{1.5}$$

where

$$R(z) = z\left[1 + \left(\frac{k\omega_0^2}{2z}\right)^2\right]. \tag{1.6}$$

Fig.1.11 exhibits the intensity and phase dependency on the axial position (z) for an emission wavelength of 980 nm and $NA = 1.27$. For calculation simplicity, $r = 0$.

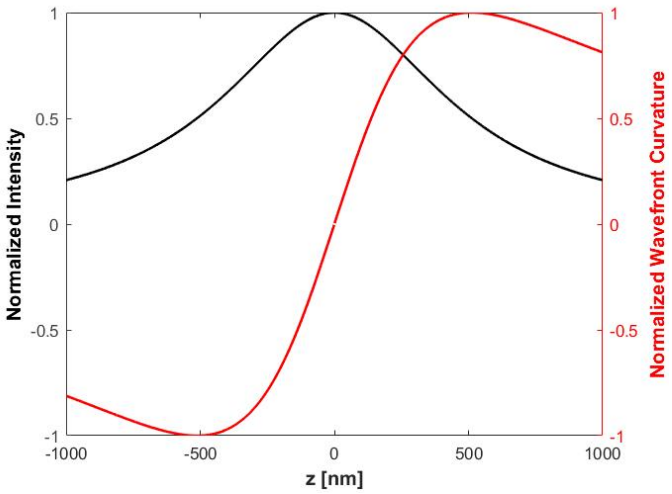

Figure 1.11: Gaussian beam intensity and phase propagation along z for $\lambda = 980$ nm and $NA = 1.27$.

As already mentioned, by calculating the centroid of the intensity distribution, we retrieve the lateral position of the point emitter with sub-diffraction precision, and this is referred as super-localization. Interestingly, Fig.1.11 shows that the phase is an

odd function within a region around $z = 0$, meaning that for each z-position, the phase has a unique value. Thus, by accessing the phase, we should be able to determine the axial position of the fluorescent emitter. However, a conventional PSF, which is an intensity distribution, does not give any information about the phase. Therefore, to retrieve the phase, one strategy is to generate interference, which encodes the phase information in it. In this case, we generate a self-interference of the field producing the PSF. The relationship between phase and self-interference is described in section 1.1.3, while how to retrieve the axial localization from the images obtained with SELFI is explained in section 1.1.4. To conclude, SELFI uses both, intensity and phase, to give complete 3D localization of the point source imaged.

1.1.3 Self-interference generation in single-molecule fluorescence microscopy

The concept of SELFI relies on the availability to measure the phase to retrieve the localization of the emitter along the z-axis. As we will discuss in the next paragraph, fluorescence is an incoherent process and conventional approaches for phase measurements based on external references cannot be used. We have thus proposed to make the emitter's signal interfere with itself. How to generate self-interference and its correlation with phase will be explained in the following pages. But first, let's recall that the work presented in this thesis will be based on the fluorescence of single molecules. Therefore, it is important to review the concept of fluorescence.

Fluorescence is an incoherent process that defines the photon emission that takes place as a consequence of the energy decay from an excited state to the ground state in the energy landscape of the molecule, as portrayed in the Jablonski diagram shown in Fig.1.12 [67]. Since there are multiple vibrational levels, vibrational relaxations take place, leading to a shift in the emission wavelength in regards to the absorption. In fact, one of the reasons for the fluorescence to be temporally incoherent is vibrational relaxations, and as a consequence this can be seen in the emission spectra which are large. Due to the comparatively low time delay between photon absorption and emission, which is typically less than a microsecond in length, the emission of light through the fluorescence process occurs almost simultaneously with the absorption of the excitation light [67].

The concept of coherence is fundamental in optics, and is closely tied to the ability of light to interfere. Two electromagnetic fields are said to be coherent when they present same frequency and zero or constant phase difference whether in time or space. As mentioned above, fluorescence is typically incoherent, but since we are under the frame of single-molecule, the fluorescence of single emitters is spatially coherent because it comes from the same source. Therefore, the emission from a

point emitter can interfere with itself because of spatial coherence.

Let's recall the concept of interference too. This phenomenon takes place when two or more coherent electromagnetic waves coincide on a given point in space, and their electromagnetic fields add up [68]. When the crests of the waves coincide, the field amplitude experienced by the point in space is equal to the sum of the individual amplitudes of each wave, this is called constructive interference. On the contrary, when the crest of one wave coincides with the trough of another, leading to a null field amplitude, is called destructive interference. However, when incoherent waves superpose, the relative instantaneous phase between each wave is not maintain through time. It means that on the time scale of observation (typically μs to s) there will be no stable interference pattern between the waves. Thus, we consider that we sum the intensity of each beam and not the amplitude.

SELFI was initially developed for visible fluorophores, where the Jablonski diagram applies. Although the present work is mainly based on semiconducting nanoparticles, the concepts previously discussed for single fluorescent molecules is still rightful.

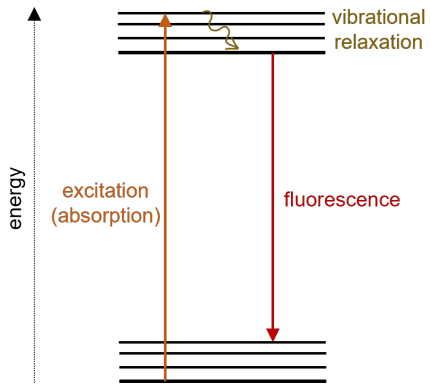

Figure 1.12: Jablonski diagram of energy for fluorescence.

SELFI is based on the generation of an interferogram by placing a diffraction grating in the path of the light emitted so that it can interfere with itself before reaching the camera, Fig.1.13. More precisely, the diffraction grating must be positioned right before the exit imaging plane of the microscope. Considering the usual dim signal that comes from fluorescent emitters, we use a 2D phase-only diffraction grating, meaning that it does not modify the amplitude of the signal, assuring the transmission of as much photons as possible to the detector [9]. On the other hand, due to the the large emission spectrum of fluorescence, we have used a grating that does not transmit the 0-order of diffraction to have an achromatic interference signal through an spectral range consistent with the emission spectrum of the fluorophore. Therefore, we have customized a 2D diffraction grating checkerboard-like that introduces a dephasing of π every other half period ($p/2$), Fig.1.14.

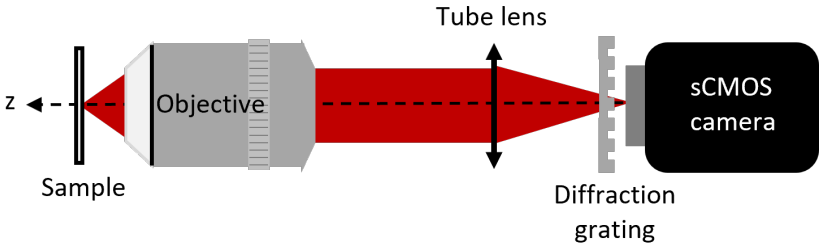

Figure 1.13: Microscopic system with a diffraction grating placed in the path traversed by the light.

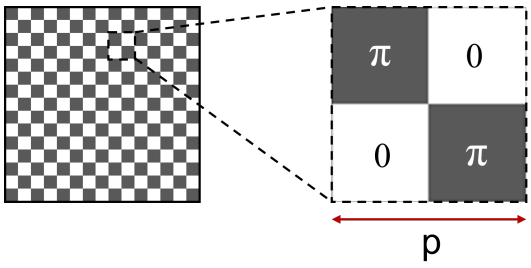

Figure 1.14: 2D phase-only diffraction grating with periodicity $p = 20$ μm.

The transmittance function of such grating, with period p, is given by Eq.1.7.

$$T(x,y) = \exp\left[i\pi \,\mathrm{rect}\left(\frac{x}{p}\right)\mathrm{rect}\left(\frac{y}{p}\right)\right]$$
$$\text{where} \quad \mathrm{rect}(\alpha) = \begin{cases} 1, & |\alpha| < \frac{1}{2} \bmod [1] \\ 0, & \text{else} \end{cases} \tag{1.7}$$

When writing the transmittance in Fourier series, Eq.1.8, we observe that the π-dephasing cancels out all the even orders of diffraction, including the 0-order, which corresponds to the non diffracted field. These calculations are explained in detail in the thesis of Jeanne Linarès-Loyez. It was also demonstrated that there is a decay of the Fourier amplitudes in $1/n$, where n is each of the diffraction orders allowed. Moreover, 66% of the energy transmitted by the grating is found in the first four orders of diffraction corresponding to ± 1 in both x and y directions. This is the reason for us to consider that four replicas are the main ones superposing and creating the interference pattern, Fig.1.15, without spreading the point spread function of the observed point emitters.

$$T(x,y) = -\frac{4}{\pi^2}\sum_{n=-\infty}^{+\infty}\sum_{m=-\infty}^{+\infty}\frac{\exp^{\frac{2i\pi}{p}[(2n+1)x+(2m+1)y]}}{(2n+1)(2m+1)} \tag{1.8}$$

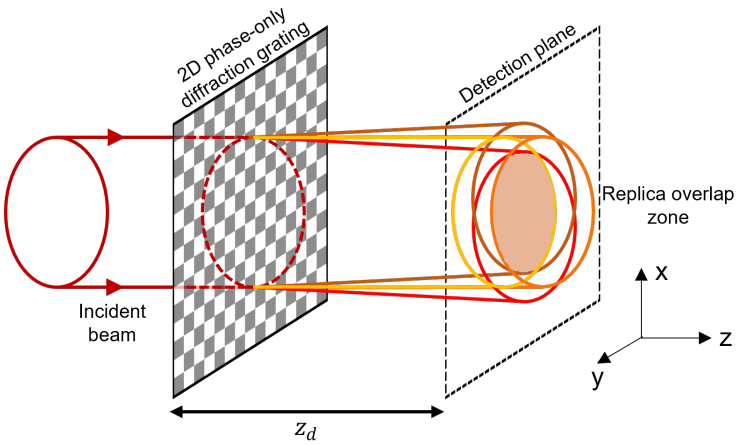

Figure 1.15: Principle diagram of the SELFI technique: formation of replicas that interfere in the detector plane.

In order to give a theoretical description of the interferogram, let's consider now an incident electromagnetic wave $E(x, y, z) = a(x, y, z) \exp^{ik_0\varphi(x,y,z)}$, where $a(x, y, z)$ is the wave's amplitude, $k_0 = 2\pi/\lambda_0$ its wavevector, λ_0 its emission wavelength, and $\varphi(x, y, z)$ the wavefront curvature. This expression of the electromagnetic field is obtained with the assumption of the slowly varying envelope, i.e. that the dimensions characteristic of the spatial variation of the phase are small compared to the wavelength. Even though all orders diffracted by the network contribute to create the interferogram on the camera, we only keep the first 4 orders to simplify things and explain how the interferogram was calculated. This decision is acceptable because, although we have shown that the higher orders are also gathered, 66% of the energy is contained in the +1 and -1 orders in both x and y directions. According to the notations detailed on the diagram of Fig.1.16, the field at the (x, y) point can be seen as the sum of four fields:

- Order -1 of the field in both x and y axes at $(x+s/2, y+s/2)$: $E(x+s/2, y+s/2)$
- Order -1 of the field in x and +1 in y at $(x - s/2, y + s/2)$: $E(x - s/2, y + s/2)$
- Order +1 of the field in x and -1 in y at $(x + s/2, y - s/2)$: $E(x + s/2, y - s/2)$
- Order +1 of the field in both x and y axes at $(x-s/2, y-s/2)$: $E(x-s/2, y-s/2)$.

The field intensity is then expressed as:

$$
\begin{aligned}
I(x,y) = & \left| \frac{E(x+s/2, y+s/2)}{2} + \frac{E(x-s/2, y+s/2)}{2} + \frac{E(x+s/2, y-s/2)}{2} \right. \\
& \left. + \frac{E(x-s/2, y-s/2)}{2} \right|^2 \\
= & \left| \frac{a(x+s/2, y+s/2)}{2} \exp^{ik_0\varphi(x+s/2, y+s/2)+i\vec{k}_{--}\cdot\vec{r}} \right. \\
& + \frac{a(x-s/2, y+s/2)}{2} \exp^{ik_0\varphi(x-s/2, y+s/2)+i\vec{k}_{+-}\cdot\vec{r}} \\
& + \frac{a(x+s/2, y-s/2)}{2} \exp^{ik_0\varphi(x+s/2, y-s/2)+i\vec{k}_{-+}\cdot\vec{r}} \\
& \left. + \frac{a(x-s/2, y-s/2)}{2} \exp^{ik_0\varphi(x-s/2, y-s/2)+i\vec{k}_{++}\cdot\vec{r}} \right|^2,
\end{aligned}
\tag{1.9}
$$

where

$$
\vec{k}_{++} = k_0 \begin{pmatrix} \sin\xi \\ \sin\xi \\ \cos\xi \end{pmatrix}, \quad \vec{k}_{+-} = k_0 \begin{pmatrix} \sin\xi \\ -\sin\xi \\ \cos\xi \end{pmatrix},
$$

$$
\vec{k}_{-+} = k_0 \begin{pmatrix} -\sin\xi \\ \sin\xi \\ \cos\xi \end{pmatrix}, \quad \vec{k}_{--} = k_0 \begin{pmatrix} -\sin\xi \\ -\sin\xi \\ \cos\xi \end{pmatrix}.
$$

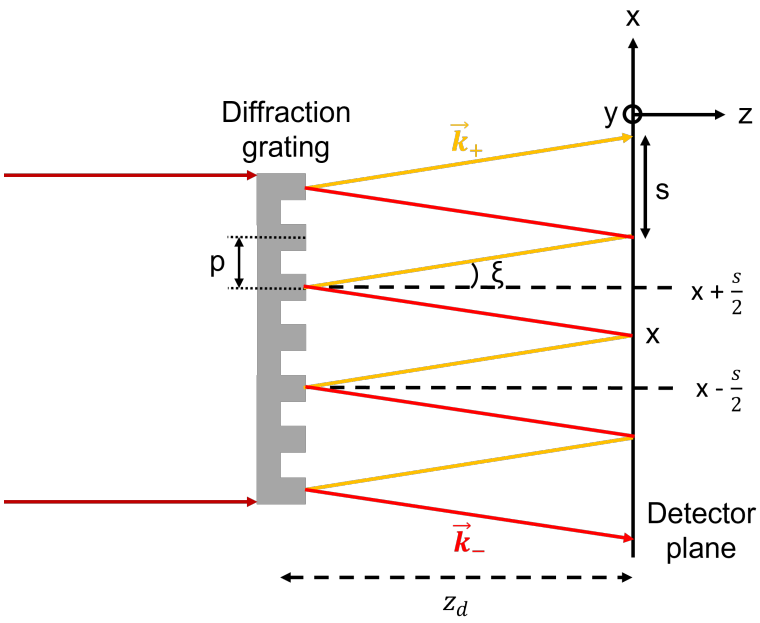

Figure 1.16: Visualization of the diffraction produced by a one-dimensional grating, details of the notations used for the calculations. This idea can be generalized to the case of 2D diffraction grating. Recall $p = 20$ μm is the periodicity of the diffraction grating.

By simplifying Eq.1.9, we obtain Eq.1.10, which describes the intensity of an interferogram produced after the light passes through a 2D diffraction grating. A detailed calculation of how to go from Eq.1.9 to Eq.1.10 can be found in the thesis of Jeanne Linarès-Loyez.

$$\begin{aligned} I(x,y) = I_0 &+ I_x \cos\left[\frac{4\pi}{p}\left(x - z_d\frac{\delta\varphi}{\delta x}\right)\right] \\ &+ I_y \cos\left[\frac{4\pi}{p}\left(y - z_d\frac{\delta\varphi}{\delta y}\right)\right] \\ &+ I_{x+y} \cos\left[\frac{4\pi}{p}\left((x+y) - z_d\frac{\delta\varphi}{\delta(x+y)}\right)\right] \\ &+ I_{x-y} \cos\left[\frac{4\pi}{p}\left((x-y) - z_d\frac{\delta\varphi}{\delta(x-y)}\right)\right], \end{aligned} \tag{1.10}$$

where

$$\begin{cases} I_0 = \frac{a^2(x+s/2,y+s/2)+a^2(x-s/2,y+s/2)+a^2(x+s/2,y-s/2)+a^2(x-s/2,y-s/2)}{4} \\ I_x = \frac{a(x+s/2,y+s/2)a(x-s/2,y+s/2)+a(x+s/2,y-s/2)a(x-s/2,y-s/2)}{2} \\ I_y = \frac{a(x+s/2,y+s/2)a(x+s/2,y-s/2)+a(x-s/2,y+s/2)a(x-s/2,y-s/2)}{2} \\ I_{x+y} = \frac{a(x+s/2,y+s/2)a(x-s/2,y-s/2)}{2} \\ I_{x-y} = \frac{a(x+s/2,y-s/2)a(x-s/2,y+s/2)}{2} \end{cases} .$$

The resulting interferogram equation, 1.10, has a sinusoidal period of p/2 and is a function of (x, y). It is essential to remember that, at the first order in limited development, no term in this equation depends on the wavelength λ_0. This illustrates the achromatic nature of the SELFI method. Thus, we acquire interferences from a spectrally extended source, such as a fluorescent emitter, as intended. This is only accurate, though, if we approximate that the interferogram is formed by only the +1 and -1 orders of each direction. The remaining orders increase the interferogram interrange's mild wavelength dependency. Although we haven't considered this weak dependence in our study, it could be interesting to find a mechanism to distinguish between emitters with various wavelengths. The distance z_d between the diffraction grating and the detector, which appears before the gradients $\delta\varphi/\delta x$, $\delta\varphi/\delta y$, and $\delta\varphi/\delta(x \pm y)$, is another significant element in Eq.1.10. It implies that the sensitivity for detecting the wavefront gradients improves with increasing distance z_d. In other words, this term on Eq.1.10 portrays that where to place the diffraction grating affects the axial resolution, and it is something to consider and explore experimentally, as we will discuss in section 1.2.4. Therefore, shift interferometry is a method with continuously varying sensitivity.

The fringes of the interferogram will deform in response to a frequency modulation centered on the frequency $2/p$ in the event of a non-planar wave, i.e. where

$\delta\varphi/\delta[x, y, (x \pm y)] \neq$ constant. In order to analyze the interferogram, a demodulation in Fourier space centered on this frequency will be used since the Fourier space carries the information regarding spatial frequencies. This will make it possible to measure the wavefront gradient. Ergo, thanks to the interferogram generated from self-interference, we are able to have access to the variation of the wavefront curvature or phase, leading us to correlate this information with a unique position in the z-axis of the emitter, as we can recall from Fig.1.11.

1.1.4 Localization retrieval from self-interfered signals

In the present section, we explain how to retrieve the z-localization from an image experimentally produced by SELFI. But first, we start by introducing how a self-referenced PSF image looks like: Fig.1.17 was experimentally obtained by imaging a PbS/CdS QD observed through the SELFI setup (see section 1.2.5 for details about the optical setup). The 2D phase-only diffraction grating creates replicas of the emission signal PSF, creating an auto-referenced interference pattern. After, the signal is collected by the detector.

We will use the Fourier transform (FT) of a SELFI image to retrieve, in a handy manner, the phase information from where we can determine the z-axis position as it will be demonstrated in the following pages. What is more, from the interferogram FT we will also obtain information about intensity. Therefore, the FT contains both intensity and phase data.

To extract the intensity profile from the FT, we apply a low pass filter, Fig.1.18. After, to retrieve the (x, y) position, we apply super-localization, as explained in section 1.1.2. Let's recall that it consists in fitting the intensity profile to a Gaussian, and by calculating its centroid we determine the lateral position of the emitter.

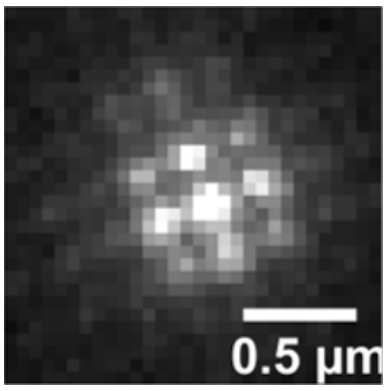

Figure 1.17: Self-interfered PSF image of a PbS/CdS QD produced experimentally.

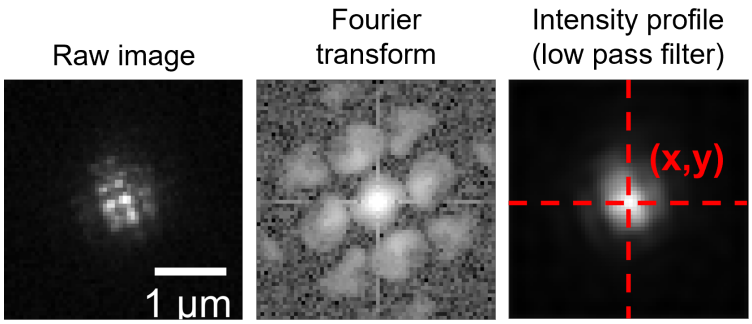

Figure 1.18: Image experimentally obtained when observing a PbS/CdS QD with SELFI. Image on the left is a SELFI PSF. On the center, its FT is shown. On the left, the intensity profile of the emitter is produced after applying a low pass filter in the FT. Then, (x, y) position is determined by fitting the intensity distribution to a Gaussian, and calculating its centroid.

In section 1.1.3, it was explained that the interference pattern produced with SELFI is correlated to the gradient of the phase, which varies depending on the z position of the emitter. Therefore, since the FT carries information of the phase, and it changes with each z position, then every FT is different for each position in z.

By taking images of a point emitter, such as PbS/CdS QDs, for different positions in z, we can produce a look-up table of FTs for different z values (z-stack), Fig.1.19. The z-stack can be generated thanks to the motorization of the microscope which enables us to shift the objective position in steps along the z-axis, therefore acquiring the interferogram of the nanoparticle in each of the depth of field planes. The minimum z-step the objective is able to make is 25 nm and there are some fluctuations of the same order, which leads to inaccuracy, reason why we have decided to use steps of 50 nm when performing the z-stacks. Once the acquisition is obtained, the Fourier transform for each z-position is obtained, and is different from one another, encoding the axial localization. After, this look-up table of FTs can be used to determine the z-position of other emitters by comparing their FTs with the ones given in the look-up table, now called calibration table. The comparison between the FTs is performed through Pearson coefficients, and the full analysis method behind the localization algorithm is described in chapter 2 of this thesis. The look-up-tables used for calibration are generated by using images experimentally obtained because real data gives us information on how the system actually behaves, which would not be the case if we would use simulated images for calibration instead.

In summary, the full routine for three-dimensional localization is shown in Fig.1.20: fluorescent emitters are imaged with SELFI, each of them is analyzed separately. For a single image of a fluorophore, its FT is calculated. To determine the lateral position, we apply a low pass filter to the interferogram to retrieve the intensity distribution, and we use super-localization. To determine the emitter axial position, we compare

its FT to the calibration table of FTs obtained by making a z-stack of images of another fluorophore.

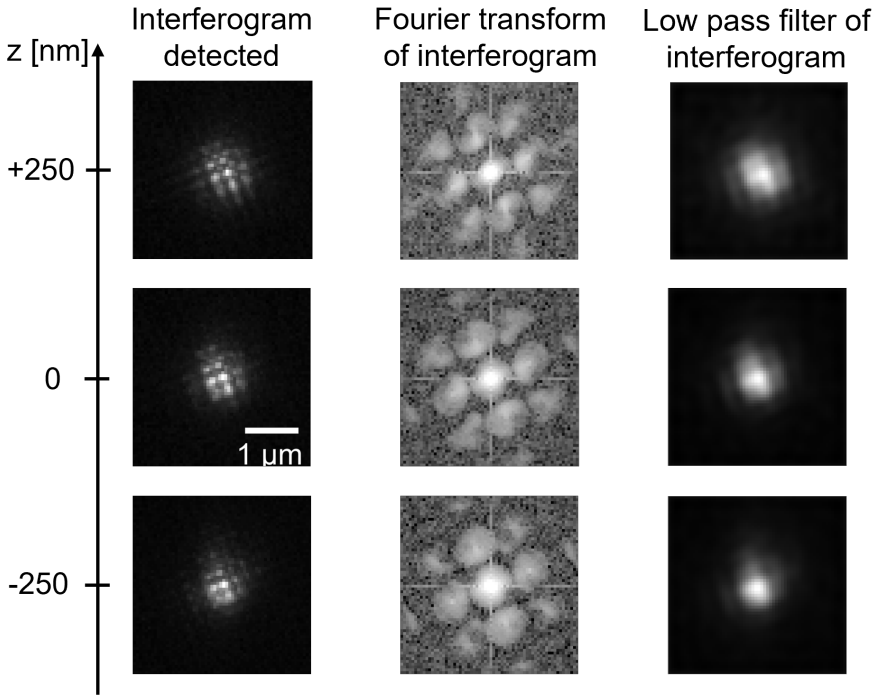

Figure 1.19: Look-up table of experimentally obtained SELFI PSFs at focus and ±250 nm of a PbS/CdS QD. Their Fourier transforms are also shown, as well as their intensity profile.

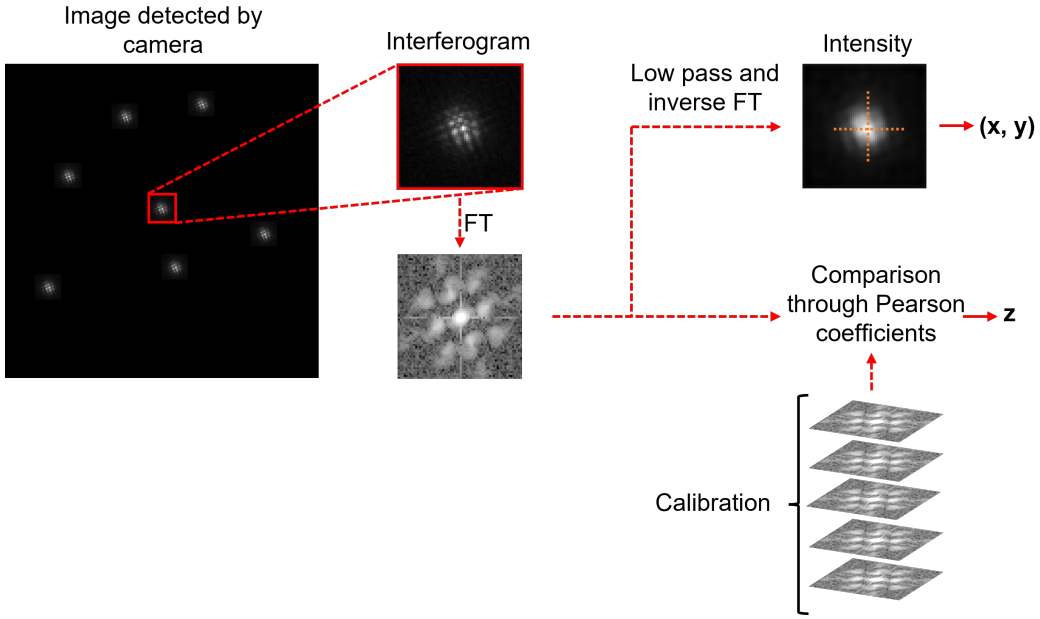

Figure 1.20: Routine for three-dimensional localization with SELFI.

It is worth mentioning that we use the Fourier transforms to make the calibration

table for comparison to localize other emitters, and that we do not use the interferograms so that the localization performance does not to depend on the relative positioning of the bright and dark fringes from one molecule to the other.

1.2 Experimental design and setup of the near-infrared SELFI optical system

In the present section, we present the design of SELFI for the near-infrared regime of wavelengths that can be applied to PbS/CdS QDs, SWCNTs, and any other flurophore emitting in the NIR. Specifically, during the design process, we consider multiple technical constrains including which camera to use, the type of emitters and its emission wavelength, the magnification required to attain super-localization, etc.

Prior to the design, let's discuss how we used the Nyquist-Shannon theorem to build the setup and optimizing its performance. In section 1.1.1, we demonstrated that at least two pixels are necessary to sample a PSF in the detector. However, two pixels are not enough when having an interferogram within the PSF given that they would not be distinguishable from one another, resulting in aliasing. Therefore, the PSF must be spread among more pixels, enough to have a good sampling but not too much to spread the dim fluorescent signal. By looking at Fig.1.21, we can determine that $\nu_N = 1/p$, and $\nu = 2N/p$, where N is the number of pixels to sample the half periodicity of the diffraction grating (p/2). Therefore, by applying the Nyquist-Shannon theorem, we obtain

$$\frac{2N}{p} > \frac{2}{p} \quad \Longrightarrow \quad N \geq 2.$$

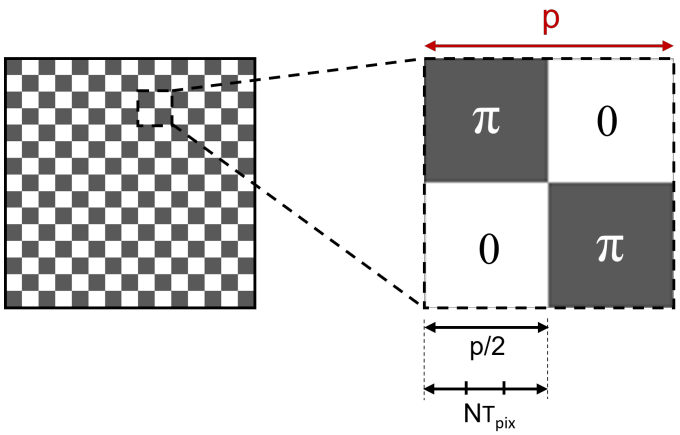

Figure 1.21: Interferogram sampling in the detector. p is the period of the diffraction grating, and $p/2$ should be sampled among N camera pixels of size T_{pix}.

In our case, we have decided to work with $N = 3$, meaning that one fringe will occupy three pixels in the camera. Three pixels per fringe is an adequate balance between signal-to-noise ratio and localization precision, leading to well sampled PSFs in the camera. Note that the number of pixels per PSF will be higher than 3 since a single PSF contains more than one fringe so that we can extract information from the interferogram.

1.2.1 Design of near-infrared SELFI system

The optimal sampling calculated through the Nyquist-Shannon theorem is 3 pixels either per PSF (for conventional 2D SMLM) or per fringe (for SELFI 3D super-resolution). However, in order to attain this proportion, a magnification relay may be needed between the microscope and the camera. This discussion is followed in the pages to come.

Due to its high transmittance ($> 70\%$) in the NIR, and high numerical aperture (NA), the objective used is the Nikon Plan Apochromat, 60×, $NA = 1.27$, water immersion, IR. Therefore, the following calculations will be done by considering this objective.

1.2.1.1 Signal sampling in detector for 2D SMLM

In the object plane (OP), the PSF size (DL) of a single emitter observed through a microscope is given by Eq.1.1 in section 1.1.2. In the image plane (IP), i.e. in the plane of the detector, the PSF size is equal to the PSF in the OS times the total magnification from the objective until the image reaches the camera (M), Eq.1.11.

$$DL^{OP} = \frac{1.22\lambda}{2NA}, \quad \text{and} \quad DL^{IP} = DL^{OP} \times M \tag{1.11}$$

For a conventional microscopic system, such as Fig.1.22, when $\lambda \sim 1000$ nm, and $NA = 1.27$, the PSF size in the OP is ~ 500 nm. This corresponds to a PSF size of ~ 30 μm in the IP. If the detector has a pixel size of 15 μm, common in cameras for visible wavelengths, the sampling would be $\#pix./PSF = 30\mu m/15\mu m = 2$.

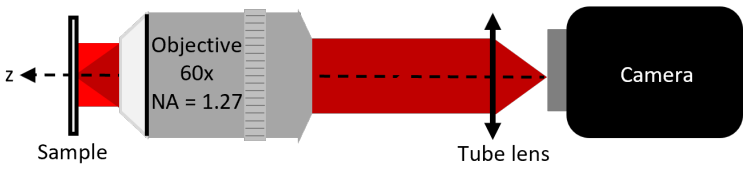

Figure 1.22: Microscope system.

To attain SMLM, we should introduce a relay with a magnification of 1.5 between the microscope and the detector to get 3 pixels per PSF, so that $DL^{IP} = 45\mu m$, and

$\#pix./PSF = 3$, Fig.1.23. Alternatively, this correction can also be performed by commercial microscopes which have a 1.5× extra magnification.

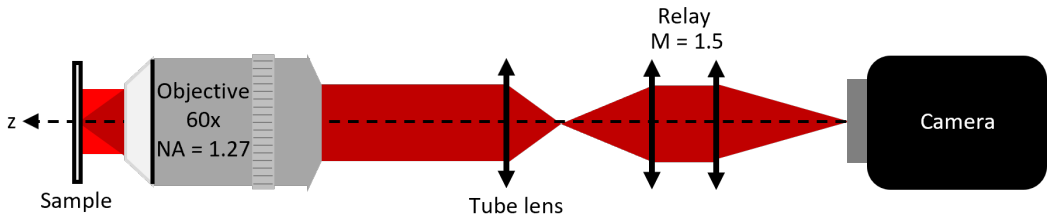

Figure 1.23: Microscope system corrected for SMLM.

1.2.1.2 Signal sampling in detector for self-interference super-resolution microscopy

Given that the optimal sampling is 3 pixels per fringe when the diffraction grating is placed, if the pixel size is 15 μm, then the relay must have a magnification of

$$\#pix./fringe = 3 \quad \Rightarrow \quad \frac{(10\,\mu\text{m}) \times (\text{relay magnification})}{15\,\mu\text{m}} = 3$$

$$\Rightarrow \quad \text{relay magnification} = 4.5.$$

As consequence, we should introduce a relay with magnification of 4.5 between the diffraction grating and the camera, Fig.1.24.

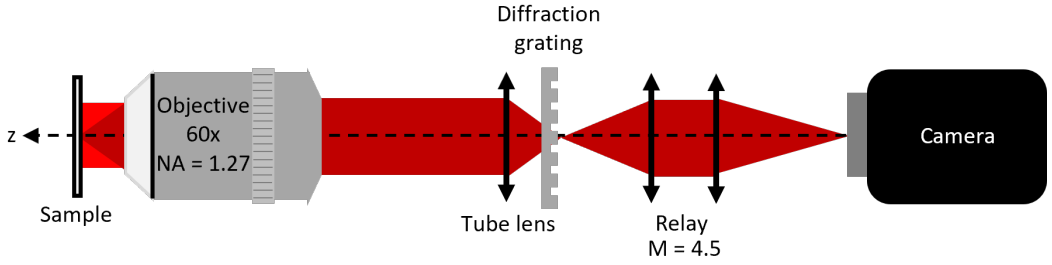

Figure 1.24: Self-interference setup corrected for super-resolution.

1.2.2 Instrumental considerations, field of view and optical aberrations

Once the parameters needed in the setup design are addressed, we choose the appropriate components to build the system. Before discussing all the elements chosen, it is important to mention that the diffraction grating here used is the same phase-only DG utilized to build the first SELFI setup. This DG has a period of $p = 20$ μm, and was optimized for visible wavelengths of emission. More precisely, it is a rectangular

DG, as portrayed in Fig.1.25, whose phase shift ($\Delta\varphi$) depends on the wavelength (λ) as [69]

$$\Delta\varphi = \frac{2\pi}{\lambda} h\,(n_2 - 1)\,, \tag{1.12}$$

where h represents the engraving depth in the rectangular structure, n_1 is the refractive index of air, and $n_2 = 1.4623$ is the refractive index of silica [70], which is the material of which the DG is made of. Recall from section 1.1.3 that the DG has a phase shift of π for visible wavelengths ($\sim$ 500 nm), therefore, according to Eq.1.12, h must be $\sim$ 500 nm as well, and this was the reasoning followed for customization. However, in the NIR, $\Delta\varphi \sim \pi/2$, leading to a dimmer contrast in the interferogram, but still effective for applications on 3D super-resolution localization in this wavelength range.

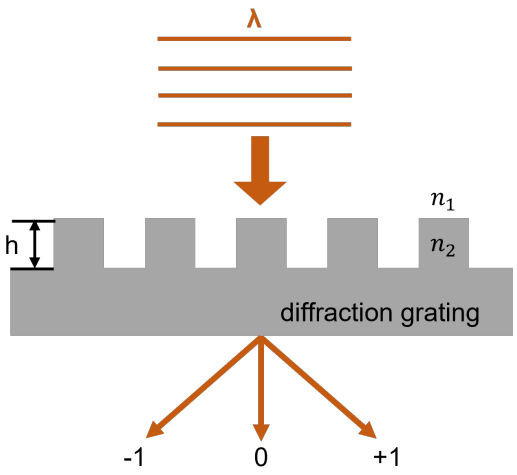

Figure 1.25: Schematic representation of light diffraction when passing through a phase grating with rectangular profile.

The first camera option, InGaAs C-RED 2 from First Light, is ideal for NIR and IR emission (quantum efficiency of $> 80\%$ for a wavelength range of around 950 - 1600 nm, as shown in Fig.1.26), and has a pixel size of 15 μm. To achieve super-resolution with SELFI, two relays, NIR Achromatic Pair Lens from Edmund Optics, were used with appropriate magnification (4.5×). This results in a field of view of 35×28 μm in the object plane. However, these relays presented high distortion among the filed of view. Let's recall that distortion is an optical aberration characterized by curvature of the field of view, as displayed in Fig.1.27. The disparity between a lens's transverse magnification and the off-axis image distance is the cause of geometrical distortion. Distortion can occur when this distance differs from what is expected by paraxial theory for constant transverse magnification because of variations in focal lengths and magnifications through different regions of the lens. Fig.1.28 displays an image of carbon nanotubes (emission at 985 nm) obtained by using the C-RED 2 camera

and both relays from Edumund Optics, it can be see that distortion is more evident as we move further from the center of the field of view. The high optical aberration present in the two-relays system led us to opt for another detector with smaller pixel size, and therefore smaller magnification correction.

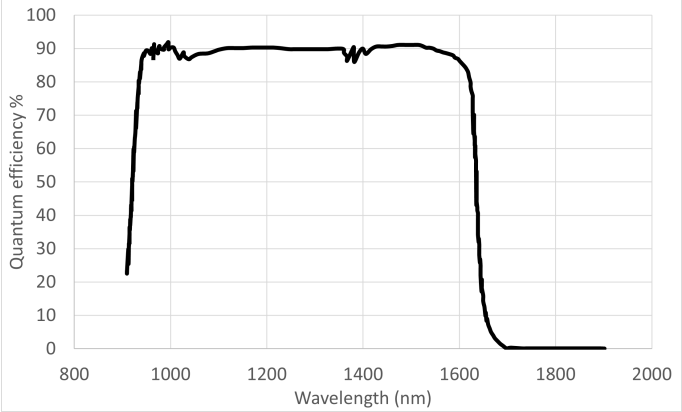

Figure 1.26: Quantum efficiency of InGaAs C-RED 2 camera from First Light.

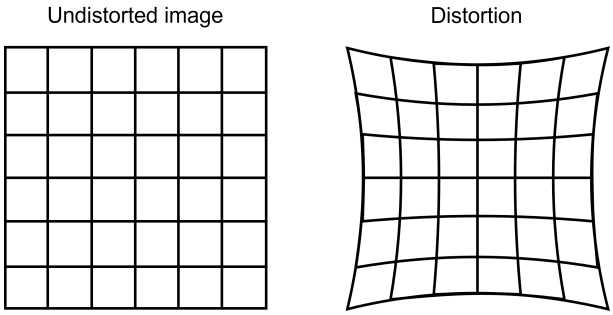

Figure 1.27: Effect of distortion aberration on the field of view.

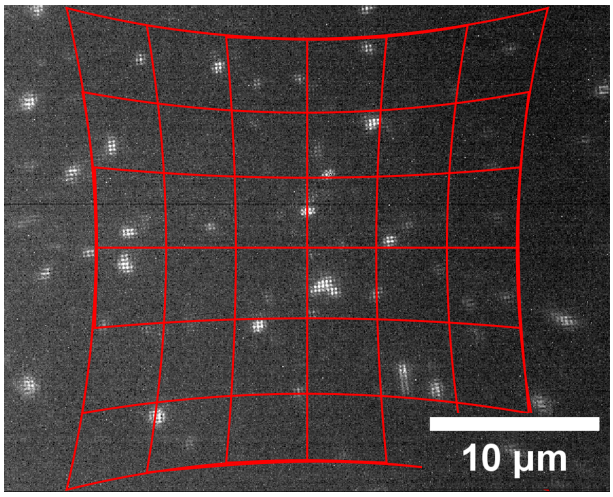

Figure 1.28: Effect of distortion aberration on an image of carbon nanotubes obtained with the setup composed by the InGaAs C-RED 2 and the two NIR Achromatic relays.

Due to the limited field of view on the camera and the distortion introduced by the relay, we have decided to acquire another camera, an sCMOS Kuro from Teledyne Princeton Instruments with a pixel size of 11 μm. This camera has the advantage to have an improved sensitivity in the NIR for a silicon based sensor (quantum efficiency of $> 10\%$ for a range of 800 - 1000 nm, as shown in Fig.1.29), smaller pixel size, and low noise. An additional advantage of this camera is that, being sensitive also to visible wavelengths, it will enable us to compare the performance of our system from the far-red to the NIR.

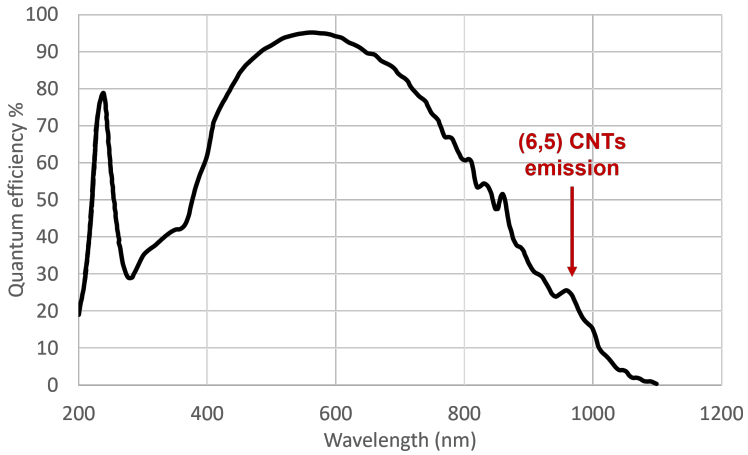

Figure 1.29: Quantum efficiency of sCMOS Kuro camera from Teledyne Princeton Instruments.

The appropriate magnification correction when Kuro is added to the setup is calculated as

$$\#pix./fringe = 3 \quad \Rightarrow \quad \frac{(10\,\mu\text{m}) \times (\text{relay magnification})}{11\,\mu\text{m}} = 3$$
$$\Rightarrow \quad \text{relay magnification} = 3.3.$$

Two achromatic lenses were used to achieve this magnification, Mounted Achromatic Doublets with coating range from 650 to 1050 nm from Thorlabs. This optical setup does not present distortion. Fig.1.30 is a comparison of two carbon nanotube (emission at 985 nm) images with both C-RED 2 and Kuro cameras. As portrayed, Kuro's field of view (66×66 μm) is twice larger than C-RED's field of view, beneficial when it comes to single-particle tracking experiments.

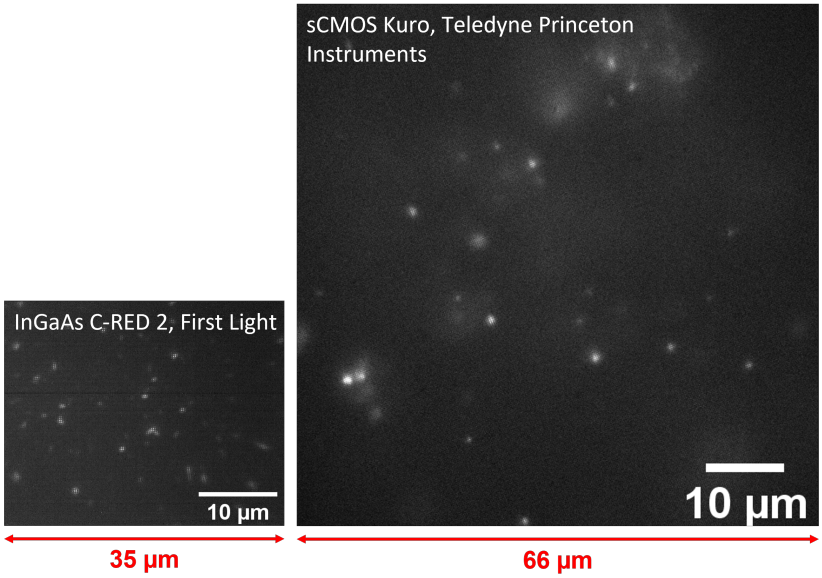

Figure 1.30: Carbon nanotubes observed through C-RED 2 and Kuro cameras. Fields of view have the same scale, C-RED 2 detector is almost half of the size of Kuro's detector.

1.2.3 Laser sources and fluorescent filters

To excite the different fluorophores, we used the following lasers, and excitation and emission filters:

- PbS/CdS QDs and SWCNTs: we first used the 3900S CW Tunable Ti Sapphire laser from Spectra-Physics, which is a solid state IR laser that we tuned at 845 nm. However, this laser stopped working by the end of the thesis. Therefore, during the last six months of experiments, we used the Laser Diode Controller (LDC210C) from Thorlabs. As filters, we have used a longpass 900 nm dichroic mirror (DMLP900R) from Thorlabs, and a longpass 900 nm emission filter (ET900LP) from Chroma for both lasers. For the diode laser, we additionally used an excitation filter, the bandpass 840/12 (FF01-840/12-25) from Semrock.

- TetraSpeck: we used the OBIS LX 660 nm 75 mW Laser System from Coherent. And the filters we employed are a bandpass 677/20 nm (FF01-677/20-25), and a bandpass 721/65 nm emission filter (FF01-721/65-25) from Semrock.

1.2.4 Diffraction grating positioning for resolution optimization

In the present section, we discuss an essential part of building the SELFI optical setup: where exactly to position the diffraction grating (DG). As mentioned above,

the DG must be placed at the exit imaging plane (IP) of the microscope such that the signal coming from the sample interferes with itself before reaching the detector, as observed in Fig.1.24. However, recall that the sensitivity and PSF spreading depend on the distance between the DG and the IP, z_d, as shown in Eq.1.10. Actually, there is an optimal position for the DG to reach the highest resolution possible. But before getting into where to position the DG, it is better to place it with a small tilt with respect to the pixels mesh in the camera to avoid aliasing.

Now, the first step to correctly place the DG is to identify the region around the IP, this gives us an idea of where the DG will be set. To do so, we use white light, we put the dichroic and emission filter used to image SWCNTs to pick wavelengths above 900 nm, and with the camera on, we can observe how the interference pattern appears when the DG is within this region. In fact, we notice how the replicas of the signal move as we displace the DG along the optical axis. If there is no interferogram observed in the camera, it is a clear indicator that the DG is too far from the IP. After, we set the DG where the IP is, i.e. where the replicas of the signal collide into one. To have micrometric precision, we guide ourselves by observing that the interferogram appears grey since there is not a significant contrast between the crests and the troughs, as displayed in Fig.1.31, meaning that the DG is truly in the IP. This narrow area is located between two clear zones (*Before IP* and *After IP*) where there is a considerable contrast, also shown in Fig.1.31. A comparison between both images before IP and after IP exhibits an inversion of black and white fringes (crests and troughs) in the interference pattern, signalling we are surrounding the IP, and making easier the task of targeting the IP. Fig.1.31 also shows a good contrast in the interferogram, even when the DG is not optimized for NIR. We may also introduce a definition that will be used for explanatory purposes later on: *interfringe*, which is defined as half fringe periodicity, as shown in Fig.1.32.

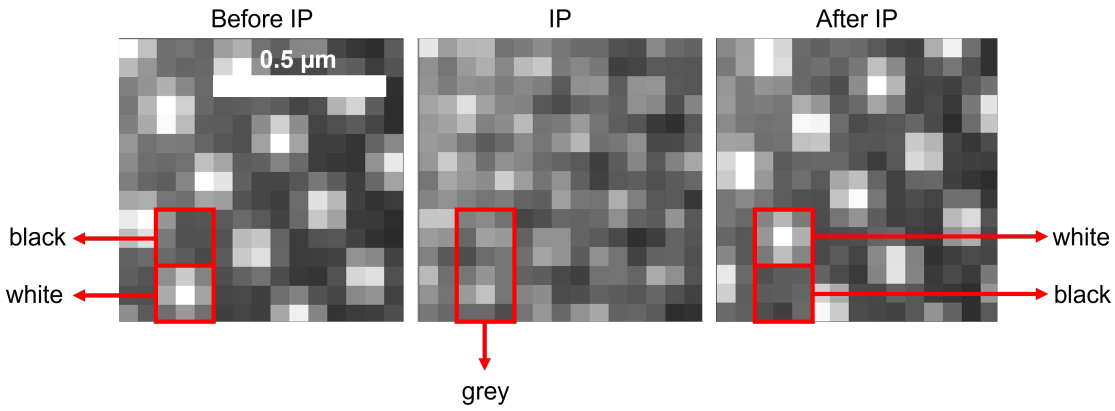

Figure 1.31: White light interferogram image obtained by placing the DG before, in, and after the IP. There is an inversion in the black and white fringes around the IP.

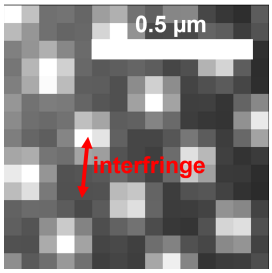

Figure 1.32: Interfringe distance in the interferogram.

Remember from Eq.1.10 that, the interferogram profile depends on the distance between the DG and the IP, z_d. Thus, the sensitivity of the interferogram to the different positions of the emitter along z is higher when z_d. However, there is a limit to how big z_d can be given that if the DG is too far away from the IP, the PSF replicas would not meet to create the interference pattern. This points out the necessity to refine the position of the DG by imaging QDs while trying different positions of the DG to optimize the resolution. Therefore, the following experiment has been performed: PbS/CdS QDs haven been fixed in a coverslip by spincoating them for 2 minutes. After, they have been excited with an 845 nm laser, and imaged through the SELFI setup. As mentioned before, its emission occurs at ∼1000 nm. For different positions of the DG along the optical axis, a z-stack has been made. 30 images were taken for each position in z of the fixed QDs. A more detailed explanation on how to prepare QDs samples as well as the imaging procedure can be found in section 1.3.1. After, images were analyzed by using a SELFI analysis script we have developed, and whose functioning will be explained in chapter 2.

Fig.1.33 exhibits how the interfringe (in x and y) within the SELFI PSF of a PbS/CdS QD varies in z as we set the DG in three different positions: a) at the IP, b) $z_d = 150$ μm, and c) $z_d = 175$ μm from the IP. In these plots, the focus (red vertical line) occurs at $\sim$ 1500 nm for a, at $\sim$ 600 nm for b, and at $\sim$ 800 nm for c. For each position in z, 30 images were taken (orange dots), and the average interfringe was calculated (blue dots). Observe that, as the DG is placed further from the IP, the interfringe in both x and y varies more.

Fig.1.34 shows the z-localization, accuracy, and precision of a fixed PbS/CdS QD when the DG is placed at the IP. These plots are produced by localizing the QD using itself as calibration probe. In the plots, *Nominal* z is the z-positions given by the microscope as we control it to move in steps of 50 nm. *Fitted* z is the z-localization resulted from the SELFI analysis code. A good localization performance would show a match between the Fitted z values and the Nominal z values for a range of ∼1 μm around the focus (red lines). The orange cloud in the z-localization plot represents the stardard deviation for the Fitted z values for each z position. As observed in Fig.1.34, the z accuracy, given by the root mean square error (RMSE), is ∼100 nm at

the focus. The z precision, understood as the standard deviation (SD), is also $\sim$ 100 nm at the focus. Actually, both RMSE and SD fluctuate from values between $\sim$70 - 110 nm for a region of 500 nm around the focus. Nevertheless, both axial accuracy and precision improve as the DG is placed further from the IP, as is shown in Fig.1.35 and Fig.1.36. The (x, y) precision is also exhibited in Fig.1.34, and is < 10 nm.

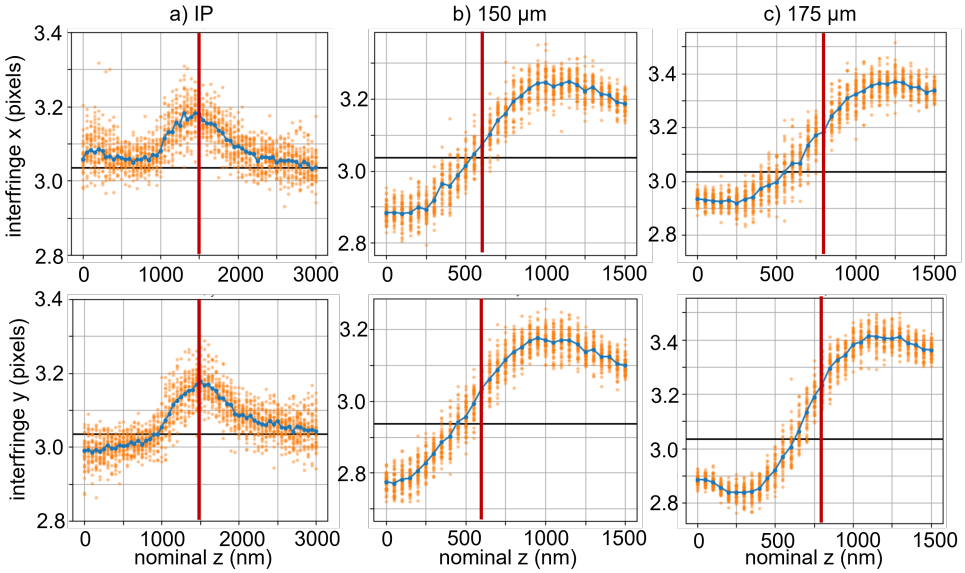

Figure 1.33: Interfringe in x and y as a function of z for different positions of the DG: a) at the IP, b) $z_d = 150$ μm, and c) $z_d = 175$ μm from the IP. The red lines indicate where the focus is.

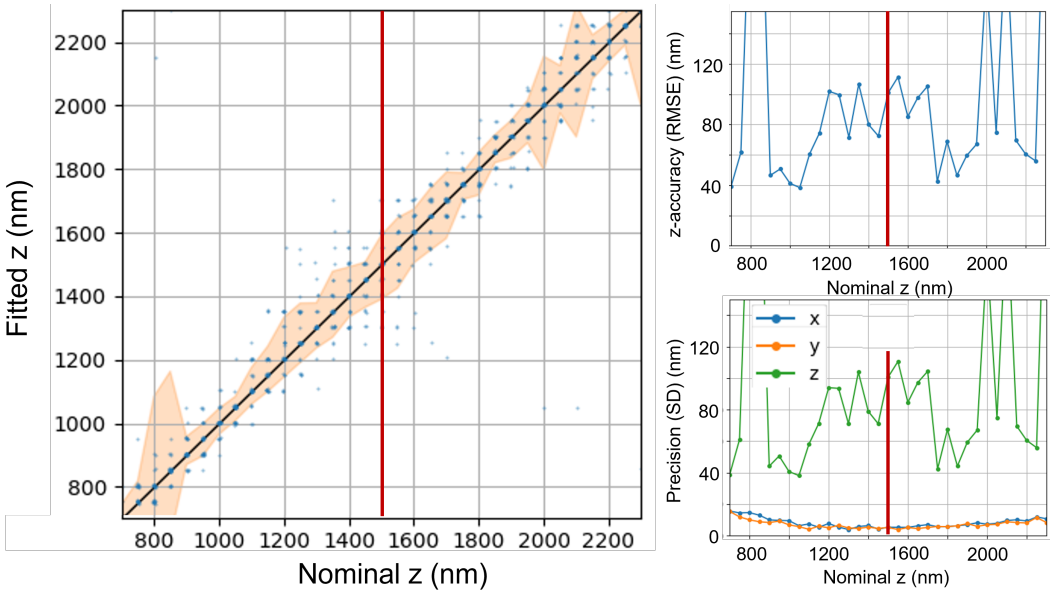

Figure 1.34: z-localization, accuracy, and precision of a fixed PbS/CdS QD when the DG is placed at the IP. Red line indicates where the focus occurs.

Fig.1.35 presents the z-localization, accuracy, and precision of a fixed PbS/CdS QD when the DG is placed 150 μm far from the IP. Both z accuracy and precision are $\sim$60 nm at the focus, and both fluctuate from $\sim$45 - 80 nm for an area $\sim$1 μm around the focus. Meaning there is an amelioration of the resolution as compared to the one obtained when the DG is placed at the IP, Fig.1.34.

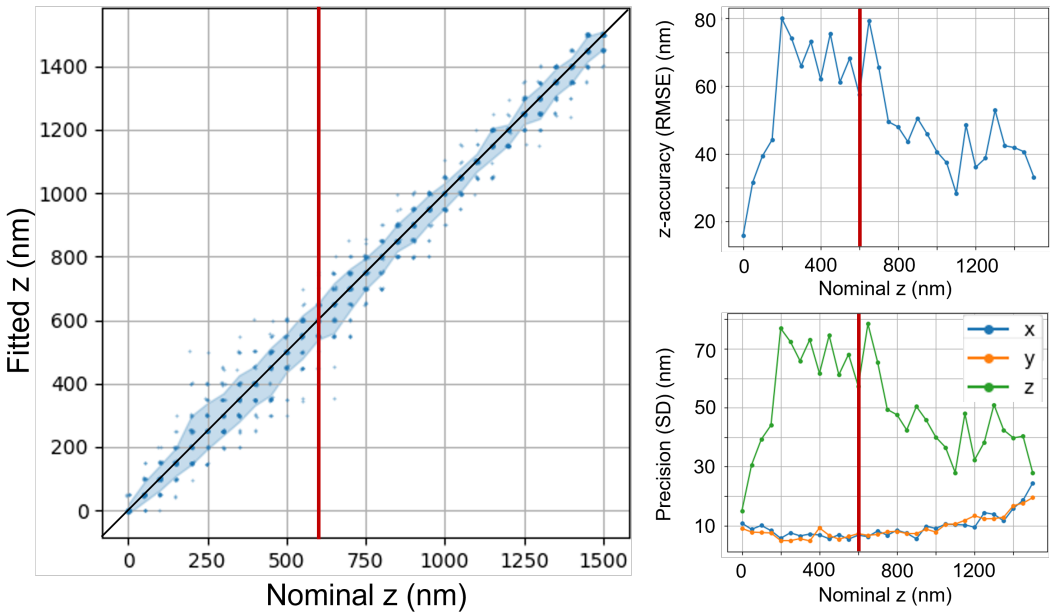

Figure 1.35: z-localization, accuracy, and precision of a fixed PbS/CdS QD when the DG is placed 150 μm far from the IP. Red line indicates where the focus occurs.

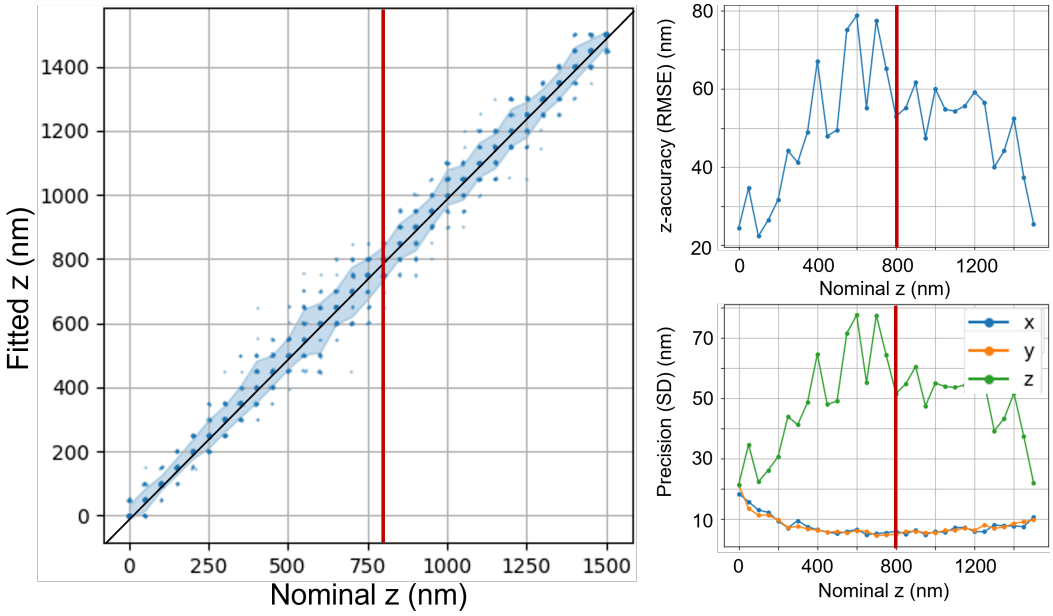

Figure 1.36: z-localization, accuracy, and precision of a fixed PbS/CdS QD when the DG is placed 175 μm far from the IP. Red line indicates where the focus occurs.

Fig.1.36 presents the z-localization, accuracy, and precision of a fixed PbS/CdS QD when the DG is placed 175 μm far from the IP. z accuracy and precision are $\sim$50 nm at focus, and for a region of $\sim$1 μm around it, both present values going from 45 - 80 nm, same as in Fig.1.35. However, now that the DG is at 175 μm from the IP, the resolution reaches values below 60 nm for more positions in z. This is the reason why we have chosen this position, 175 μm from the IP, as the optimal position of the DG to reach the highest z resolution possible for a range of 1 μm around the focus. Remarkably, the z resolution acquired (50 nm) is ten times better than the diffraction limit, which is 500 nm for 1000 nm as emission wavelength. It is relevant to observe that the setup performance is also satisfactory with the DG is at 150 μm from the IP, meaning that this position could also be used for 3D super-resolution localization.

Fig.1.37 exhibits how the interterference pattern looks at 175 μm in comparison to Fig.1.31.

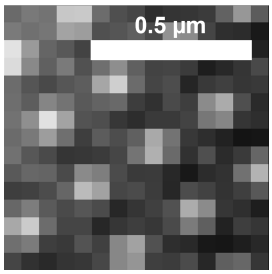

Figure 1.37: Image of interferogram when DG is placed at 175 μm, which has been determined as the ideal DG position for 1000 nm emission wavelength.

1.2.5 Configuration of SELFI optical system for near-infrared and far-red emission wavelengths

We recapitulate here the configuration that will be used for the rest of this thesis project. The SELFI optical setup is composed by the sCMOS Kuro camera, and the relay with magnification of 3.3$\times$ due to its performance clean from aberrations and large field of view, ideal when performing single-particle tracking. Using the Kuro camera also offers the advantage of being able to do experiments not only in the NIR but also in the far-red range of wavelengths.

The optical setup for NIR SELFI is shown in Fig.1.38. In general terms, this is how an experiment with SELFI is performed: the sample is excited with a laser (845 nm for SWCNTs). Then, the fluorescent emission (985 nm for SWCNTs) is collected through the objective. The 2D phase-only diffraction grating, placed $\sim$ 175 μm from the imaging plane of the microscope, creates replicas of the PSF that will interfere between each other and create an interference pattern. After, the relay corrects the magnification of the image, now being $60 \times 3.3\times = 198\times$, to achieve 3D

super-localization. Then, the signal is detected by the sCMOS KURO camera.

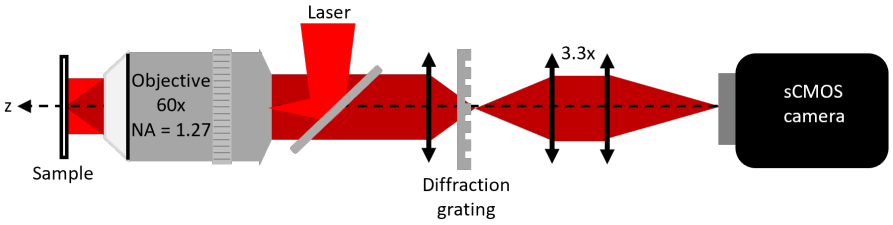

Figure 1.38: SELFI optical setup.

Notably, when measuring the SELFI PSF size in comparison with the size of a normal PSF, there is no considerable broadening of the PSF induced by the interference generation. For PbS/CdS QDs (emission at $\sim$ 1000 nm), the PSF size is:

$$DL = \frac{1.22\lambda}{2NA} \sim 500\,\text{nm},$$

for $NA = 1.27$, while in Fig.1.39 we observe that, experimentally, the PSF size is $\sim$ 600 nm.

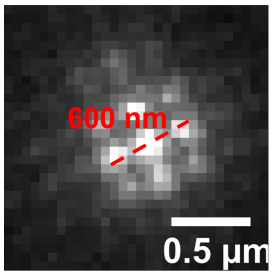

Figure 1.39: Image of a PbS/CdS QD observed through SELFI setup. $FWMH = 600$ nm.

1.3 Performance characterization of three-dimensional localization of nanoparticles

We now assess the performance of 3D localization with SELFI. In particular, we focus on the resolution that can be achieved with this optical setup. We present here two methods to determine the resolution: first, the precision through the calculation of the standard deviation (SD); and second, the accuracy defined as the root mean square error (RMSE). In the following, we characterize SELFI by using spherical QDs that emit in the near-infrared regime, i.e. PbS/CdS QDs. The choice of using QDs instead of carbon nanotubes is not to be biased by the one-dimensional geometry of SWCNTs, even though we frame this project to the localization of short nanotubes ($\sim$ 100 - 500 nm). The properties of PbS/CdS QDs will be described in section 1.3.1. We decided

not to continue our experiments with them because their signal is significantly dimer than the signal of SWCNTs, making them unsuitable for deep-tissue imaging.

Although our first aim is to work with carbon nanotubes that might emit at $\lambda > 1000$ nm in the near infrared, we took the opportunity to work with a good detector (sCMOS Kuro) in the visible regime as well, allowing us to extend this characterization to the far-red. This allows us to evaluate the robustness of the system to multiwavelengths, opening opportunities for other cellular imaging applications. In the far-red wavelength of emission, we have used TetraSpeck nanobeads, which emit at ~ 680 nm. These results are presented in section 1.3.2.

1.3.1 SELFI in the near infrared emission range

1.3.1.1 PbS/CdS quantum dots properties

The optical setup we have built has been optimized for NIR wavelengths. Due to this reason, we used PbS/CdS (lead (II) sulfide/cadmium sulfide) quantum dots emitting in this wavelength to characterize the performance of SELFI. In the present section, we introduce the properties and characteristics of these fluorophores. Fig.1.40 displays an image of these QDs when they are excited with an 845 nm laser. This image was obtained with a widefield microscope and a Ninox camera, meaning there is no self-interference in this image.

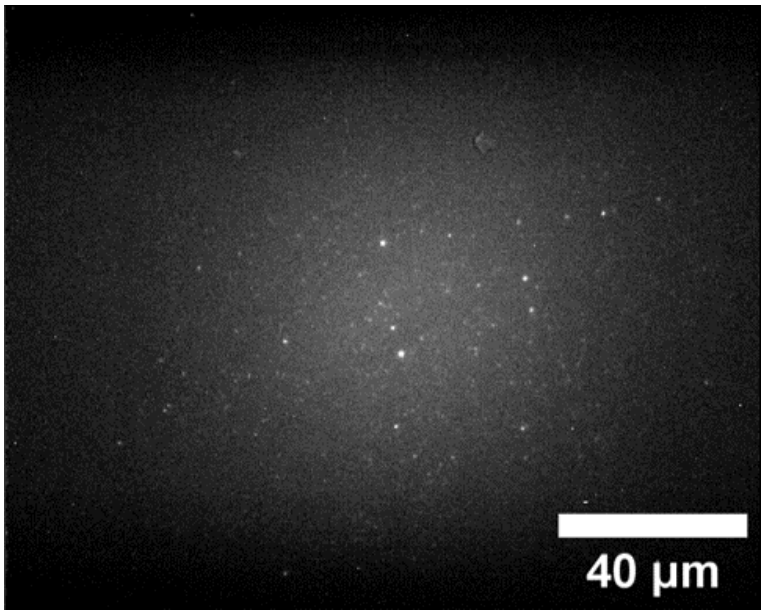

Figure 1.40: PbS/CdS QDs excited with an 845 nm laser, and imaged with a widefield microscope and Ninox camera.

PbS/CdS QDs have a core/shell structure. They are also coated with amine (-NH_2) surfactant, which is hydrophilic, making the QDs soluble in water and bio-

compatible. Their diameter is < 10 nm, and their emission peak is ~ 1040 nm when excited with an 845 nm laser, as shown in the colormap of Fig.1.2.

PbS/CdS QDs are produced by NanoOptical Materials Inc, a company based in California, United States. These QDs were acquired by our team during the Covid-19 pandemic, so we faced accessibility issues to obtain the QDs due to the distance from the delivery country to France. Unfortunately, during the shipping process, they have been damaged due to improper temperature conditioning, affecting their coating and solubility. This was reflected in their poor brightness as well as in a tendency to aggregate. What is more, we could not buy a second batch of these QDs during the course of this thesis due to the complex world situation.

Despite the fact that the QDs were not in their ideal state, their performance was sufficient to calibrate the optical setup. Some of them might have been forming aggregates, but still they were punctual clusters, which is good enough for the purpose of characterization. Nevertheless, due to the damage, they were used exclusively on surfaces, not in suspension.

1.3.1.2 Sample preparation

In order to characterize the NIR SELFI setup, we imaged fixed QDs. The samples were prepared in the following way: first, QDs are diluted in water to a concentration of 1:2000. Then, this solution is sonicated for 15 mins to homogenize it. After, on a coverslip, the solution is spincoated for 2 mins with a velocity of 920 RPM. Fig.1.41 exhibits a simple graph of how the sample of immobile QDs is made.

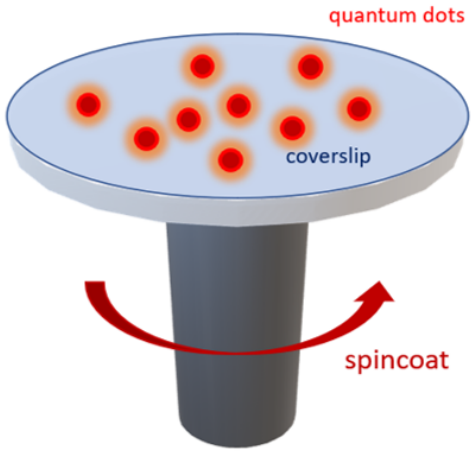

Figure 1.41: Sample preparation of fixed QDs.

1.3.1.3 Imaging and analysis protocol

Once the sample is prepared, we proceed to imaging. First, we image a bright QD centered in the field of view, which is later used for calibration. This will be referred as

the *calibration QD*. A z-stack is acquired from -750 nm to +750 nm around the focus of the QD image in steps of 50 nm, Fig.1.42. For each position in z, 30 images are taken by using an exposure time of 150 ms. The motorization of the microscope, allowing the objective to move, produces the z-stack by staying in each position until the 30 images are taken, only after this the objective shifts to the following position. Then, the analysis code is run in this QD to produce a look-up-table of Fourier transforms for each position in z. After, we localize this very same QD with the look-up-table of FTs produced with its own images. In that way, we first evaluate if the analysis code is able to compare identical FTs and give the correct z-positions. Once this is verified, this QD is considered as the calibration QD, and its FTs' look-up-table is now the calibration table. As explained in section 1.1.4, we utilize the calibration table to localize the rest of QDs. After, we image the QDs that we actually interested in localizing.

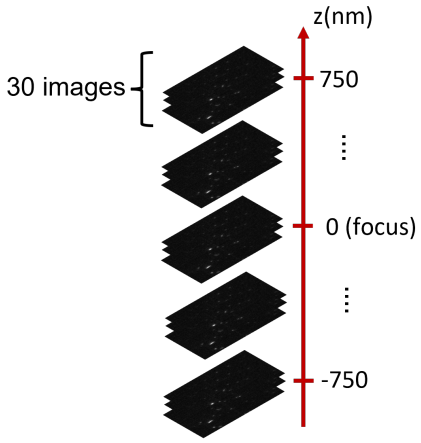

Figure 1.42: z-stack generation by moving the objective in steps of 50 nm along the optical axis.

The QDs to localize are other QDs also fixed to the coverslip surface. They are imaged in the same way as the calibration QD, i.e. z-stacks are produced by taking 30 images per z-position, and by using an exposure time of 150 ms. For each QD, we calculate the Fourier transforms of the z-stack, and they are compared with the calibration table. If the QD in question is well localized, then the analysis exhibits a match between the z-positions of both the QD to localize and the calibration QD.

1.3.1.4 Results and discussions

In the following lines, we discuss the results obtained after localizing QDs with NIR SELFI setup. Fig.1.43 shows the z-localization, precision, and accuracy of the bright calibration QD ($\sim$ 10800 photons). Let's recall that Nominal z is the z-positions given by the microscope as we control it to move in along s. Fitted z is the z-localization

resulted from our SELFI analysis code. A good localization would show a match between the Fitted z values and the Nominal z values for a range of ~ 1 μm around the focus, which in this case happens around Nominal z = 600 nm. As observed in the figure, the (x, y) precision is < 10 nm. The z precision is of $\sim 40 - 80$ nm, same as the accuracy. Fig.1.44 exhibits the interfringe interfringe$_x$ and interfringe$_y$ as functions of z. We can notice that for each z-position, there is a unique value for interfringe$_x$ and interfringe$_y$. In fact, there is a difference of 0.5 pixels equal to 28 nm between the smallest peak-to-peak distance (~ 2.9 pix.) to the biggest (~ 3.4 pix.).

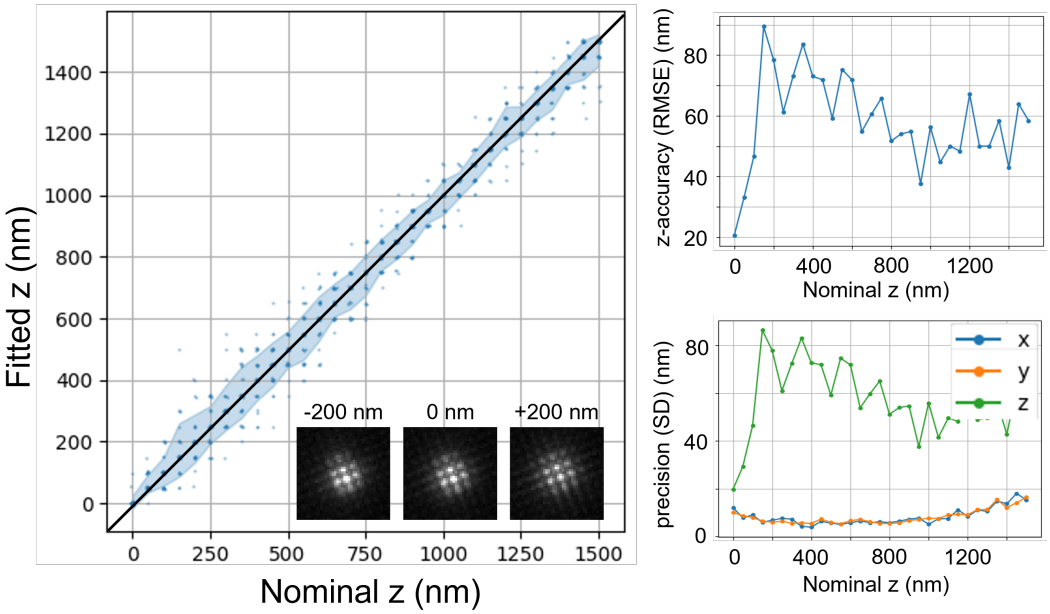

Figure 1.43: z-localization of a PbS/CdS QD fixed in the center of the field of view, the accuracy and precision are also shown. The number of photons in the signal is 10800.

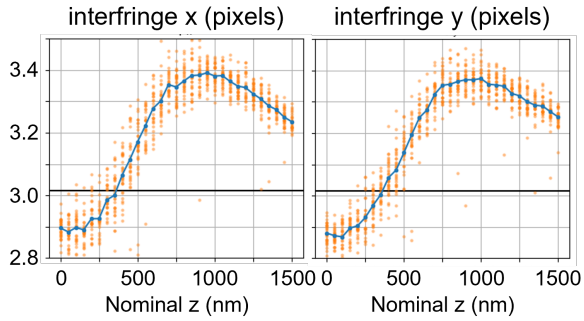

Figure 1.44: Distance (in pixels) from peak-to-peak in the interference pattern inside the PSF of a quantum dot vs. z.

Effect of the number of photons on the resolution

After performing the calibration, different QDs also centered in the field of view were localized, but now excited with different intensities to evaluate the resolution of NIR SELFI with respect to the number of photons emitted by the fluorescent sample. The images of the QDs were acquired in the same way as the calibration QD. Meaning that for each of them a z-stack of 30 images per z-position was taken with 150 ms as exposure time. These QDs were localized by using the calibration table produced, Fig.1.45 shows some examples of the results obtained. We can observe how the resolution ameliorates when the signal is stronger.

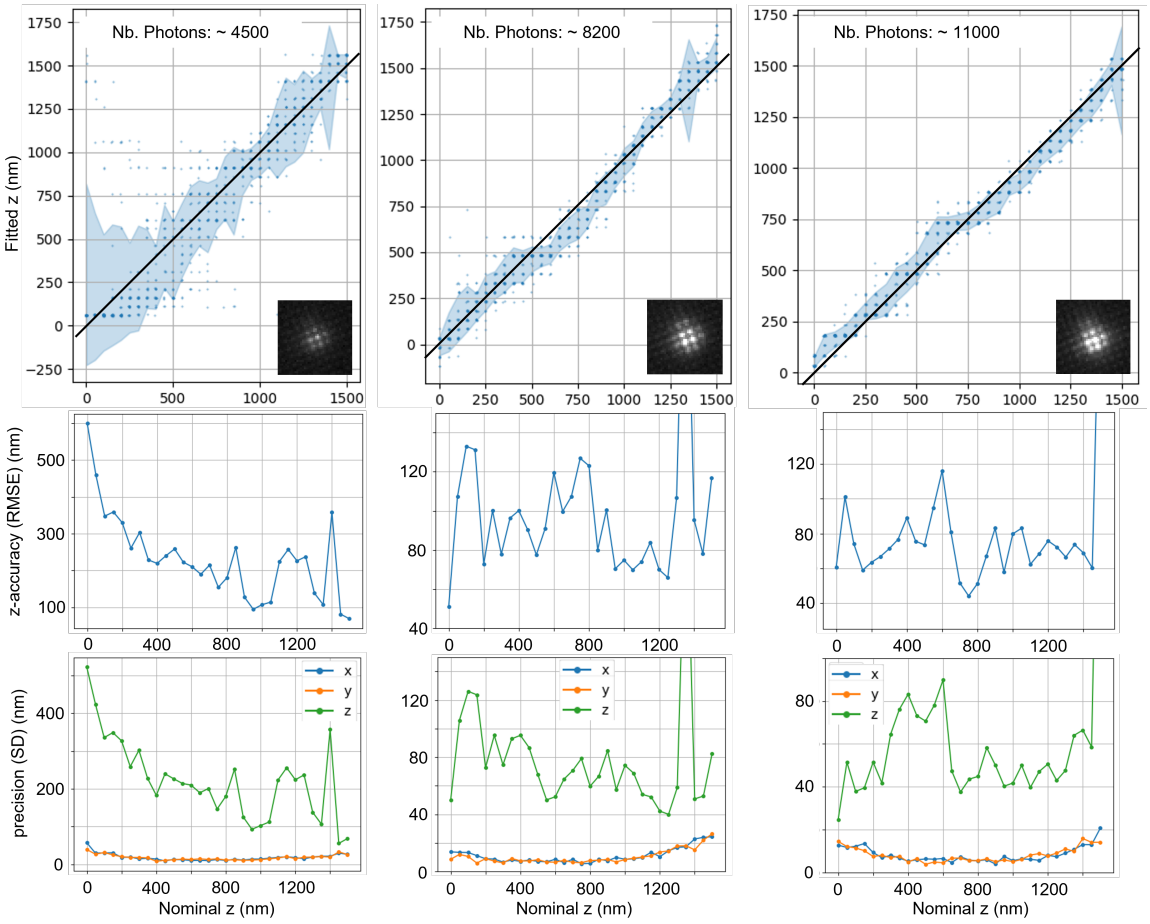

Figure 1.45: z-localization of PbS/CdS QDs fixed in the center of the field of view, but different number of photons emitted. The brightness of the signal was controlled by modulating the excitation laser intensity.

For each localized QD in Fig.1.45, if we average the RMSE values for a region of 1 μm in z centered at the focus, the axial accuracy values are 206 nm for a signal of 4500 photons, 90 nm for 8200 photons, and 73 nm for 11000 photons. By doing the same average of SD values, we have a precision of 200 nm for 4500 photons, 68 nm for 8200 photons, and 56 nm for 11000 photons. Therefore, the dependence of

the resolution on the photon budget is strong. These average calculations portray which is the average resolution of that 1 μm region since both precision and accuracy change por each z-position due to signal fluctuations.

60 QDs were imaged in total in order to analyze the dependency of the resolution on the signal. Fig.1.46 displays the experimental z-localization precision (exp. prec.) and accuracy (exp. accu.) as a function of the photon budget. Each point in the plot was calculated by averaging the SD or RMSE for a z-range of 1μm around the focus, in the same way as discussed above. Note that the precision and accuracy are both below 100 nm when the number of photons is higher than 8000.

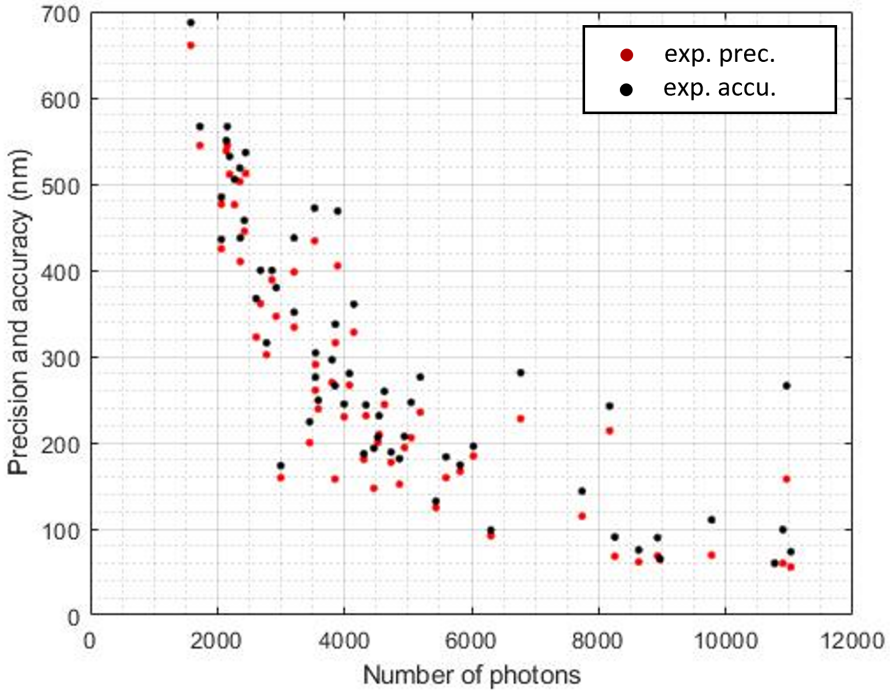

Figure 1.46: z-localization precision and accuracy of NIR SELFI as functions of the photon budget.

Fig.1.47 is the logarithmic plot of the resolution vs. the number of photons. The power law fit (fit prec. and fit accu.) shows that the resolution does not depend on the inverse square root of the photon budget (precision and accuracy $\propto$ (number of photons)$^{-0.5}$), as it would be expected by shot noise limited detection, but rather on the inverse of the photon budget as when the localization precision is limited by the background noise, as discussed in section 1.1.1 [65]. More precisely, the dependence are: precision $\propto$ (number of photons)$^{-1.18}$, and accuracy $\propto$ (number of photons)$^{-1.04}$. This effect may be caused by background coming from the camera, or any other source of background, such as out-of-focus fluorescence, etc, as supported by references [65] and [2], and explained in section 1.1.1 in detail.

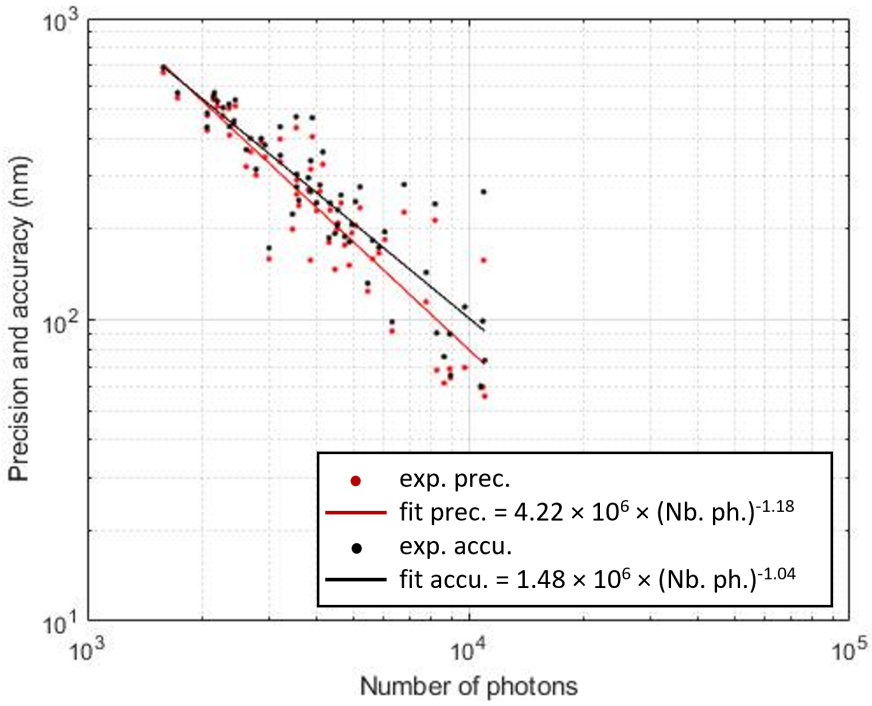

Figure 1.47: Logarithmic plot of z-localization precision and accuracy of NIR SELFI as functions of the photon budget.

Effect of the distance from the center of the field of view on the resolution

We now image QDs fixed in different positions spread along the field of view in order to evaluate the localization resolution of NIR SELFI as a function of the distance from the center of the field of view, Fig.1.48.

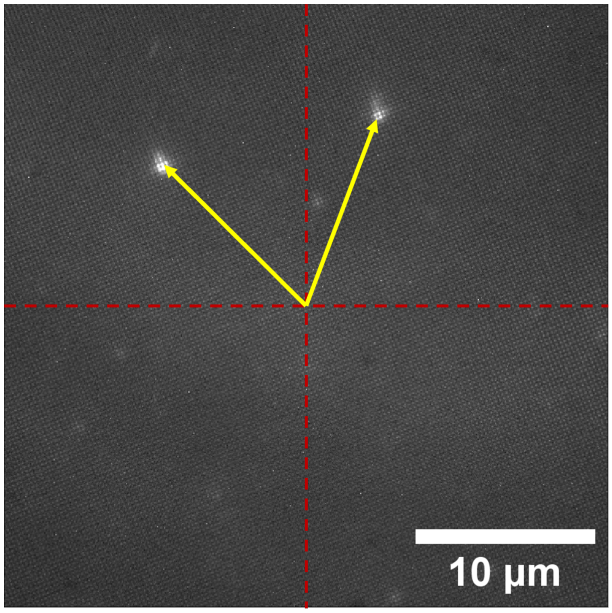

Figure 1.48: Two QDs located far from the center of the camera field of view.

Fig.1.49 displays the localization of three different QDs positioned at 0.5 μm, 11 μm, and 21.7 μm from the center of the camera field of view while their signal is the same for the three of them, 5500 photons. Once more, the acquisitions consisted on z-stacks of 30 images per z-position using an exposure time of 150 ms. For each localized QD in Fig.1.49, we average the RMSE values for a region of 1 μm in z centered at the focus. Same thing is done with the SD. Among this 1 μm region, the accuracy is 134 nm for a distance of 0.5 μm, 183 nm for 11 μm, and 168 nm for 21.7 μm. Whereas the precision is 132 nm for 0.5 μm, 150 nm for 11 μm, and 158 nm for 21.7 μm.

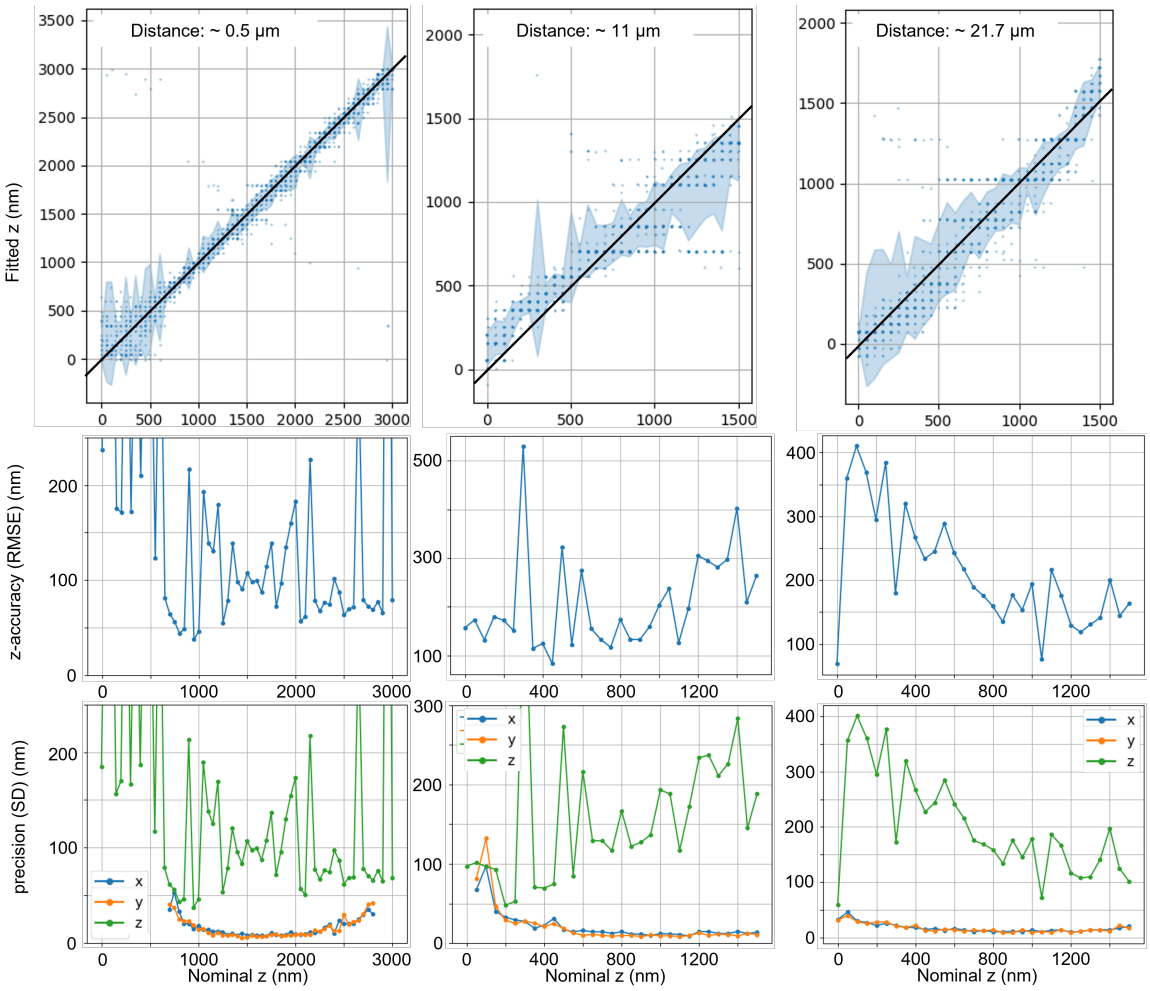

Figure 1.49: z-localization of PbS/CdS QDs fixed in different positions

To have a better understanding on how the resolution varies as a function of the distance from the field of view, we localized 43 QDs located all along the field of view. Again, the photon budget remains 5500 photons for all the QDs. Fig.1.50 shows the experimental precision (exp. prec.) and accuracy (exp. accu.), which is the averaged SD and RMSE over a 1 μm region around the focus, respectively. We note that the precision only depends on the number of photons but not on its localization

from the center, whereas the accuracy does depend on both number of photons and distance from the center. From Fig.1.50 we can observe that the precision remains quasi-constaint, going from $\sim$ 130 - 140 nm, while the accuracy is $<$ 210 nm for distances $<$ 15 μm from the center. Our interpretation of the increase of inaccuracy compared to precision is that is a consequence of the presence of optical aberrations as they increase as we move further from the center, such as comma, Fig.1.51, leading to a small deformation of the fringes in the interferogram which is reflected in the information held in the Fourier transforms. Noteworthy, we have a working field of view of 30 μm, practical for single-particle tracking experiments.

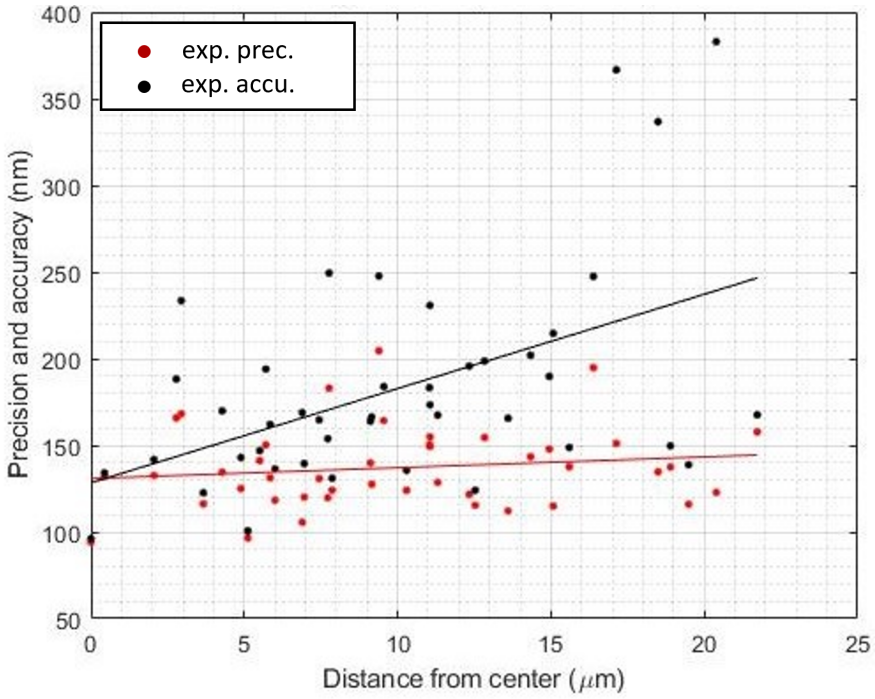

Figure 1.50: Localization precision and accuracy of NIR SELFI as functions of the emitter distance from center of the field of view for 5500 photons.

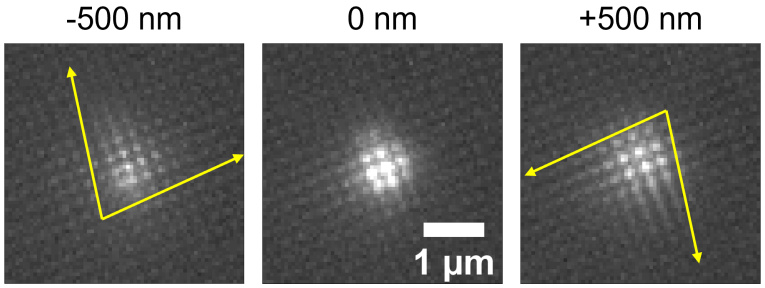

Figure 1.51: Comma aberration present in the NIR SELFI setup.

1.3.2 SELFI in the far-red emission range

We now evaluate the performance of the NIR SELFI setup for far-red wavelength emission. As mention before, we are able to do so thanks to the camera we are using since it is also suitable for visible wavelengths. In the following sections, we introduce the nanobeads used during this characterization, which are TetraSpeck. After, we discuss the sample preparation as well as the imaging procedure. Finally; we discuss the results obtained.

1.3.2.1 TetraSpeck nanobeads properties

The fluorescent emitters used in this section were TetraSpeck nanobeads (TS) from ThermoFisher scientific. They present a diameter of 100 nm. They have four peaks of emission. However, we use the emission peak occuring at $\sim$ 680 nm when excited with a 660 nm laser. Fig.1.52 shows fixed TetraSpecks spread along the field of view. This image was produced with a widefield microscope, a 660 nm laser, and a ProEM camera, therefore there is no self-interference in this image.

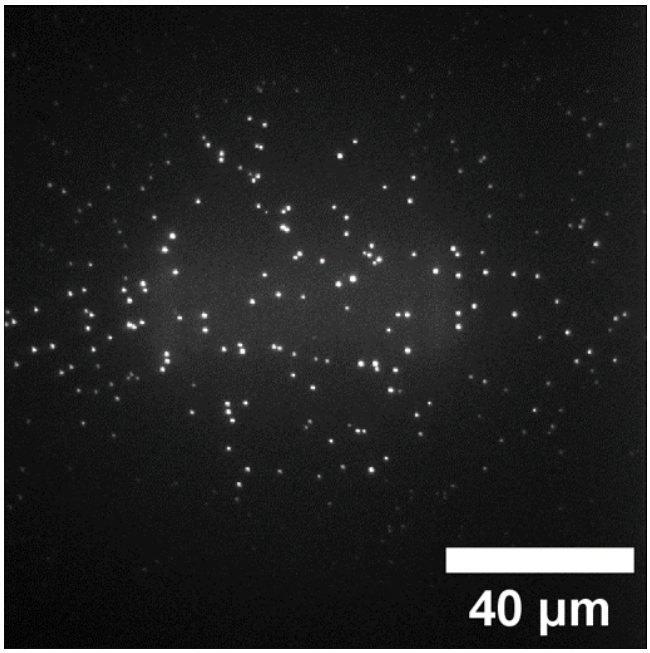

Figure 1.52: TetraSpecks excited with an 660 nm laser, and imaged with a widefield microscope and ProEM camera.

1.3.2.2 Sample preparation

To characterize the NIR SELFI setup for far-red emission, we imaged TetraSpeck nanobeads. To prepare the sample, we first dilute the TetraSpeck in water to achieve a concentration of 1:4. Then, the solution is homogenized by sonicating it for 15 mins.

After, 2 μL of solution is put on a coverslip with other 2 μL of PBS (phosphate-buffered saline), the latter enables the nanobeads to stick to the surface, fixing them among the coverslip. The sample preparation is displayed in the schematics of Fig.1.53.

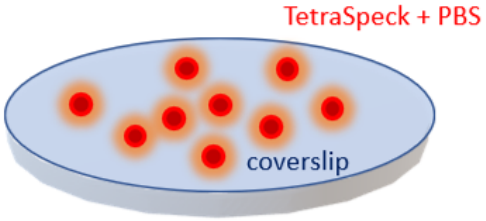

Figure 1.53: Sample preparation of fixed TetraSpecks.

1.3.2.3 Imaging and analysis protocol

The imaging and analysis protocol is performed in the same way as for the QDs, and it is described in section 1.3.1.3, but using an exposure time of 50 ms. There is also another difference, and this one is fundamental: the position of the diffraction grating is not the same as for NIR emission wavelength. To perform the following set of experiments, we have changed the position of the DG to optimize it for far-red emission. As mentioned before, the DG ideal place for NIR is $\sim$ 175 μm from the image plane, whereas the optimal place of the DG for far-red wavelengths is $\sim$ 150 μm. Noteworthy, it is easy to pass from one position of the DG to another since the DG holder allows the motion of the DG along the optical axis with micrometric precision. Therefore, to achieve multicolor SELFI, it will be required to move the DG from one position to another.

1.3.2.4 Results and discussions

Given the fact that the DG position is not the same for NIR as for far-red emission, we expect to see a difference in the interfringe. Fig.1.54 shows precisely that, is displays how interfringe$_x$ and interfringe$_y$ evolve as functions of z when using the NIR SELFI setup on far-red emission. When compared to Fig.1.44, we observe that the difference between the smallest and biggest interfringe is different, being 0.5 pixels for NIR emission, and 0.25 pixels for far-red emission.

Fig.1.55 exhibits the z-localization and resolution when localizing the calibration TS by using itself during the analysis, similar to what was done with QDs. The (x, y) precision is $\sim$ 5 nm, while in z is $<$ 50 nm. The z accuracy is $<$ 60 nm. All this when the number of photons is 10000. When comparing these results with the ones obtained with QDs, it is found that the resolution of TSs is similar to the one obtained with QDs even though the setup was designed for NIR emission. Therefore,

we can conclude that the SELFI NIR setup is robust for both far-red and NIR. This is due to different reasons, first, the DG was initially costumized for visible wavelenght, making it ideal for far-red, as well as the fact that the process of axial localization only depends on the interferogram produced by the DG, independent of the PSF size, therefore achromatic.

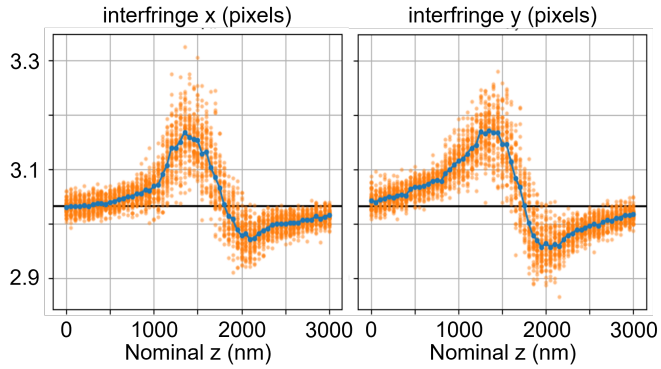

Figure 1.54: Interfringe inside the PSF of a TetraSpeck as a function of z. Among the z values, 1500 nm represents the focus.

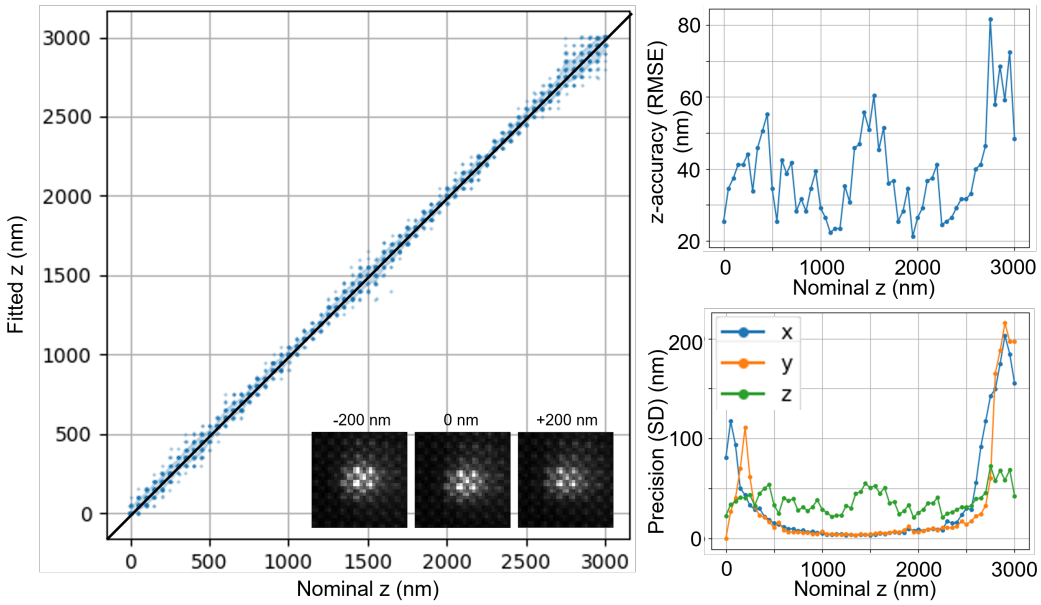

Figure 1.55: z-localization of a TetraSpeck in the center of the field of view used for calibration, more than 10000 photons.

The calibration TS was then used to localize itself when excited with different intensities in order to observe the dependency of the localization performance as a function of the photon budget. Fig.1.56 portrays some examples on how the z resolution decreases as the photon budget drops, while the (x, y) resolution barely changes. As observed, a signal of $\sim$ 8300 photons has a z RMSE $<$ 100 nm and SD

< 75 nm, ~ 6000 photons shows a z RMSE < 200 nm and SD < 125 nm, and ~ 3500 photons a z RMSE < 500 nm and SD < 250 nm.

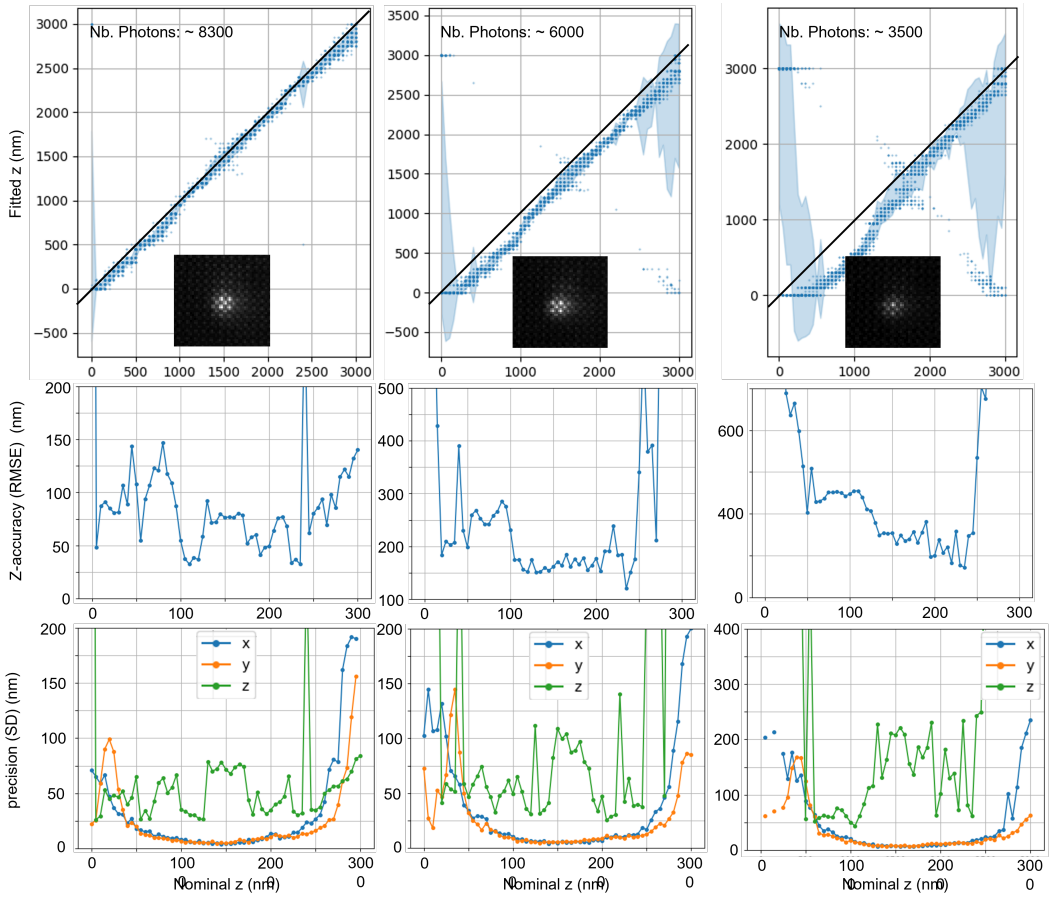

Figure 1.56: z-localization of the same TetraSpeck in the same position in the field of view, but different number of photons emitted. The brightness of the signal was controlled by modulating the excitation laser intensity.

Chapter 2

Analysis method for SELFI 3D super-localization

In the present chapter, we expose the strategy developed to analyze 3D localization of fluorophores observed through the NIR SELFI setup. The analysis code was written in Python, and developed by Antony Lee with the help of Pierre Bon, who were members of our research team. As it was discussed in section 1.1.2, a single image produced with SELFI encloses information regarding both intensity and phase of fluorescent light emitted by the sample and collected by the detector. Analysis of this image allows to super-localize single emitters in (x, y) by means of the intensity, and in z by the phase. More precisely, let's recall the discussions of section 1.1.4, where we showed that, given a SELFI PSF image experimentally obtained, the lateral super-localization is obtained by fitting the intensity distribution of a PSF to a Gaussian as a good approximation of the actual PSF shape (Airy disk): the centroid of the Gaussian corresponds to the (x, y) position of the emitter. To retrieve the axial position, we compare the image Fourier transform (FT) to a look-up-table of Fourier transforms produced from a z-stack of images of a calibration fluorophore. This is possible since the phase changes with the axial (z) position of the emitter, the Fourier transform itself is different for each position in z. All this process is encoded in our analysis script, and it will be explained in the following pages.

In section 2.1, we study the different parts encompassing a self-referenced image, such as background of the image, intensity profile of the signal, and interferogram. This enables us to create an algebraic model that describes the images experimentally obtained with SELFI. We end this section by listing the parameters that form part of this model, and that must be determined to have an optimal fitting function. In section 2.2, we explain the method we use to find optimal converging parameters, which is non-linear least square fit. We also explain how the lateral localization of the emitter is determined. Finally, in section 2.3, we illustrate the method to determine the axial localization of the emitter, which is based on the use of Pearson coefficients.

2.1 SELFI image model

To understand how the analysis script is constructed, let's consider a z-stack of images of a fixed point-like emitter (such as PbS/CdS QDs or SWCNTs) acquired by the SELFI NIR setup while the focusing point is varied in regular steps systematically. Fig.2.1 shows a self-interfered image of a single emitter.

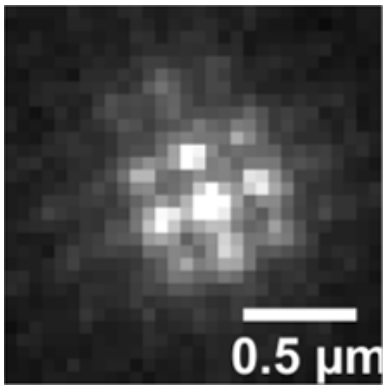

Figure 2.1: Experimental self-interfered PSF image of a PbS/CdS QD.

This image is composed by two elements, the PSF signal constituted by a distribution of intensity that "envelopes" the distribution and can be approximated to a Gaussian, and background. Both of them, PSF and background, present interference that looks like a chessboard (black and white squares), caused by the diffraction grating in the setup. However, the background has fringes which correspond to ∼zero wavefront curvature, whereas the PSF (emitter's signal) has fringes that correspond to nonzero wavefront curvature. Any SELFI PSF image can be thought as the following sum of contributions:

$$\begin{aligned} &\text{Image} = \text{signal} \times \text{fringes} + \text{background} \times \text{fringes}, \\ &\text{where} \quad \text{signal} = \text{normalized Gaussian} \times \text{amplitude}, \end{aligned} \tag{2.1}$$

and it is represented in the scheme of Fig.2.2. This representation of SELFI PSF images allows us to separate four elements of the image makes it easier to create the model that represents and fits these images during the analysis process. The first element is a normalized Gaussian multiplied by a certain amplitude, and multiplied by an interferogram. We also add the contribution of the background, multiplied by the interferogram as well. Background and its different causes are discussed in section 1.1.1. In our model, background and signal amplitude are set parameters that can be extracted from the acquired images. Our focus then goes to the modeling of the 2D Gaussian function and the interferogram. In sections 2.1.1 and 2.1.2, we define the different systems of references and functions that will enable us to fulfill these tasks.

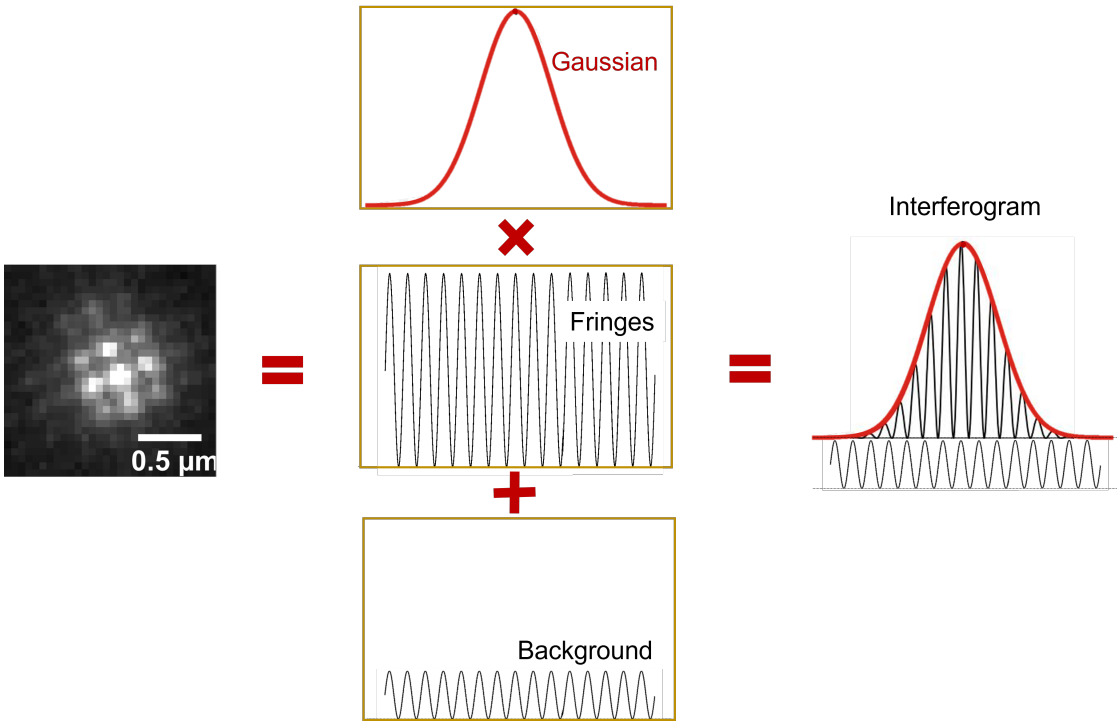

Figure 2.2: SELFI PSF image composed by a Gaussian envelope with fringe modulation coming from interference plus a background which presents interference as well. Although, background fringes are not the same as PSF fringes as the interferogram is deformed by the wavefront curvature.

2.1.1 Modelization of intensity distribution

In the present section, we model the 2D Gaussian that resembles the PSF envelope. To do so, we first introduce some system of coordinates to define emitters' positions within experimental images. In this way, the Gaussian modeling is straightforward.

From a z-stack of images acquired experimentally, let's consider an emitter to localize. Its PSF center is at position (i_0, j_0) in respect to the origin of the image, which is in the upper left corner, as displayed in Fig.2.3, and (i, j) is the position of any pixel in this system of coordinates. Note that i_0 and j_0 are not integers but the super-resolved position of the emitter, whereas i and j are integers. The image is then cropped around the center of the PSF so that its size is 30×30 pixels since that area corresponds to the PSF extent. In the cropped image, we can define a new system of reference where the position of any pixel in the PSF is (i_c, j_c), and is given by

$$i_c = i - i_0, \quad j_c = j - j_0. \tag{2.2}$$

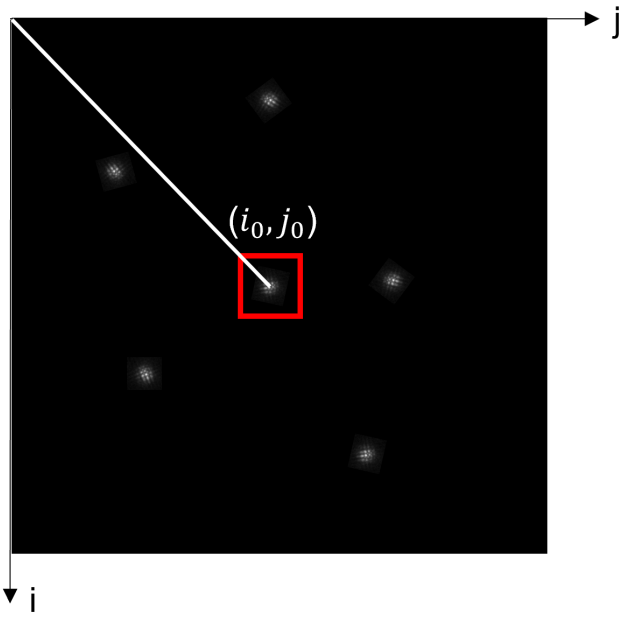

Figure 2.3: System of reference in an image. Its origin is in the upper left corner of the image. (i_0, j_0) is the position of the center of the emitter to localize.

Fig.2.4 shows the experimental image of the emitter, which is often elliptical due to the presence of optical aberrations or because of their 1D geometry in the case of small SWCNTs that might be slightly longer in one direction. Therefore, we have built the model by considering elliptical PSF shapes, where circular PSFs are a particular case. Since the ellipse has an orientation, we can define a system of reference (a, b) which is rotated by an angle θ_{PSF} with respects to the (i, j) reference system. In this new system of coordinates, (i_c, j_c) becomes (a, b) under the transformation

$$\begin{aligned} a &= i_c \cos\theta_{PSF} - j_c \sin\theta_{PSF} \\ b &= i_c \sin\theta_{PSF} + j_c \cos\theta_{PSF}. \end{aligned} \tag{2.3}$$

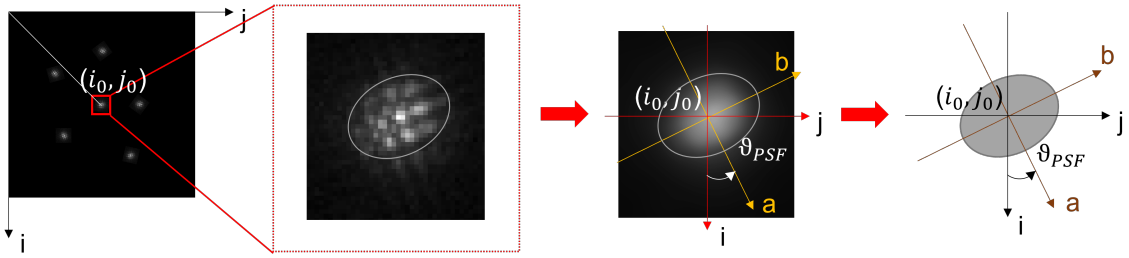

Figure 2.4: A given PSF in a SELFI image is analyzed for localization. There are two reference systems: (i, j) the coordinate system of the image, and (a, b) in alignment to the orientation of the elliptical PSF.

We now are able to approximate the signal to a Gaussian with different widths in both a and b directions in the system of reference of the ellipse:

$$\text{Gaussian}(a,b) = \exp\left[-\left(\frac{a^2}{2\sigma_a^2} + \frac{b^2}{2\sigma_b^2}\right)\right]. \tag{2.4}$$

2.1.2 Modelization of self-referenced interferograms

In the present section, we model the interferogram, and to do so it is important to remember that to get better resolution of the interference pattern imaged in the detector, the diffraction grating is placed with an angle shift, θ, with respect to the pixels web in the camera to avoid the match of the fringes ends with the pixels edges and lose information. We normally choose θ to be $\sim 20°$. In section 2.2, we show how to determine θ from experimental images. We now define a fourth system of coordinates, (x, y), aligned with the interferogram, as shown in Fig.2.5. θ then is the shift angle of the (x, y) system of coordinates with respect to the (i_c, j_c) system.

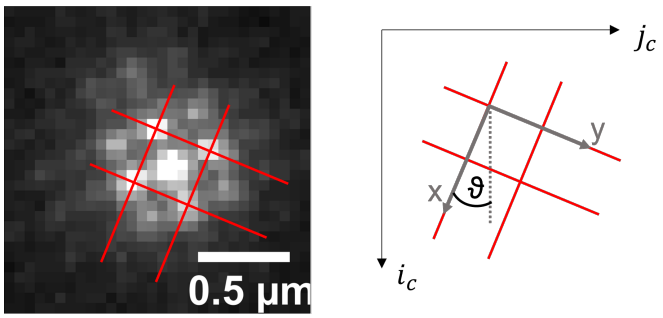

Figure 2.5: SELFI PSF image produced experimentally. (x, y) system of reference is shifted by θ in respect to (i_c, j_c).

Similarly, we introduce a coordinate transformation with the purpose of making an easier description of the interferogram model:

$$\begin{aligned} x &= i_c \cos\theta - j_c \sin\theta \\ y &= i_c \sin\theta + j_c \cos\theta. \end{aligned} \tag{2.5}$$

To arrive to a 2D equation that describes the interferogram profile experimentally observed in the camera, let's start by the easiest case, which is that of a 1D interferogram shaped as a cosine function:

$$\text{interferogram}(x) = \cos\left(K_x x + \phi_x\right) + \text{cte.},$$

where $K_x = 2\pi/\text{interfringe}_x = 4\pi/p$, and interfringe_x is the half periodicity $(p/2)$ of the interference pattern along the x axis. Now, to derive and equation that shapes a 2D web of fringes, it is useful to introduce the following dimensionless variables:

$$\begin{aligned} x' &= K_x x + \phi_x \\ y' &= K_y y + \phi_y. \end{aligned} \tag{2.6}$$

The full 2D interferogram equation is given by Eq.2.7, it is derived from Eq.1.10 in section 1.1.3, and it represents the contributions of the different harmonics present in the interferogram.

$$\begin{aligned}\text{interferogram}(x', y') =& 1 + a_1 \left(\cos x' + \cos y'\right) + a_2 \left[\cos\left(x' + y'\right) + \cos\left(x' - y'\right)\right] \\ &+ a_{1/2} \left[\cos\left(\frac{x' + y'}{2}\right) + \cos\left(\frac{x' - y'}{2}\right)\right]\end{aligned} \tag{2.7}$$

Now we have a fitting model that is consistent with the shape of SELFI PSFs, and is constituted by a Gaussian function (Eg.2.4) modulated by an interference pattern function (Eq.2.7) plus a background.

There are 14 independent parameters contained in the equations of this fitting model (Eqs.: 2.1, 2.4, and 2.7 with transformations 2.2, 2.3, 2.5 and 2.6), and in order to optimize it, we should optimize the values of the parameters as well. Table 2.1 is a list of the parameters, their meaning, and the equation number where they appear.

Parameters	Meaning	Part of equation
background (c)	value calculated for every image processed during analysis, and corresponds to the minimum number of photons detected by the pixels in the image	2.1
amplitude (a_0)	value linked to the signal's intensity	2.1
(i_0, j_0)	lateral location of the emitter	2.2
θ_{PSF}	orientation of the PSF ellipse with respect to the (i, j) reference system, it differs from one emitter to another	2.3
σ_a and σ_b	standard deviation of the 2D Gaussian fit in the (a, b) reference system	2.4
K_x and K_y	$4\pi/p$	2.6
ϕ_x and ϕ_y	phase shift in the interferogram	2.6
a_1, a_2 and $a_{1/2}$	modulation of the contribution of each harmonic in the interferogram	2.7

Table 2.1: Parameters in the fitting model, their definition, and the equation they are part of.

2.2 Parameters setting and lateral super-localization of single emitters

The present section is divided into different subsections where we expose how to determine (i_0, j_0) by means of lateral super-localization. After, we show how to determine the interferogram orientation angle (θ). Then, we explain the non-linear square fitting method we use to optimize the 14 independent parameters that are part of the model's equations. (i_0, j_0) is considered as another parameter since (i_0, j_0) has to be optimized too. Fig.2.6 shows a schematic of the process behind the analysis of SELFI images, and the parameters (plus θ) that will be covered in this section.

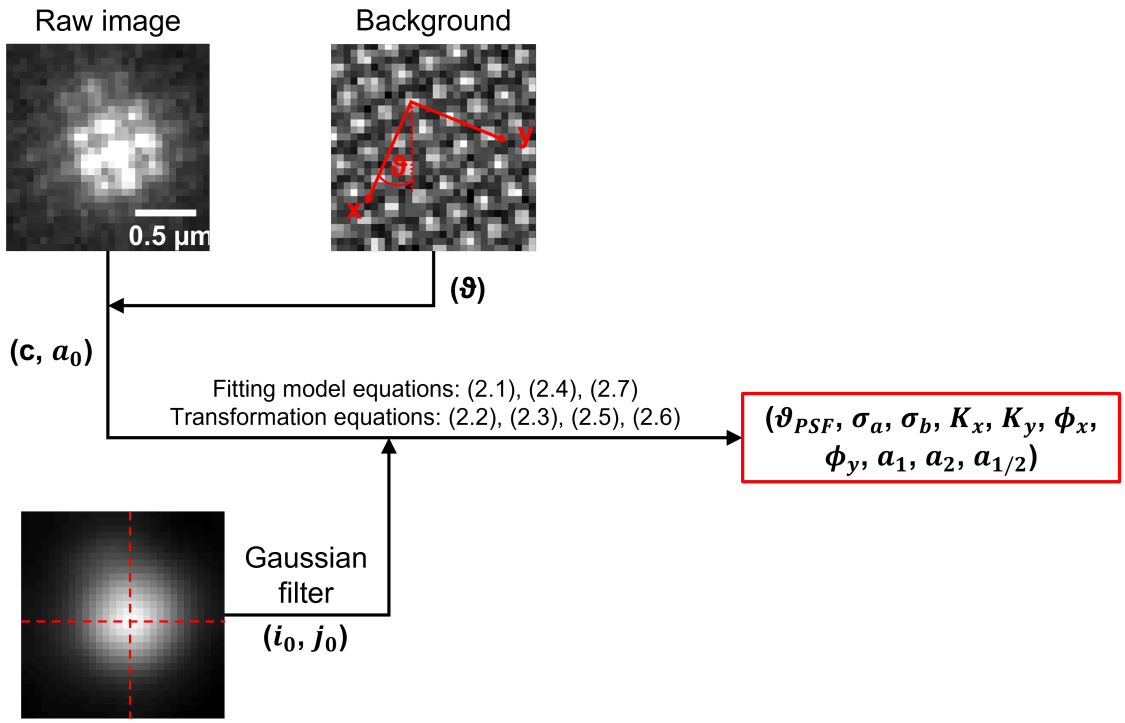

Figure 2.6: Schematics of images and equations that lead to the determination of the parameters in the fitting model.

2.2.1 Super-localization for lateral position determination

To determine the lateral position of a point-like emitter, we first apply a Gaussian filter to the image of the PSF, which is used as a low pass filter on the image to obtain the intensity profile without the interferogram modulation. Gaussian filters are widely used for image processing as low pass filters because Gaussian masks replicate optical blur (PSF profile) almost flawlessly, as demonstrated in section 1.1.2. This process is exemplified in Fig.2.7. Then, the centroid of this image can be calculated to determine an initial guess of (i_0, j_0). Finally, a non-linear least squares is used to fit the model to

the data from the experimental image and determine precisely (i_0, j_0). This process will be covered in section 2.2.3.

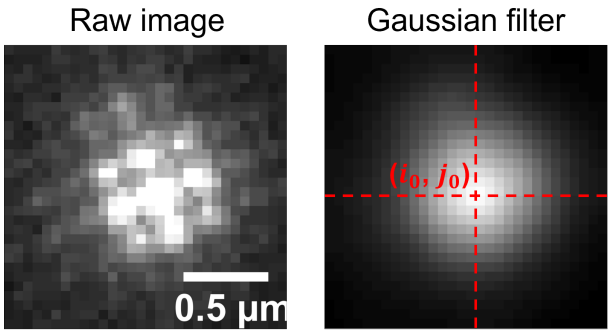

Figure 2.7: Gaussian filter applied to an image of PbS/CdS QD observed through SELFI.

2.2.2 Determination of interferogram orientation

The angle of the interferogram with respect to the axes (i_c, j_c), θ, can be retrieved in the following way: during a localization experiment, background images must be taken. With the excitation laser on and the same filters and dichroics used when imaging fluorescent emitters, we move the focus away from the emitters to have a non-contaminated image of the background. This image is then given to the analysis code, and it calculates the Fourier transform of the background, from where it determines θ. Fig.2.8 shows this process.

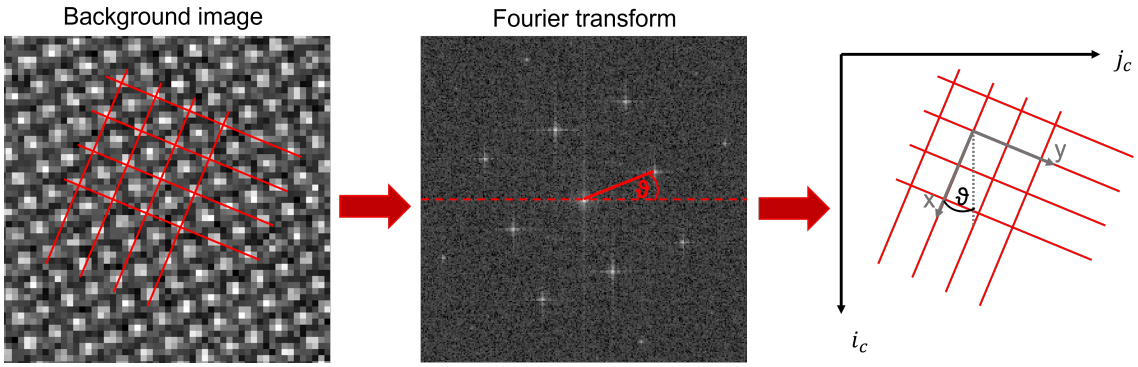

Figure 2.8: Background image with clean interference pattern. The fringes present an orientation (θ) compared to the system of coordinates of the image.

2.2.3 Non-linear least squares fitting

Non-linear least squares is a method to fit a collection of m observations with a non-linear function with n parameters $(m \geq n)$. To understand the theory behind this fitting model, let's consider m points experimentally obtained, (x_1, y_1), (x_2, y_2), ... ,

(x_m, y_m), and a function to model y, i.e. $y = f(x, \beta)$, where β is a set of parameters $(\beta_1, \beta_2, \ldots, \beta_n)$. Non-linear least squares is the process where β is optimized so that the function $f(x, \beta)$ describes in the most accurate manner the data set by using least squares, i.e. by minimuzing the sum

$$S = \sum_{i}^{m} r_i^2,$$

where $r_i = y_i - f(x_i, \beta)$ is the residual for $i = 1, ..., m$. To find the appropriate parameters, we must give an initial guess of their values. Iterative refinement of the parameters or sequential approximation yields to optimal values in order to find the best fit function $f(x_i, \beta)$ which describes the data.

From the non-linear least squares optimization, the (i_0, j_0) position of the emitter is improved from the initial guess being the Gaussian's centroid, as explained above. The rest of parameters were also refined from the non-linear least squares procedure.

Interestingly, there are some degeneracies to consider that, although they do not affect the results, they affect the plots. To understand these degeneracies, consider the parameters defining the Gaussian fit: σ_a, σ_b, and θ_{PSF}. We can notice that the rotation

$$\begin{aligned} \theta_{PSF} &\Longrightarrow \theta_{PSF} + \frac{\pi}{2} \\ \sigma_b &\Longrightarrow \sigma_a \\ \sigma_a &\Longrightarrow \sigma_b \end{aligned}$$

corresponds to the same PSF image, but rotated $\pi/2$. These type of results can take place during the determination of parameters, so to consolidate all the values of σ_a, σ_b, and θ_{PSF}, we "unwrap" θ_{PSF}, which means that: from one image to the next, $|\Delta\theta| < \pi/4$, otherwise $\pi/2$ is subtracted or added from the angle, and σ_a and σ_b are swapped back to their original orientation.

Another degeneracy occurs when

$$\begin{gathered} \phi_x \Longrightarrow \phi_x \pm 4\pi \\ \text{or} \\ \phi_y \Longrightarrow \phi_y \pm 4\pi \\ \text{or} \\ \begin{cases} \phi_x \Longrightarrow \phi_x \pm 2\pi \\ \phi_y \Longrightarrow \phi_y \pm 2\pi, \end{cases} \end{gathered}$$

since these transformations do not change the result of the fringes equation, which is a sum of cosine functions.

2.2.4 Results from the analysis process

In the present section, we show an example of the results we get after analyzing experimental images of an immobile PbS/CdS QD. All the parameters are plotted as functions of z in Fig.2.9, where c = background, a_0 = amplitude, $interfringe_x = 2\pi/K_x$, and $interfringe_y = 2\pi/K_y$.

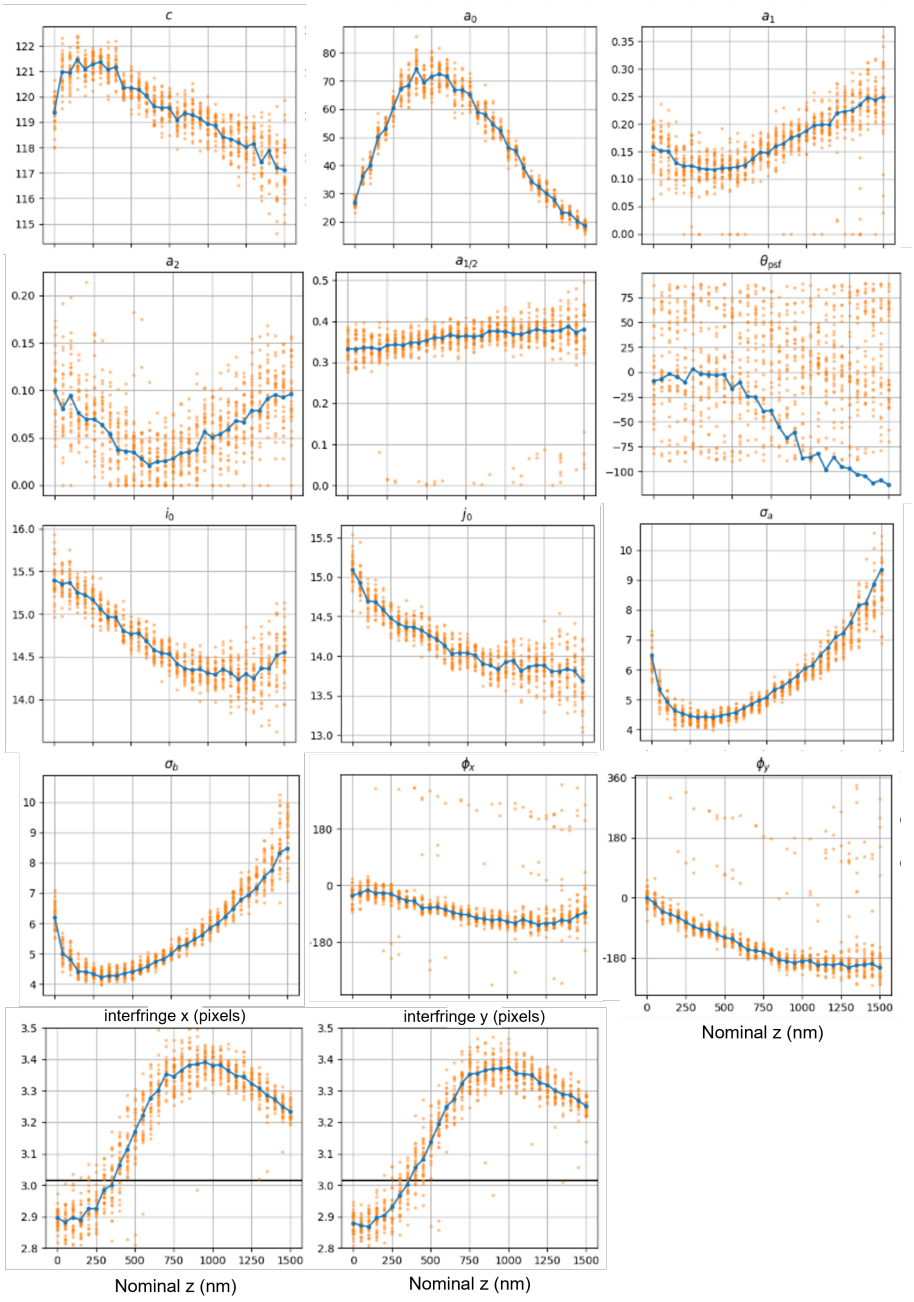

Figure 2.9: Parameters after analyzing experimental images of an immobile PbS/CdS QD. For each z position, 30 images were taken. Each orange point represents the value of a given parameter for each image. Blue points are the average values for the parameter at a certain z.

Fig.2.9 give us all the information regarding the PSF and the interferogram, such as the fact that the only parameters useful to determine the axial position of single emitters through SELFI are $interfringe_x$ and $interfringe_y$. Interfringe is the only parameter from where it is possible to obtain the axial localization since, within a range, each interfringe value corresponds to a single z position.

Fig.2.9 shows how (i_0, j_0) changes as a function of z, indicating the presence of comma in the field of view. It also shows the contribution of the different harmonics in Eq.2.7 to the interferogram through the values of a_1, a_2, and $a_{1/2}$. We observe that term which contributes the most is $\cos[(x' + y')/2] + \cos[(x' - y')/2]$ since $a_{1/2}$ has the highest values. a_0 is the signal of the emitter, and the highest signal takes place from around 200 to 750 nm in z, which coincides to the lateral position with the highest precision, which is portrayed in the values of σ_a and σ_b.

2.3 Axial localization of single emitters through calculation of Pearson coefficients

We now present how the axial localization is practically retrieved during the analysis of the images. Let's recall that a single emitter is localized in z by comparing the Fourier transform (FT) of its image with a look-up-table of Fourier transforms produced by acquiring a z-stack of images of another point-like emitter considered as calibration probe. A schematics of this process is presented in Fig.2.10.

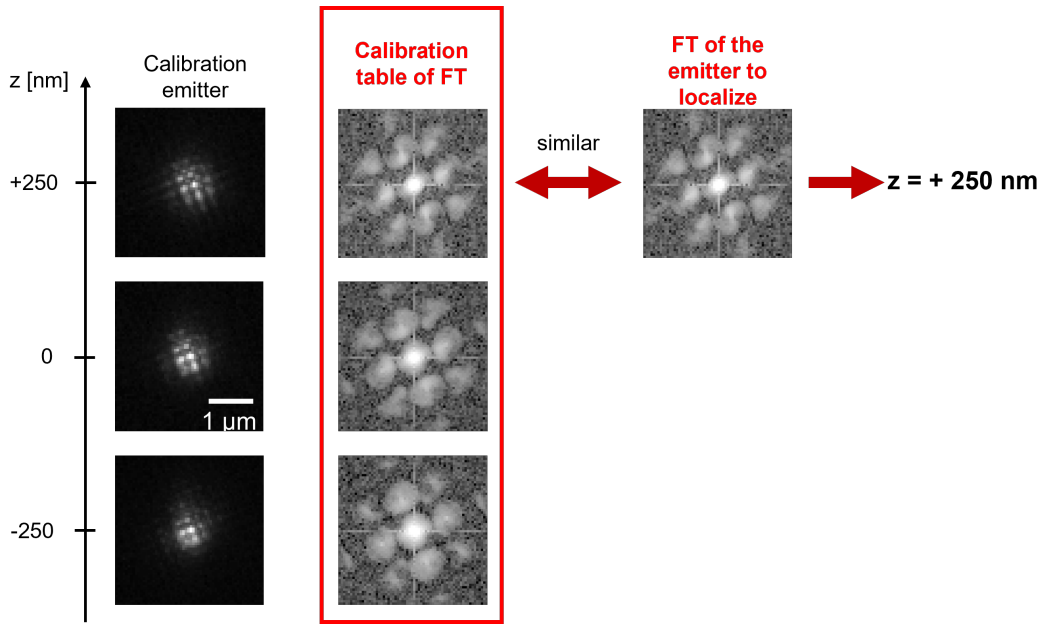

Figure 2.10: Schematics of the process of z localization by comparing the FT of a calibration emitter to the FT of the image of the emitter to localize.

We have chosen to perform the comparison between FTs by means of Pearson coefficient (r). The Pearson correlation coefficient is a measure of the linear correlation between two variables U and V, and is defined as

$$r = \frac{\mathrm{cov}(U,V)}{\sigma_U \sigma_V}, \tag{2.8}$$

where cov is the covariance of (U,V), and σ_U and σ_V are the standard deviations of U and V, respectively. These quantities are calculated as

$$\mathrm{cov}(U,V) = \frac{1}{N}\sum_i \left(U_i - \bar{U}\right)\left(V_i - \bar{V}\right) \quad \text{and} \quad (U,V).$$

Eq.2.8 reflects that r is basically a measurement of the covariance normalized by the standard deviations of U and V. Therefore, r always has a value between -1 and 1. In other words, the denominator of Eq.2.8 ensures that the scale of the data does not affect the correlation value, making the correlation much easier to interpret. Regarding the value interpretations, if the value is 0, there is no correlation between the two variables. A number larger than 0 denotes a positive connection whereas an association with a value less than 0 is said to be negative.

Before performing these calculations, we first calculate all the FTs. When computing Pearson coefficients in our data, U_i is squared magnitude of the FT ($|FT|^2$) of the i-th pixel of the FT image of the emitter to localize, V_i is the $|FT|^2$ of the i-th pixel in the FT image of the calibration emitter, and N is the total number of pixels in the FT image. The correlation coefficient r is calculated between the image in question and every image of the calibration z-stack. The highest r will then correspond to the z-localization of the emitter since it portrays a high similitude between both FTs. Since r is independent of data scale, then r is independent of the intensity amplitude of the signal, which is very practical given that experimentally we always deal with intensity fluctuations. Therefore, the comparison is not affected by the fact that the photon budget is not the same between the calibration emitter and the one to localize.

2.4 Machine learning as an alternative method for axial localization of single emitters

A method based on machine learning (ML) was also tested to determine the axial localization. A machine learning algorithm is a type of algorithm that learns as we expose it to data called training data. After the ML algorithm has been trained, it creates a model that fits the training data, and that is used to make predictions over other data sets, commonly called test data. A schematic of this process is shown in Fig.2.11.

Experimentally, we acquired images of immobile single TetraSpecks for different planes in z as the objective shifts of position. Therefore, we know the z position of the defocused TetraSpecks. The ML implementation starts with `Scikit learn`, which is a machine learning toolkit for Python. From this kit, we use `sklearn.ensemble.GradientBoostingRegressor()`, which is the model we have chosen based on its robustness observed in previous experiences using it. The training data is 10% of the optimized parameters obtained from the fitting model discussed in section 2.1, and that give us all the information regarding the SELFI PSF. The training data feeds the ML algorithm and creates a model that relates these parameters with the expected z positions. The remaning 90% is the test data, whose z positions will be predicted by means of the model created with the ML algorithm.

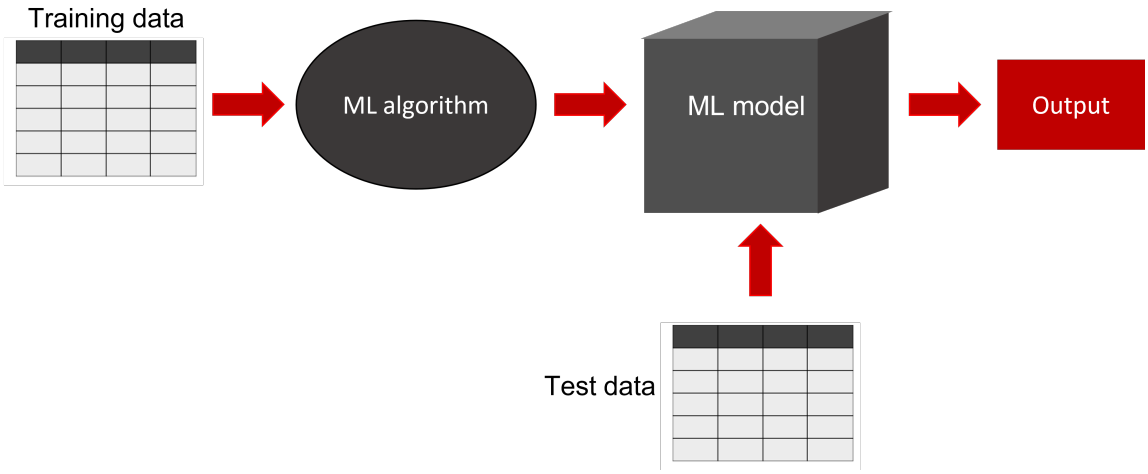

Figure 2.11: Schematic of machine learning algorithm.

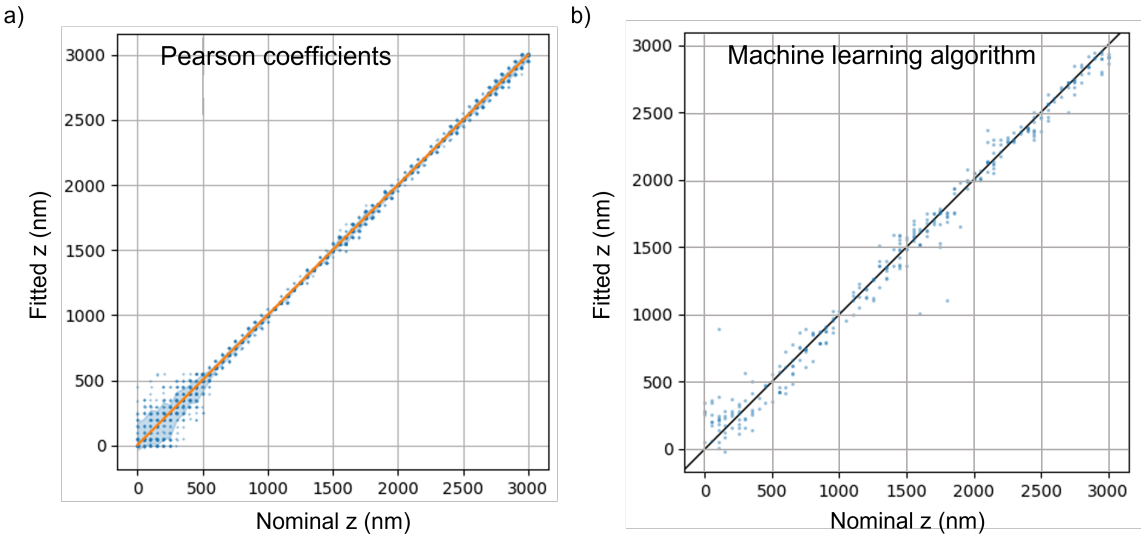

Figure 2.12: Comparison of z localization performance between a) Pearson coefficients and b) machine learning algorithm.

Fig.2.12 shows the z localization predicted for a set of images acquired experimentally. z has been determined by means of the two methods exposed in the present chapter: Pearson coefficients and ML. As we can observe, Pearson coefficients present a better precision in comparison to the ML method, reason why we chose Pearson coefficients for z localization and did not continue exploring in further detail the ML algorithm. However, this method should not be discarded as its performance may be improved by refining the code.

Chapter 3

Applications of near-infrared SELFI to carbon nanotubes

The goal of this thesis has been to design and build a self-interference super-resolution optical setup to image single-walled carbon nanotubes (SWCNTs) and determine their 3D position for single-particle tracking (SPT) applications in live brain tissues. After having presented SELFI and its applications on spherical nanoparticles in chapter 1, we now show how SELFI can be applied on SWCNTs in brain tissue. To do so, we have two things to consider: first, SWCNTs differ from nanoparticles used in chapter 1 due to their dimensions, and second, SWCNTs are more photostable and present bright photoluminiscence. Our discussions start by introducing SWCNTs, and their important features in terms of structure and photophysical properties. Then we show 3D localization of immobilized nanotubes. After, we exhibit single-particle tracking of carbon nanotubes in different types of media, such as homogeneous medium (glycerol-water mixture), heterogeneous medium (agarose gel), and finally live brain slices.

3.1 A brief overview of single-walled carbon nanotubes and their properties

Carbon is a nonmetallic chemical element with atomic number 6, that means it has six electrons occupying $1s^2$, $2s^2$, and $2p^2$ atomic orbitals. Carbon is tetravalent, denoting that four of its electrons are available to make covalent chemical bonds. This fact enables carbon to form different allotropes depending on their hybridization, such as graphite (sp^2) and diamond (sp^3), and some other nanostructures like graphene, fullerene, and carbon nanotubes (sp^2). Among all the allotropes, carbon nanotubes have been the focus of many studies in research for a vast field of applications due to their exceptional properties.

Carbon nanotubes are rolled-up sheets of graphene which is a lattice of sp^2 hy-

bridized carbon atoms, forming hollow cylindrical nanostructures with high length-to-diameter ratio. Their diameter can go from 0.4 to 10 nm, while their length can go from hundreds of nm to μm. The discovery of carbon nanotubes traces back to 1993 by Iijima *et al.* [71], and Bethune *et al.* [72], independently; and they have been widely studied ever since. Single-walled carbon nanotubes (SWCNTs), the kind of nanotubes subject of this research, were named after their structure conformed by a single layer of graphene. In 2002, it was discovered that SWCNTs are fluorescent in the NIR range ($\sim$ 870 - 2500 nm) [73, 74], matching the tissue transparency window, i.e. the range of wavelengths where light has its maximum penetration in biological tissue [75]. This was a starting point to consider carbon nanotubes in applications for bioimaging.

3.1.1 Synthesis of SWCNTs

Synthesis of carbon nanotubes is a topic in research with increasing interest since there are some challenges still remaining to overcome, such as low-cost production in large scale of high-quality nanotubes, structure-controlled production of nanotubes, location and orientation organization of nanotubes on a substrate surface, and unraveling the processes involved in nanotubes [76]. There are mainly two methods used for nanotube synthesis, being them plasma-based synthesis methods including arc discharge technique and laser ablation technique; and thermal synthesis process including chemical vapor deposition (CVD) and plasma-enhanced CVD (PECVD). Among them, the most commonly used, due to their simplicity, low cost, low temperature, and ambient pressure, are CVD-based [76, 77], such as HiPco (high pressure carbon monoxide) and CoMoCAT (unique catalyst mixture of cobalt and molybdenum).

As HiPco and CoMoCAT nanotubes are used for experimentation during this thesis, we discuss their synthesis processes in the following sections.

3.1.1.1 HiPco SWCNTs

HipCo nanotubes are produced by heating and applying high pressure to carbon monoxide (CO) gas in a chamber. Generally, the temperature ranges between 800°C and 1200°C at pressures between 1 [78] and 100 atm [79]. Iron pentacarbonyl ($Fe(CO)_5$) is used as a catalyst during this process, which decomposes forming iron vapour that forms aggregates. The growth of the nanotubes is supported by these aggregates. Temperature and pressure have an impact on the nanotubes' distribution of diameters. For instance, at 1200 °C and 10 atm of pressure, the nanotubes' diameters generally range between 0.6 nm and 1.3 nm. Eventually, the iron is removed from the nanotubes to end up with a more purified sample [80].

3.1.1.2 CoMoCAT SWCNTs

D. E. Resasco et al. invented the synthesis of CoMoCAT nanotubes [81]. CO is synthesized under a pressure of 1 to 10 atm with a temperature range of 700 to 950°C. Cobalt (Co) and Molybdenum (Mo) are utilized as catalysts in this process. Mo oxide substrate and a layer of cobalt molybdate ($CoMoO_4$) are progressively deposited in one side of the bottom of the chamber. On the other side of the chamber, there is a deposition of non-metallic cobalt. Cobalt's crystalline structure will alter as a result of the reaction. Under CO atmosphere, Mo oxide becomes Mo carbide. This process causes $CoMoO_4$ to disintegrate, allowing carbon monoxide to reduce cobalt. Cobalt becomes metallic. In the same way as for HipCo, the metallic cobalt agglomerates and nanotubes grow on the cobalt aggregates thanks to the CO decomposition reaction.

The production of different nanotubes can be favored by changing the ratios of Co and Mo. For instance, if Co is greater than Mo, then the synthesis will favor multiwall nanotubes. After the synthesis step, the nanotubes are detached from the support. For this, the sample is first immersed in a basic bath to remove the catalysts. It is then oxidized in air at 200 - 250°C and finally immersed in a bath of nitric or hydrochloric acid.

The distribution of nanotube diameters changes depending on the production method. Compared to CoMoCAT, HipCo has a greater spread [81] since the latter favors the synthesis of small diameter nanotubes.

3.1.2 Geometrical structure of SWCNTs

In the real space, the structure of SWCNTs is categorized by a couple of integer chiral indices (n, m), coming from the chiral vector of the graphene lattice $\vec{R} = n\vec{R}_1 + m\vec{R}_2$, where $\vec{R}_1$ and $\vec{R}_2$ are lattice unit vectors of the graphene sheet [82], see Fig.3.1. What is more, $\vec{R}$ forms the circumference of carbon nanotubes. From (n, m) it is possible to calculate the diameter (d_t) and chiral angle (θ) of the nanotubes:

$$d_t = \frac{|\vec{R}|}{\pi} = \frac{a_{CC}}{\pi}\sqrt{3\left(m^2 + n^2 + mn\right)} \quad \text{and} \quad \theta = \tan^{-1}\frac{\sqrt{3}m}{2n+m}, \tag{3.1}$$

where $a_{CC} = 1.44$ Å is the carbon-carbon bond distance of graphene [82, 83]. (n, m) are also correlated with the nanotube *helicity*. It is called "armchair" when $n = m$, and "zigzag" when $m = 0$, "right-handed" if $n - m > 0$, and "left-handed" otherwise [82,83]. The indices (n, m) are correlated with the electric properties of SWCNTs [84]. For instance, when $|m–n| = 3k$ for any integer k, SWCNTs are metallic; whereas when $|m–n| = 3k \pm 1$, SWCNTs are semiconductors.

From Eq.3.1, we observe that SWCNTs' diameter increases as (n, m) increase as well. d_t varies typically between 0.32 nm for (4, 0) nanotubes and 1.35 nm for (10, 10) nanotubes. In this thesis, we have used (6, 5) nanotubes with a diameter of 0.76 nm.

SWCNTs are considered to be one-dimensional nanostructures as their length is much larger than their diameter. In fact, their length can reach several micrometers [85]. Therefore, SWCNTs are 1D objects with a very strong confinement in two dimensions, influencing their electronic and optical properties.

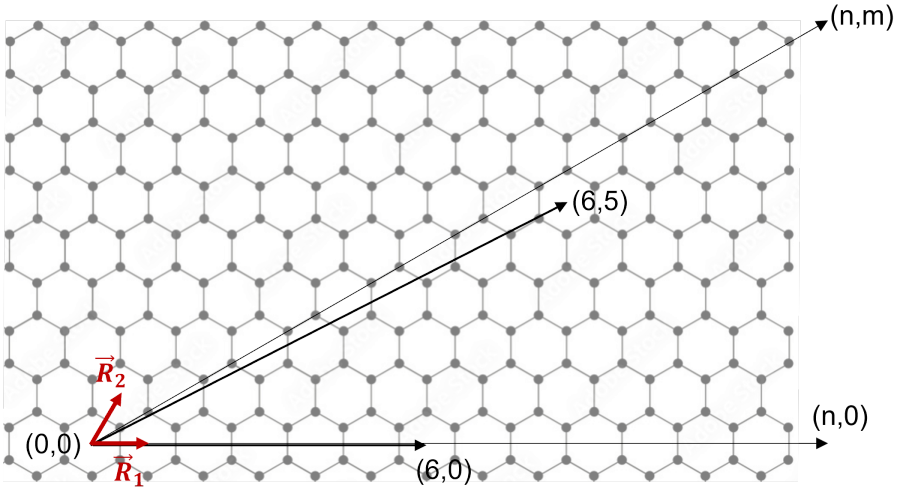

Figure 3.1: Scheme of the crystallography of a right-handed (8,4) and a left-handed (4,8) SWCNT. (Figure obtained from Yang F. *et al. Chem. Rev.* 2020 [82])

In the reciprocal space, i.e. the space conformed by spatial frequencies and defined by the wavelength vector $\vec{k}$, the geometry of the crystal lattice is directly correlated to the geometry in the real space. It is important to describe the geometry of SWCNTs in the reciprocal space as their electric and optical properties depend on it in this context. We may start from the reciprocal space of graphene given that carbon nanotubes have a local crystal structure that is identical to that of graphene in the real space. Since the real-space crystal structure of graphene is hexagonal, so is its reciprocal lattice, as shown in Fig.3.2.a. The point Γ is the rotation's center with symmetry $\pi/3$. Points K and K' play a crucial role when describing the electric properties of SWCNTs, as it will be discussed in the following section.

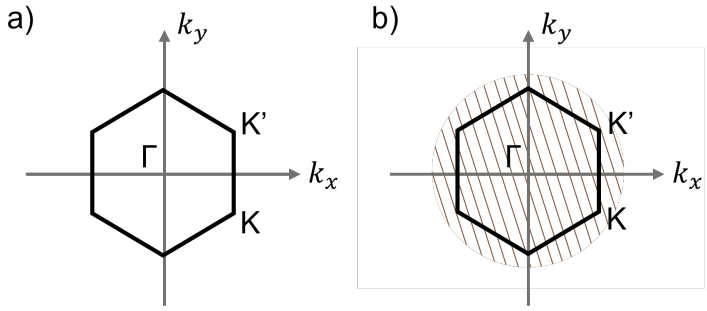

Figure 3.2: a) Graphene lattice in the reciprocal space. b) Brillouin zone of graphene. Parallel lines represent allowed energy states for SWNTs.

3.1.3 Electric properties of SWCNTs

SWCNTs are quantum systems, therefore, by solving their Schrödinger's equation, we may have access to their energy states, which determine SWCNTs' electrical characteristics. In the present section, we start by stating the Hamiltonian of graphene, leagind us to the energy states. After, we explain how this result is linked to SWCNTs' energy landscape.

Graphene's unit cell has two carbon atoms forming a π bond. Each atom contributes with one electron in this bond. The Hamiltonian of these carbon atoms is given by:

$$\hat{H} = \hat{T}_N + \hat{T}_e + \hat{V}_{Ne} + \hat{V}_{ee} + \hat{V}_{NN},$$

where $\hat{T}_N$ is the kinetic energy of the nuclei, $\hat{T}_e$ is the kinetic energy of the electrons, $\hat{V}_{Ne}$ is the interaction potential between nuclei and electrons, $\hat{V}_{ee}$ is the interaction potential between electrons, and $\hat{V}_{NN}$ is the interaction potential between nuclei.

Given that the mass of the carbon nuclei is 2000 times bigger than the one od the electrons, the movements of the nuclei are negligible compared to those of the electrons, considering them as immobile (Born-Oppenheimer approximation). This means that $\hat{T}_N = 0$, and $\hat{V}_{NN}$ is a constant. Therefore, the Hamiltonian becomes

$$\hat{H} = \hat{T}_e + \hat{V}_{Ne} + \hat{V}_{ee} + \hat{V}_{NN}.$$

The eigenenergies (E) of $\hat{H}$ are the values that satisfy the equation

$$\hat{H}|\psi\rangle = E|\psi\rangle, \tag{3.2}$$

where $|\psi\rangle$ is the wavefunction of the system. By solving Eq.3.2, we obtain the energy dispersion relation:

$$E = \pm\, \tau_0 \sqrt{1 + 4\cos\frac{3k_x a_{CC}}{2}\cos\frac{\sqrt{3}k_y a_{CC}}{2} + 4\cos^2\frac{\sqrt{3}k_y a_{CC}}{2}}, \tag{3.3}$$

where τ_0 is the transfer integral between first-neighbor π orbitals, $\vec{k} = (k_x, k_y)$ is the wavevector that belongs to the first hexagonal Brillouin zone, and the sign $\pm$ represents the energies of the conduction band and the valence band [86]. Graphene's energy bands are shown in Fig.3.3. Points K and K' are points of electronic singularities where the conduction band and the valence band meet, giving graphene its conduction properties.

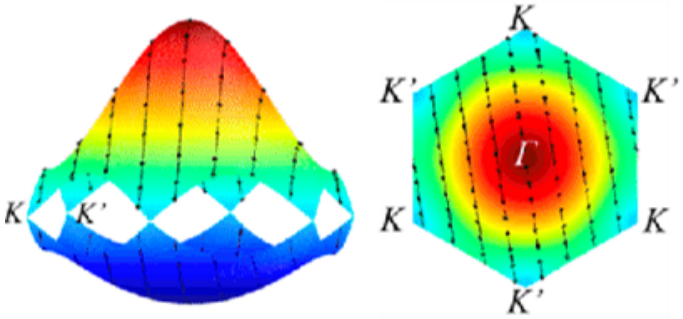

Figure 3.3: Energy dispersion plot for conduction and valence bands of graphene's first Brillouin zone. Right, side view; left, vertical view. (Figure obtained from Yang F. et al. Chem. Rev. 2020 [82])

SWCNTs' electronic bands correspond to the electronic bands of the graphene cut along the parallel wave vectors (dotted black lines in Fig.3.3). If one of these lines passes through the points K or K', then the nanotube is metallic, otherwise it is semiconductor.

3.1.4 Optical transitions of SWCNTs

The density of electronic states (DOS) determines the permitted optical transitions of nanotubes. For simplicity, we initially ignore the confinement effects and focus on the one-electron model to describe the DOS. After, we shall explore the consequences of this limited model, which force the examination of excitonic processes.

3.1.4.1 One-electron model

As SWCNTs are composed of a single rolled up graphene sheet, the simplest way to describe their electronic structure is by considering the same of the graphene sheet with periodic boundary conditions imposed over the rollup vector $\vec{R}$ [87]. Therefore, the universal DOS described in these pages is based on the graphene sheet model.

In general terms, the contribution of a single, doubly degenerate 1D band $\varepsilon(k)$ to the density of states, $n(E)$, is expressed as

$$n(E) = \frac{2}{l} \sum_i \int dk\, \delta(k - k_i) \left| \frac{\partial \varepsilon}{\partial k} \right|^{-1}, \tag{3.4}$$

where k_i are the solutions to the equation $E - \varepsilon_i = 0$, and l represents the length of the 1D Brillouin zone and is given by $l = 4\pi|\vec{R}|/(\sqrt{3}a^2)$ in the case of SWCNTs.

The density of electronic states can be defined for any energy value. However, since it has been demonstrated that the DOS around the Fermi level (close to the K and K' points) are alike for semiconducting SWNTs with similar diameters, and it

has been established the same relationship for metallic nanotubes, then a universal DOS around the Fermi level can be written for SWCNTs with diameters from 1.3 to 2.8 nm [88]. In other words, the DOS described in this section only depends on whether the SWCNT belongs to the semiconducting or metallic groups of nanotubes.

Near the Fermi level, the DOS is correlated to the energy states closest to k_F. In this region, the 2D dispersion relations of the π bands of graphene can be described by a linear approximation which has been demonstrated to work well by [89], and is stated as follows:

$$|\varepsilon(\vec{k})| \approx \frac{3}{2}\, a_{CC}\, \gamma_0\, |\vec{k} - \vec{k}_F|, \tag{3.5}$$

where γ_0 is the nearest neighbor carbon-carbon interaction energy.

$|\varepsilon(\vec{k})|$ can also be written in terms of the chiral numbers (n, m), and the condition that allowed electron states for SWCNTs are restricted to points where the wavevector satisfies $\vec{k} \cdot \vec{R} = 2\pi\mu$, μ being an integer:

$$|\varepsilon_\mu| = |3\mu - n + m|\, \gamma_0\, \frac{a_{CC}}{d_t}. \tag{3.6}$$

We observe from Eq.3.5 that, when $k \to k_F$, $|\varepsilon(\vec{k})| \to 0$, resulting in a divergence in the occupied (unoccupied) DOS near ε_F called van Hove singularity [88].

Reference [87] exposes the theoretical procedure of how from Eqs.3.4 and 3.5 one can obtain the DOS, $\rho(E)$, in the vicinity of the Fermi level ε_F of all carbon nanotubes:

$$\rho(E) = \frac{1}{\Lambda\gamma_0}\, U\left(\frac{\Lambda E}{\gamma_0}\right), \tag{3.7}$$

where

$$U(E') = \frac{2\sqrt{3}}{\pi^2} \sum_{\mu'=-\infty}^{\infty} g(E', \varepsilon'_{\mu'}),$$

and

$$g(E', \varepsilon'_{\mu'}) = \begin{cases} |E'|/\sqrt{E'^2 - \varepsilon'^2_{\mu'}}, & \text{if } |E'| > |\varepsilon'_{\mu'}| \\ 0, & \text{if } |E'| < |\varepsilon'_{\mu'}| \end{cases}.$$

Fig.3.4 shows the energy

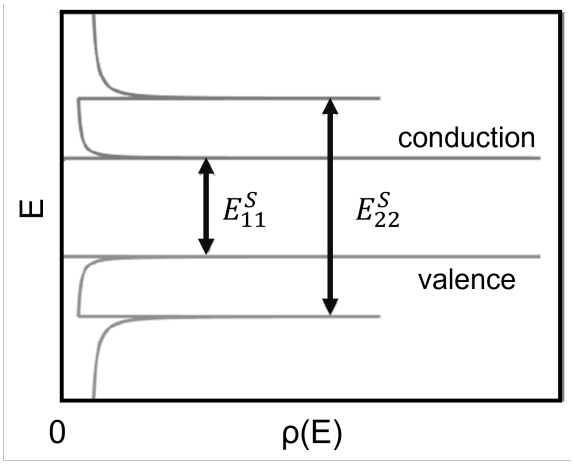

Figure 3.4: Density of states and van Hove singularities for a semiconducting SWCNT, such as $(6, 5)$ SWCNTs.

From Eq.3.6, we can determine the energy differences between the ith van Hove singularity peaks in the conduction and valence bands numbered from the Fermi energy, $E_{ii}^{M,S}(d_t)$, as a function of nanotube diameter d_t, M stands for metallic SWCNTs, and S for semiconducting SWCNTs. $E_{11}^S(d_t)$ denotes the energy difference between the highest-lying valence-band singularity and the lowest-lying conduction-band singularity in the 1D DOS for for a semiconducting SWCNT, as shown in Fig.3.4, likewise $E_{22}^S(d_t)$. Reference [90] determines expressions for $E_{11}^M(d_t)$ as well as $E_{11}^S(d_t)$:

$$E_{11}^M(d_t) = \frac{6a_0\gamma_0}{d_t}$$
$$E_{11}^S(d_t) = \frac{2a_0\gamma_0}{d_t}.$$

However, the one-electron model previously described, does not take into account the confinement effects due to the small diameter of the nanotube which makes this model incomplete to quantitatively describe the experiments [73, 91]. Besides, to describe in more detail the optical transitions involved in carbon nanotubes, it is necessary to introduce excitonic processes [92–95].

3.1.4.2 Excitonic model

Because of the high confinement caused by the nanotubes' diameter, excitons arise as a result of light's stimulation. With absorption of a photon, an electron in the valence band is is excited and moves into the conduction band. This electron leaves behind a hole in the valence band. Then, the exciton is produced as a consequence of the Coulomb interaction between the electron (e^-) and the hole (e^+) in the confined nanotube space. Exciton formation is accompanied by an inter-fermionic E_b binding energy that can reach several hundred meV, a significant fraction of the E_{11}^S

transition [96]. This binding energy depends, among other things, on the immediate environment of the nanotube [97].

Excitonic states

As mentioned above, excitons take place in SWCNTs when they interact with light. Therefore, it is necessary to understand the energy states of excitons to explain the optical transitions in SWCNTs. The Schrödinger equation for the exciton's eigenenergy solutions represent the excitonic states. We may explain the phenomenology of the optically permitted transitions of SWCNTs without having to solve this equation by relying on the symmetry components of the excitonic wave function. The exciton's wave function ($\Phi\left(\vec{r}_e, \vec{r}_h\right)$) is conformed by a linear combination of products between the conduction electron and valence hole wave functions, $\varphi_c(\vec{r}_e)$, and $\varphi_v^*(\vec{r}_h)$, respectively. For small diameters (d $<$ 1.5 nm), the gaps between the Van Hove singularities are relatively large. In fact, the minimum gap is equal to $2a_0\gamma_0/d_t$, therefore the wider the gap, the smaller the diameter of the nanotube. This criterion allows us to compute the exciton's wave function while just taking the first Van Hove singularity into account. The exciton's wave function is then written as:

$$\Phi\left(\vec{r}_e, \vec{r}_h\right) = \sum_{c,v} A_{c,v}\ \varphi_c(\vec{r}_e)\ \varphi_v^*(\vec{r}_h),$$

where v and c stand for valence- and conduction-band states, respectively [98]. The coefficient $A_{c,v}$ describes the coupling between electrons and holes.

When considering nanotubes with small diameters (d_t $<$ 1.5 nm), the energy separation between singularities in the exciton's density of states is large. Therefore, it is reasonable to assume, as a first approximation, that the excitonic states are only formed by the electronic bands contributing to a given 1D singularity [98, 99]. This allows us to employ the effective-mass and envelope-function approximations (EMA) [98, 100]:

$$\Phi^{EMA}\left(\vec{r}_e, \vec{r}_h\right) = \sum_{c,v} B_{c,v}\ \varphi_c(\vec{r}_e)\ \varphi_v^*(\vec{r}_h) F_\nu(z_e - z_h),$$

where the sum is made only over those states associated with the exciton's density of states singularity. $F_\nu(z_e - z_h)$ is the envelope function that provides an appropriate localization of the exciton in the relative coordinate $z_e - z_h$, and ν corresponds to the level of the Rydberg series for hydrogen atoms. The deformation potential (phonons) resulting from the interaction between the exciton and the lattice atoms is taken into account by the envelope function. The envelope function is even when ν is also even. Therefore, three terms dependent on the spatial geometry ($\vec{r}$ and z) conform the exciton's wave function.

The transitions that are permitted optically depend on the symmetry (parity) of this wave function. The Schrödinger equation may be solved to provide four excitonic states with various symmetries. We have four potential spin states thanks to the electron and hole spins: one singlet and three triplets. Thus, there are 16 total excitonic states for each van Hove singularity. To a first approximation, the optical transitions are unaffected by the triplet levels, which have a higher energy than the singlet states. Indeed, second order adjustments to the energy levels are brought about by spin effects. Fig.3.5 displays the first van Hove Singularity's four lowest energy singlet excitonic states. In the following part, we explain the notations used in Fig.3.5.

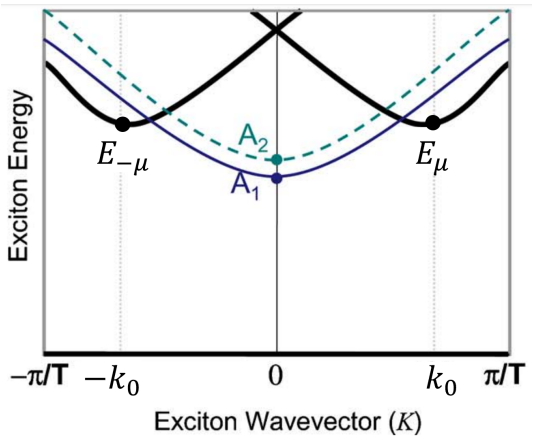

Figure 3.5: Schematic representation of the 4 lowest energy singlet exciton levels for the first Van Hove Singularity. The dotted line corresponds to the bright state (figure extracted from Barros, Physical Review B. 2006 [98]).

Permitted optical transitions

Electrical dipolar interactions must respect selection rules. The dipolar transition for the exciton is only possible if the parities of the wave function under a C_2 rotation (a π rotation perpendicular to the tube axis, bringing z to $-z$) before and after the excitation are in opposition. The singlet excitonic state A_2 is equivalent to this circumstance. Thus, the immediate formation of an exciton from the absorption of an energy photon "A_2" is possible (see Fig.3.5). The exciton is referred to be "brigh" as this excitonic condition that is optically permissible. The A_1 excitonic state's wave function is peculiar. As a result, this transition is not permitted visually. Be aware that this energy level, which is only a few meV below the A_2 level, has a role in the temporal dynamics of the exciton's de-excitation [101]. Additionally, Fig.3.5 shows that an optical transition facilitated by phonons can result in the formation of "black" excitons with energy E_μ (also known as "K-momentum dark excitons") or in the relaxation of the exciton between the E_μ and A_2 energy levels [102].

Properties of absorption

Fig.3.6 shows the absorption spectrum of (6,5) SWCNTs. We observe there are three primary absorption peaks on the absorption spectra of this semiconducting carbon nanotubes with a given chirality. On this spectrum, we notice two peaks that correspond to absorptions on the E_{22}^S and E_{11}^S transitions as well as the peak that corresponds to an absorption towards the K-momentum dark exciton assisted by phonons, called KSB transition (K-momentum excitonphon sideband).

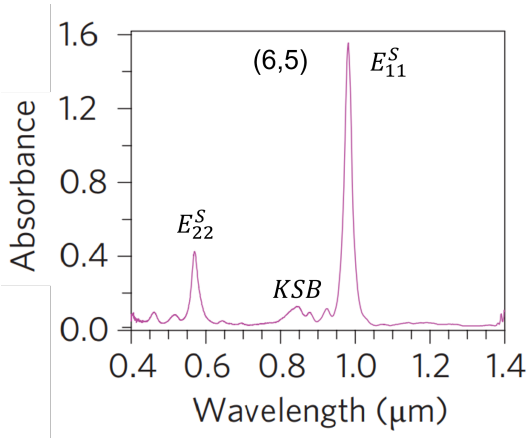

Figure 3.6: Absorption of (6, 5) nanotubes as a function of the excitation wavelength showing the optically allowed transitions. (Figure extracted from Weisman, Nature Nanotechnology. 2010 [103])

3.1.5 Photoluminiscence of SWCNTs

SWCNTs are among the brightest and most photostable nanostructures in the NIR range of emission due to their fast decay rates and high absorption cross-sections. These features allow SWCNTs to be excellent probes for single-molecule imaging. Nevertheless, it has been shown that photoluminescence quantum yields (PLQY) of pristine SWCNTs is relatively low ($< 1\%$) compared to others nanoparticles emitting in other wavelengths [104]. SWCNTs' PLQY low performance is caused by two different reasons. First, a low-lying "dark" state present $\sim$ 5 - 100 meV below the allowed E_{11} energy transition precipitates energy loss through thermal processes [105]. Second, nonradiative decays of the exciton take place, such as multiphonon decay and phonon-assisted indirect exciton ionization mechanism [101, 106]. Furthermore, external factors also play an important role in the performance of PLQY of SWCNTs since PL is highly sensitive to local chemical defects of the nanotube structure as well as to chemical or dielectric environments [54, 107], causing local quenching of the PL. Therefore, the signal quality is different for each SWCNT as it is correlated with the imperfections existent in their structures. Nevertheless, the sensitivity of SWCNTs

PL to local chemical defects can be used to improve the PL performance, as it will be discussed in the following subsection.

3.1.6 Encapsulation of SWCNTs

Single-walled carbon nanotubes are hydrophobic nanostructures, and have strong Van der Walls interactions between each other, creating bundles of nanotubes. In order to separate them and be able to suspend them in an aqueous media, water in this PhD thesis, amphiphilic coatings are used. Amphiphilic molecules have both hydrophobic (nonpolar) and hydrophilic (polar) regions. The hydrophobic part bonds to the nanotube, while the hydrophilic one is exposed to the ouside medium, making possible for SWCNTs to disolve in water. Different kinds of coatings can be used, such as protein based coatings including DNA [108, 109] and bovine serum albumin (BSA) [110], surfactants [111] namely sodium dodecyl benzene sulphonate (SDBS), sodium dodecyl sulfate (SDS), cetyltrimethylammonium bromide and sodium deoxycholate (DOC) [112, 113], and lipids like phospholipid-polyethylene glycol (PL–PEG) [114].

In the present work, we have used surfactants and lipids-based coatings on SWCNTs, each used for different applications:

- DOC works well when encapsulating SWCNTs, allowing the preparation of highly bright suspensions. In fact, SWCNTs wrapped with DOC are the brightest ones. However, as DOC is a detergent, it has a high probability to create toxicity if used for biological applications, reason why DOC-coated SWCNTs have been only used on experiments involving glycerol or agarose media.

- PL-PEG is used in order to perform experiments related to biological applications, such as diffusion observations in brain slices. The hydrophobic PL chains attach to the nanotube's surface, while the PEG increases the solubility and stability of nanotubes in high salt and serum containing environments [115]. In this work, the DSPE-mPEG$_{5k}$ (1,2-Distearoyl-sn-Glycero-3-Phosphoethanolamine with conjugated methoxyl poly(ethylene glycol)) is the coating chosen. The DSPE part has a good interaction with the nanotube, while the PEG part allows the preparation of a suspension in water.

3.1.7 Suspension process of SWCNTs

3.1.7.1 DOC wrapping of HiPco SWCNTs

HiPco nanotubes (1 mg) are suspended in 1.0% w/v DOC in 10 mL Milli-Q water. Milli-Q water is water purified using a Millipore Milli-Q lab water system. Ultra Turrax at 19000RPM is used for 15 min for homogenization purpose of the mixture

coating + nanotubes in water. SWCNTs were further dispersed by tip sonication at the output power of 1 W/mL for 30 min. Nanotube bundles and impurities were precipitated by centrifugation at 18,000 RPM for 60 min at room temperature. 70–80% of the supernatant of DOC functionalized SWCNTs was then collected.

3.1.7.2 PL-PEG wrapping of CoMoCAT SWCNTs

CoMoCAT nanotubes (1 mg) are suspended in 0.5% w/v PL-PEG in Milli-Q water (10 mL). Ultra Turrax at 19000RPM is used for 15 min for homogenization purpose of the mixture coating + nanotubes in water. SWCNTs were further dispersed by tip sonication at the output power of 1 W/mL for 30 min. Nanotube bundles and impurities were precipitated by centrifugation at 18,000 RPM for 60 min at room temperature. 70–80% of the supernatant of PL-PEG functionalized SWCNTs was then collected and stored at 4°C.

3.1.8 Single-molecule localization microscopy of SWCNTs

To perform experiments involving single-molecule localization microscopy of SWCNTs, such as 2D single-particle tracking of CNTs, the optical setup used is the one showed in Fig.3.7.a. As observed, it is a simple setup that consists in a high-NA objective, a laser power to excite the nanotubes, such as an 845 nm laser, and a camera suitable for SWCNTs' NIR emission, such as InGaAs cameras. Fig.3.7.b shows an image of fixed SWCNTs observed with these type of setup.

A technique that uses single-emitter localization to address important challenges in biology and materials science is single-particle tracking. In an SPT experiment, a particular molecule's spatial route is established by repeatedly detecting and super-localizing it at several successive frames acquired [37, 116]. The type of motion followed by the tracked particles, which may be diffusive, motor-directed, restricted, or a combination of these modes, can be determined by analysis of the mean square displacement (MSD) calculated from the single-molecule tracks [117–122]. The fluorescent probe utilized is often dilute enough to attain single-molecule concentration for applications in materials science and in vitro reconstitutions of biological systems. In order to minimize the emitter concentration for fluorescently tagged proteins in live cells, extra techniques are occasionally required. Reduced expression of genetically encoded labels [123], quenching or photobleaching of an originally high number of emitters, chemical emitter production, or sparse activation of just a small number of photoactivatable molecules at once are a few examples of these techniques [124, 125]. The motion of the target molecule as it performs its function in the natural biological environment, such as the cytoplasm or the membrane, is more representative, even though in vitro measurements are easier to perform because intracellular crowding

and binding interactions with cellular structures influence measured trajectories [126]. In the Introduction chapter of this thesis, we have discussed some results on 2D SPT of SWCNTs obtained by our research team.

In the following section, we present a brief explanation on how to analyze the translational diffusion of SWCNTs when they follow a stochastic movement.

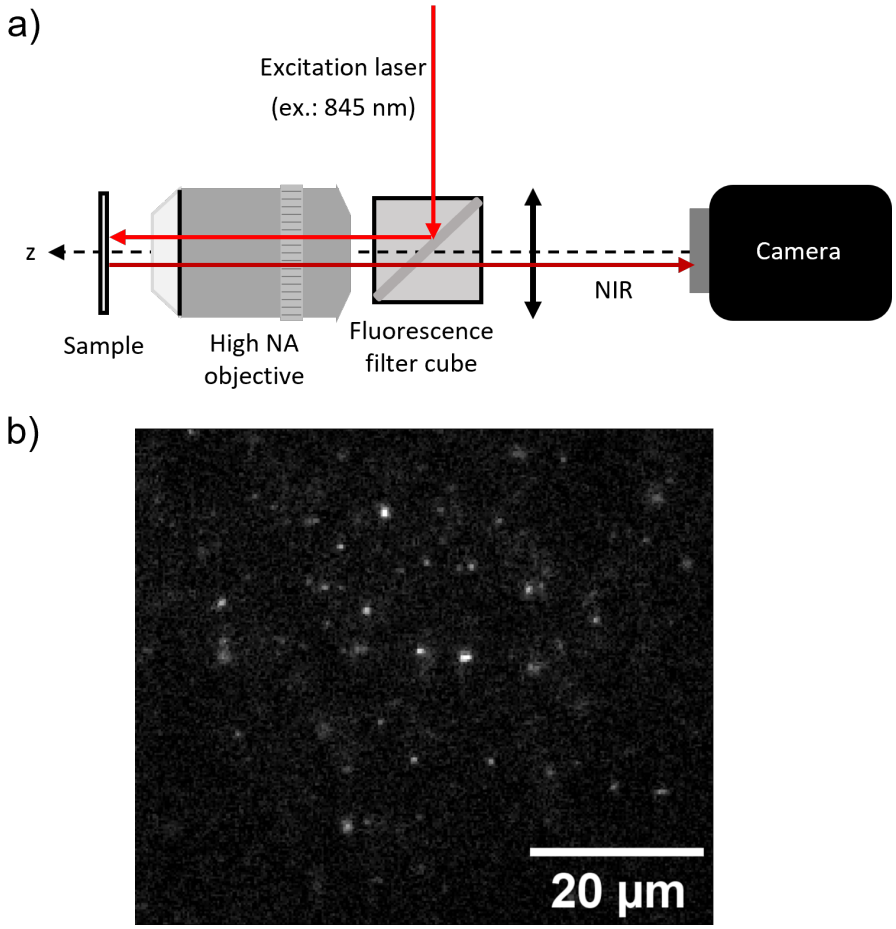

Figure 3.7: Optical setup to perform single-molecule localization microscopy of SWCNTs.

3.1.8.1 Translational diffusion of SWCNTs

Let's consider a SWCNT diffusing in a viscous media, and drawing a finite trajectory. The two-dimensional mean-square displacement, which describes the nanotube's isotropic mobility during a time interval t, is

$$MSD_T(t) = \frac{1}{T-t}\sum_{i=1}^{T-t}\left(\vec{r}_{i+t} - \vec{r}_i\right)^2, \tag{3.8}$$

where T is the number of frames in the movie stack and $\vec{r}$ the 2D projection of the position vector of the SWCNT. The MSD depends linearly on the time lag t as follows:

$$MSD_T(t) = 4D_T t,$$

where D_T is the translational diffusion coefficient. Nevertheless, experimentally we must consider the contribution of localization error σ and motion blur over the exposure time t_E. Then, the empirical MSD is [127]

$$MSD_T(t) = 4D_T t + 4\sigma^2 - \frac{4}{3} D_T t_E.$$

In the case of nanotubes shorter than 3 μm, their diffusion behavior can be approximated to the one of a rigid rod [128], in which case the translational diffusion coefficient is given by

$$D_T = \frac{k_B T}{3\pi\eta L} \left[\log p + X_T(p)\right],$$

where k_B is the Boltzmann constant, T the temperature, η the viscosity of the medium, L the length of the SWCNT, $p = L/d$ its hydrodynamic aspect ratio (its length L to its hydrodynamic diameter d), and $XT(p)$ is the following finite-length correction term [127]:

$$X_T(p) \approx 0.38 - \frac{1.16}{\sqrt{p}} + \frac{1.77}{p} - \frac{0.14}{p^2} + \frac{0.55 \log p}{p} - \frac{0.1 \log p}{p^2}.$$

3.2 Three-dimensional localization of immobilized carbon nanotubes

In the present section, we demonstrate the application of SELFI to SWCNTs imaging and analyze the performance of the method on these atypical probes. Here, we localize different immobilized SWCNTs, and observe how the precision and accuracy along z changes as a function of the number of photons emitted.

3.2.1 Sample preparation

Samples were prepared in the following way: first, HipCo DOC SWCNTs suspension is diluted in water to a concentration of 33:1000. Then, this solution is sonicated for 15 mins to homogenize it. After, the solution is spincoated on a coverslip for 2 mins with a velocity of 920 RPM for immobilization of SWCNTs, as shown in Fig.3.8. Alternatively to the spincoating process for fixation of SWCNTs to the coverslip surface, dropcast has also been used, which consists in putting a few μL of the solution on the coverslip and let it dry. However, when using the dropcast method, there is a decrease on SWCNTs brightness, leading to a lesser number of photons detected by the camera.

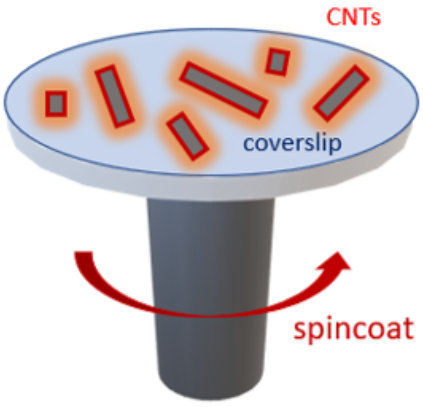

Figure 3.8: Sample preparation of fixed SWCNTs.

3.2.2 Imaging and analysis protocol

The optical setup used is shown in Fig.3.9. The objective used is the Nikon Plan Apochromat, 60×, $NA = 1.27$, water immersion, IR. The excitation laser is the 3900S CW Tunable Ti Sapphire laser from Spectra-Physics at 845 nm. As filters, we have used a longpass 900 nm dichroic mirror (DMLP900R)s, and a longpass 900 nm emission filter (ET900LP). A sCMOS KURO camera was used for detection.

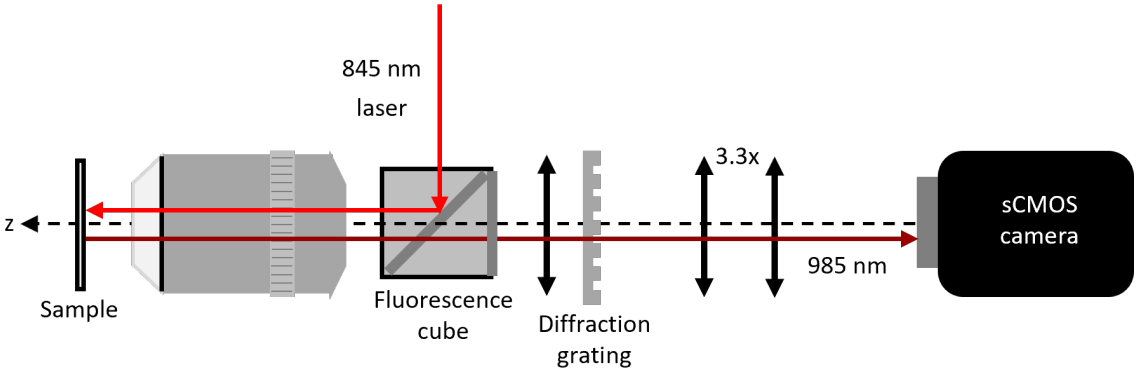

Figure 3.9: SELFI optical setup for 3D super-localization of SWCNTs.

The imaging process is the following: multiple fixed nanotubes were imaged in the center of the camera field of view. For each nanotube, a z-stack is acquired from -750 nm to +750 nm around the best focus in steps of 50 nm by controlling the focus of the objective. For each position in z, 30 images are taken by using an exposure time of 150 ms. Then, the analysis code is run to localize every nanotube.

3.2.3 SELFI calibration with fixed SWCNTs

Fig.3.10 shows images of a HipCo DOC nanotube for different z positions observed with the setup shown in Fig.3.9. It is important to remark the outstanding photo-

luminiscence of HipCo DOC SWCNTs (18000 photons in this case) as their signal is bright and stable, making it possible to have a very clear self-interference pattern. As a consequence, the background is weak compared to the nanotube signal.

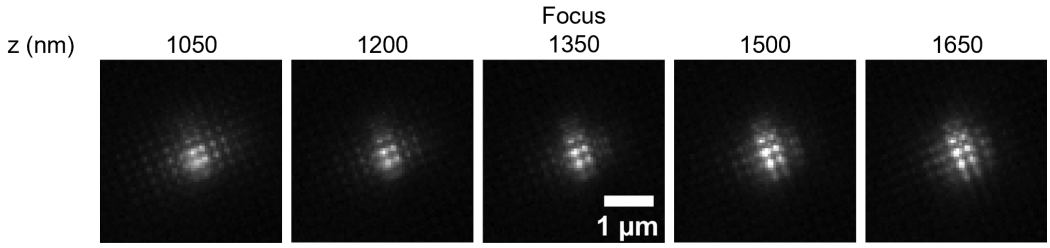

Figure 3.10: Images of a SWCNT for different focal planes obtained with SELFI optical setup. The focal plane is located at the z position 1350 nm. Photon budget: 18000.

The SWCNT shown in Fig.3.10 ($\sim$ 18000 photons), was localized, and its z-localization, precision, and accuracy are displayed in Fig.3.11. Let's recall that nominal z is the locations (z) given by the microscope, and fitted z is the z-localization resulting from our analysis. As can be seen in Fig.3.11, the precision in (x, y) is < 10 nm. Meanwhile, the accuracy and z precision are both $\sim 20-40$ nm. The interfringe, interfringe$_x$ and interfringe$_y$, is shown in Fig.3.12 as function of z. As expected, for each z-position, there is a region of single values for interfringe$_x$ and interfringe$_y$, making the z-localization possible.

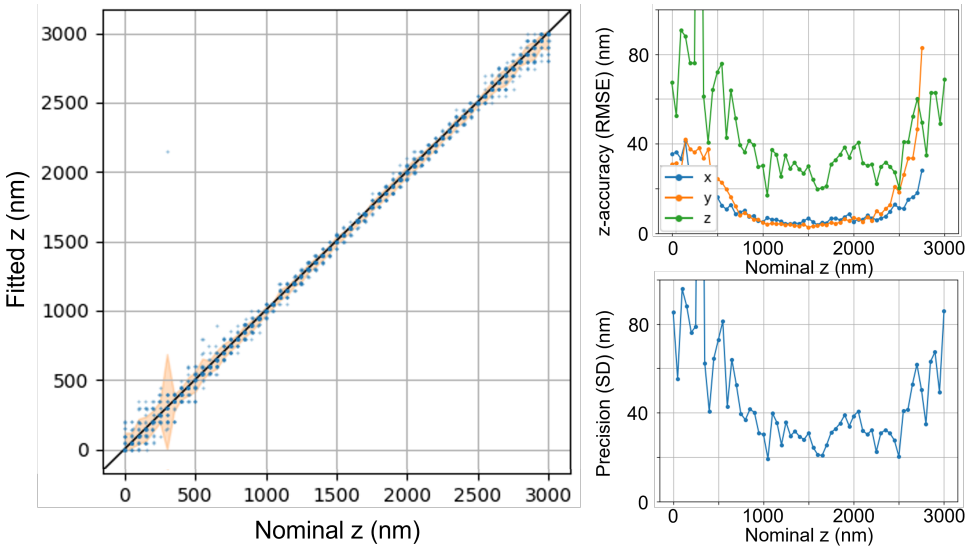

Figure 3.11: z-localization of a CNT fixed in the center of the field of view, the accuracy and precision are also shown. The number of photons in the signal > 18000.

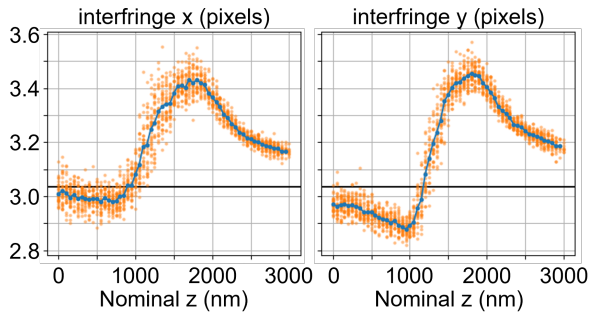

Figure 3.12: Interfringe inside the PSF of a CNT imaged with SELFI vs. z.

3.2.4 SELFI performance with SWCNTs

Fig.3.13 shows some examples of localized SWCNTs, focused and centered in the field of view, with different number of photons emitted.

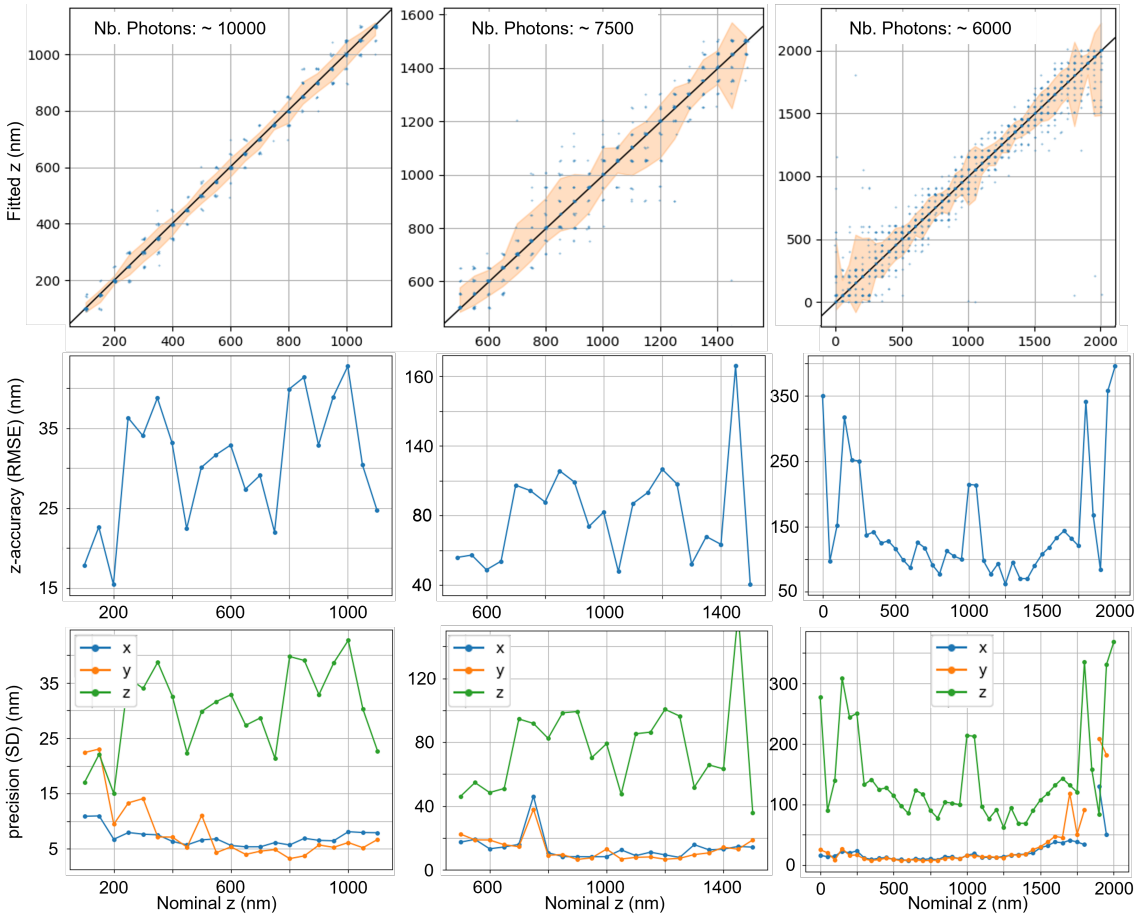

Figure 3.13: z-localization of SWCNTs fixed in the center of the field of view, but different photon budgets.

Remarkably, the signal of SWCNTs is much larger than the one obtained with the batch of PbS/CdS QDs, whose results are exposed in section 1.3.1. We observe how

the resolution decreases as the signal diminishes.

For each localized SWCNT in Fig.3.13, we have averaged the RMSE values for a region of 1 μm in z centered at the focus, resulting in the following axial accuracy values: 30 nm for a signal of 10000 photons, 80 nm for 7500 photons, and 106 nm for 6000 photons. Similarly, we averaged the SD values, obtaining the following precision: 30 nm for 10000 photons, 76 nm for 7500 photons, and 104 nm for 6000 photons. Let's recall that these results were obtained at an emission wavelength of 985 nm, meaning that the diffraction limit is $\sim$500 nm. Therefore, we have been able to obtain a resolution more than 16 times higher than the diffraction limit for photon budgets above 10000.

To have a better understanding on how the experimental precision (exp. prec.) and accuracy (exp. accu.) vary with the number of photons, we have localized SWCNTs with different emitted signals. Fig.3.14 shows a logarithmic plot on how the precision and the accuracy of the SELFI NIR setup changes as a function of the number of photons emitted on SWCNTs samples. Each point in the plot was calculated by averaging the SD or RMSE for a z-range of 1μm around the focus. The power law fit (fit prec. and fit accu.) shows that the resolution depends on the inverse square root of the photon budget (precision and accuracy $\propto$ (number of photons)$^{-0.5}$) as it is expected by shot noise limited detection, as discussed in section 1.1.1 [65].

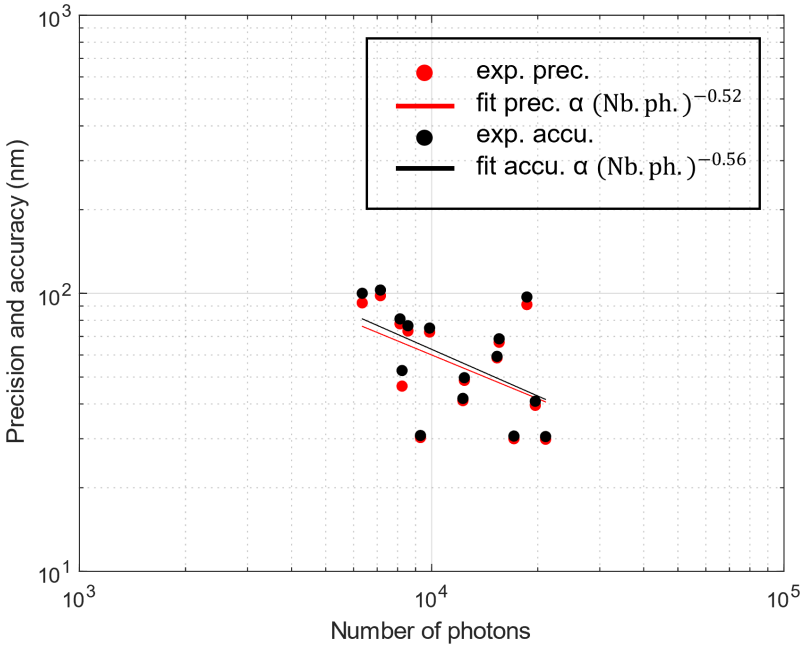

Figure 3.14: Logarithmic plot of z-localization precision and accuracy of NIR SELFI as functions of the number of photons emitted by SWCNTs.

So far, the experiments were perfomed by localizing short SWCNTs, i.e. nanotubes shorter than $\sim$ 500 nm as they can be considered as point-like emitters as

long as their length is smaller than the diffraction limit. Nevertheless, we should keep in mind their one-dimensional shape. The one-dimensional feature of carbon nanotubes might become a limitation in our method for 3D localization since this feature affects the Fourier transform of a SWCNT image, as shown in Fig.3.15. Therefore, when comparing the image of a long carbon nanotube with one of a point-like calibration nanotube in the process of localization, the Pearson coefficients will decrease, leading to a diminishment of the z-resolution.

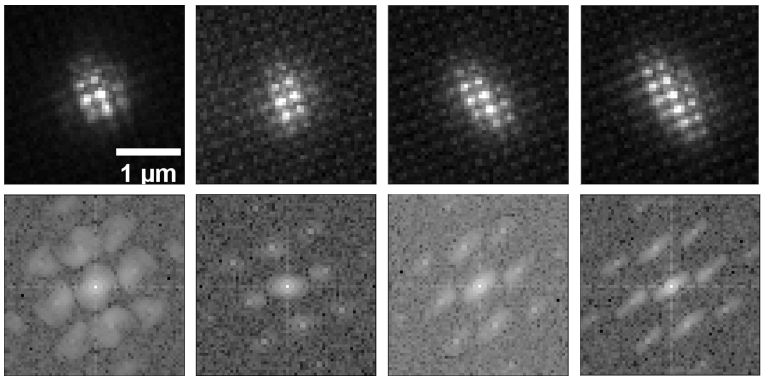

Figure 3.15: Carbon nanotubes of different lenghts and their correspondent Fourier transforms.

3.3 3D single-particle tracking of carbon nanotubes

In the present section, we show our studies on single-paticle tracking (SPT) with carbon nanotubes in various media, such as isotropic medium (glycerol-water mixture), anisotropic medium (agarose gel), and brain tissue. After, we explore some ideas for further studies on how to improve 3D SPT. And finally, the analysis process followed to perform 3D SPT and obtain these results is explained.

3.3.1 3D single-particle tracking of carbon nanotubes in isotropic medium

Particles moving in isotropic media follow a Brownian motion, meaning that their movement is random as a result of their continuous impact with the molecules forming the surrounding medium. Brownian motion has been widely studied at the microscopic level and it is the simplest case [129]. Reason why we have started our experiments on SPT with SWCNTs in glycerol-water mixture, which is an isotropic medium with high viscosity. We have analyzed the dynamics in terms of the mean square displacement (MSD).

3.3.1.1 Sample preparation and imaging protocol

HiPco DOC SWCNTs were dissolved in water (1:7), then incorporated with glycerol to finally have a glycerol-water (3:1) mixture. 50 μL of the solution were "sandwiched" between two coverslips and sealed with grease to avoid convection. After, it is important to wait for an hour before starting the acquisitions to let decrease the drift due to the flux exerted on the solution during the sample preparation.

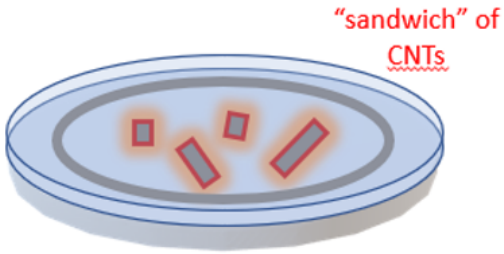

Figure 3.16: Sample preparation of SWCNTs diffusing in glycerol-water mixture. The solution is "sandwiched" between two coverslips and sealed with grease.

The optical setup used is the same one as shown in Fig.3.9. Images were taken 10 μm far from the surface, and the exposure time used was 100 ms.

3.3.1.2 Analysis procedure for 3D single-particle tracking

To perform 3D SPT analysis, we start with 2D SPT by using TrackMate, a Fiji plugin that applies SMLM analysis techniques to reconstruct 2D trajectories of moving targets. To do so, the SELFI movies are first low-pass filtered to have the intensity profiles without the interferogram, and be able to use SMLM. Consider now a single nanotube, its (x, y) position in every frame is uploaded to our analysis script to target the nanotube in the original movie with the interference pattern. After, a calibration z-stack is used to determine the axial localization of the nanotube in every frame, leading to the determination of the three-dimensional trajectory of the nanotube in question. Fig.3.17 is a schematics summarizing this process.

We should also consider that the working range of z-localization is of 1 μm. Reason why the trajectories' projection in z may look slightly flat compared to the projections in x and y. Nevertheless, 3D single-particle tracking in the NIR with subwavelength precision is a breakthrough as we have gone further than anyone else in the topic.

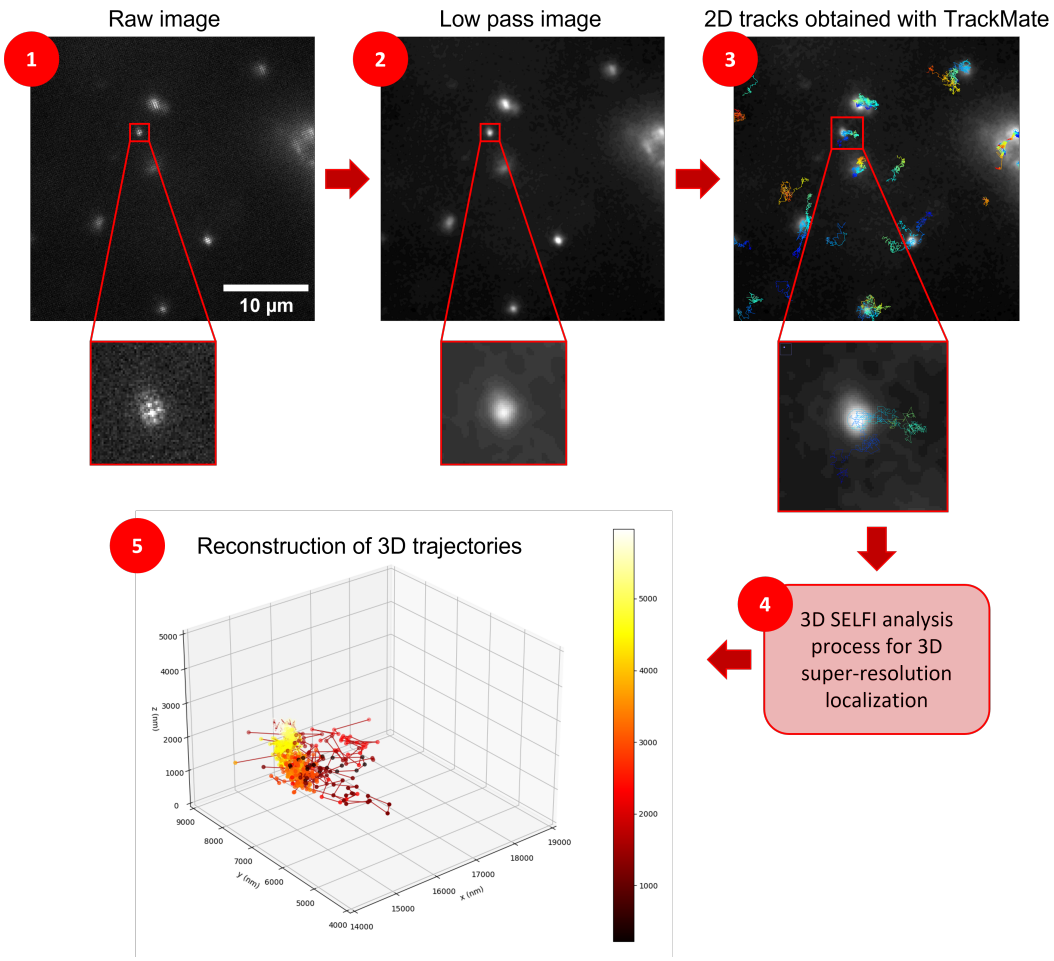

Figure 3.17: Schematics of 3D single-particle tracking process with SELFI.

3.3.1.3 Results and discussions

We present now the results obtained for 3D SPT of SWCNTs in glycerol-water isotropic media. 26 different trajectories were acquired. Fig.3.18.a and 3.19.a show two examples of 3D trajectories of SWCNTs diffusing in (3:1) glycerol-water mixture by showing the trajectories' projection in planes (x, z), (y, z), and (x, y), as well as the trajectories in 3D. Fig.3.18.b and 3.19.b show the evolution of x and z positions of the nanotubes with time (frame number). Fig.3.18.a shows a regular stochastic track in (x, y) where the diffusion in x occurs over a distance $\sim 4\mu$m, and $\sim 3\mu$m in y. Whereas in (x, z) and (y, z), we observe that the distance covered in z looks $< 1\mu$m. It may appear as the distance traveled in z is shorter, but it is actually linked to the working range of SELFI, which is $\sim 1\mu$m. In Fig.3.18.b, we observe the displacement in x and z as functions of time (frame). The blank spaces in the displacement plot correspond to frames where the particle has gone out of focus or to localizations excluded during the analysis process due to their non-physical values. The x and z displacements seem to exhibit random behaviour as expected for stochastic motion.

In the following, we try to quantify this information.

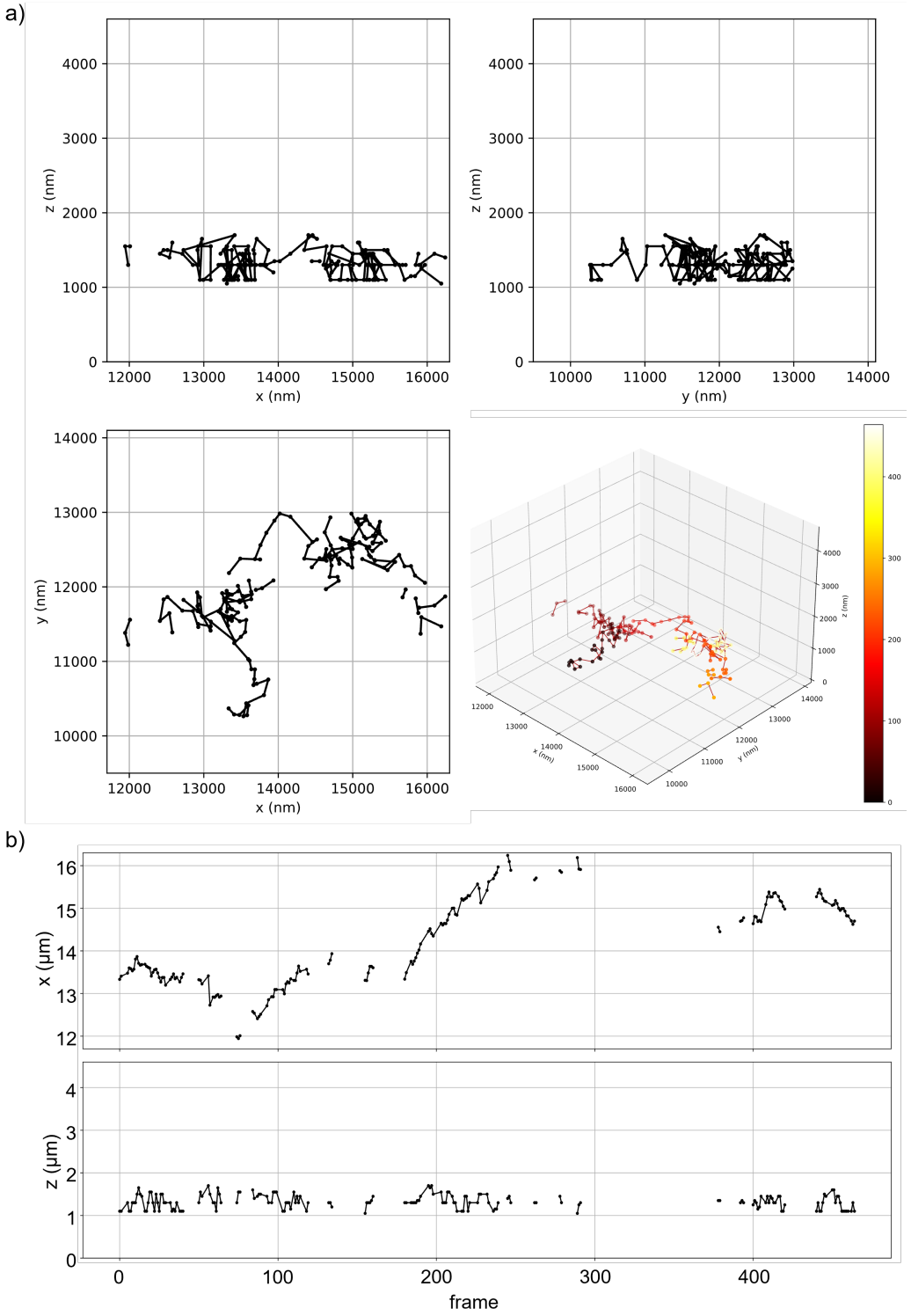

Figure 3.18: Diffusion of SWCNTs in (3:1) glycerol-water mixture. a) Trajectory projections in planes (x, z), (y, z), and (x, y). b) frame vs. x position, and frame vs. z position.

Fig.3.19.a shows another example of an stochastic trajectory in (x, y). Diffusion

in x occurs over a distance $\sim 3.5\mu$m, $\sim 3\mu$m in y, and ~ 800nm in z. The later as a result of SELFI's working range. In Fig.3.19.b, we again notice that displacements in x and z follow what would be expected from stochastic motion.

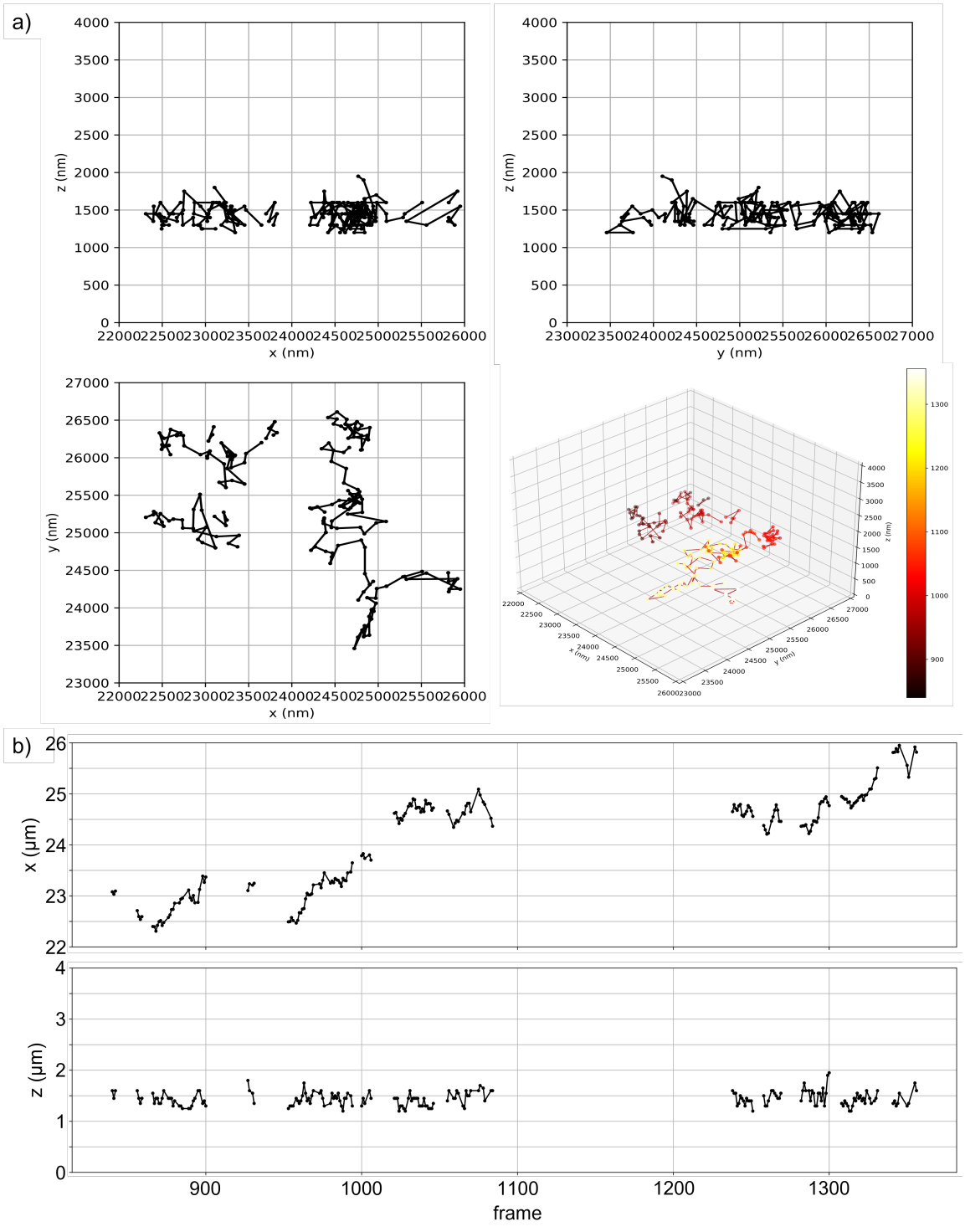

Figure 3.19: Diffusion of SWCNTs in (3:1) glycerol-water mixture. a) Trajectory projections in planes (x, y), and (x, z). b) frame vs. x position, and frame vs. z position.

These two tracks are among the longest ones, meaning that these SWCNTs stay in the depth of focus. This bias in the selection of trajectories is reflected in the space covered by the motion of SWCNTs in x, y, and z since the space traveled in z is smaller than in x and y. Nevertheless, this is not a general rule for their motion since there are other NTs whose movement is more even along the three directions or occurs mostly along z. Yet, these other kind of trajectories are too short to be analyzed since SWCNTs would move out of focus faster.

To assess the performance of SELFI for 3D single-particle tracking, we have calculated the experimental MSD along x, y, and z by using Eq.3.8. The MSD has been calculated for a time interval $t = 100$ ms, equivalent to one frame acquired. As the motion of nanotubes is Brownian in glycerol-water medium, we expect the calculated MSDs in the three different directions to be the same as there is no preference in the direction of motion. The MSD has been calculated for 26 trajectories. Fig.3.20.a shows the experimentally obtained values of MSD in y (black dots) and MSD in z (red dots) as functions of MSD in x. The black dotted line follows a slope of 1, which is satisfied by MSD_y as a function of MSD_x, meaning that $\mathrm{MSD}_y^{exp} \approx \mathrm{MSD}_x^{exp}$. The red dotted line shows a linear fit of the red dots data (MSD_z^{exp} vs. MSD_x^{exp}) with an offset while forcing the slope to be 1. This offset between the red and black dotted lines ($MSD_z^{exp} - MSD_y^{exp}$) can be determined by considering the following MSD equations where is neglected the effect of the particle moving during the exposure time [129]:

$$\begin{aligned} MSD_y^{exp} &= MSD_y^{true} + 4\langle \Delta y \rangle^2 \quad \text{and} \\ MSD_z^{exp} &= MSD_z^{true} + 4\langle \Delta z \rangle^2, \end{aligned}$$

where MSD_y^{true} and MSD_z^{true} are the true MSD values in both directions, and Δy and Δz are the precision errors in y and z, respectively. Therefore, the offset is

$$MSD_z^{exp} - MSD_y^{exp} = 4\left(\langle \Delta z \rangle^2 - \langle \Delta y \rangle^2\right) = 0.004\,\mu\mathrm{m}^2. \tag{3.9}$$

In Fig.3.20.b, we have shifted the MSD_z^{exp} data by subtracting $4\left(\langle \Delta z \rangle^2 - \langle \Delta y \rangle^2\right) = 0.004\,\mu\mathrm{m}^2$. We now observe that MSD_z^{exp} and MSD_y^{exp} are indistinguishable, which indicates that the difference between MSD_z^{exp} and MSD_y^{exp} in Fig.3.20.a is linked to the discrepancy between the lateral axes and the axial axis resolutions, and calculated to be

$$\frac{\sqrt{\langle \Delta z \rangle^2 - \langle \Delta y \rangle^2}}{4} = \frac{\sqrt{4000\,\mathrm{nm}^2}}{4} \sim 32\,\mathrm{nm}.$$

What is more, this is in agreement with the results obtained in section 3.2, where we showed that the resolution in x and y is <10 nm while in z is <40 nm for bright SWCNTs.

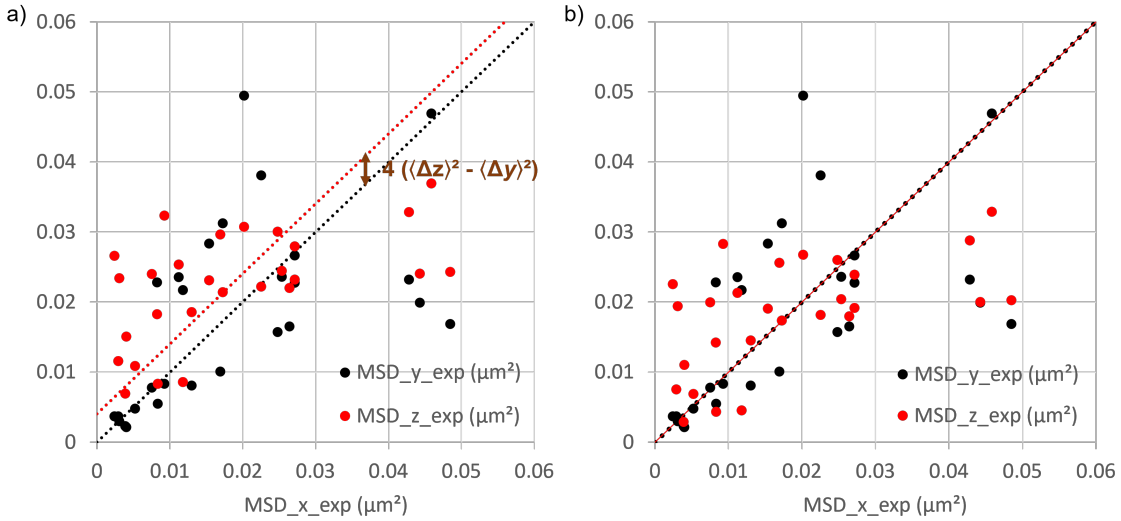

Figure 3.20: MSD of 26 different trajectories.

Another way to study the movement of SWCNTs is through the displacement that occurs from one consecutive frame to another. In other words, for each trajectory, we plot a histogram of displacements within 100 ms. Fig.3.21 and 3.22 are the displacement histograms of the trajectories shown in Fig.3.18 and 3.19, respectively.

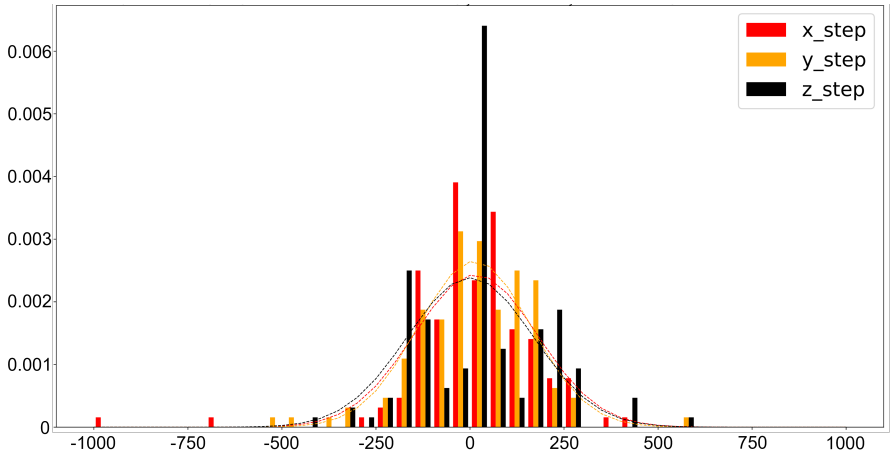

Figure 3.21: Histogram of displacements within 100 ms of trajectory in Fig.3.18.

The bin of the histogram is 50 nm since 50 nm corresponds to the minimum displacement in z limited by the shifting of the objective position when recording a calibration z-stack. As observed in Fig.3.21 and 3.22, most of the displacements in x and y do not exceed ± 250 nm. Since 2D SPT is well understood, and the resolution in (x, y) is higher than in z, we take the displacements in x and y as reference in regards of what to expect from z displacements. Therefore, we have discarded outliers when their z-displacements in reference with the consecutive frame are higher than ± 250 nm since they are more likely to be erroneous localization points. We may observe

that in Fig.3.21 and 3.22 the displacement distribution is very similar between x, y, and z, meaning that SELFI works well as a 3D super-resolution technique for 3D SPT applications.

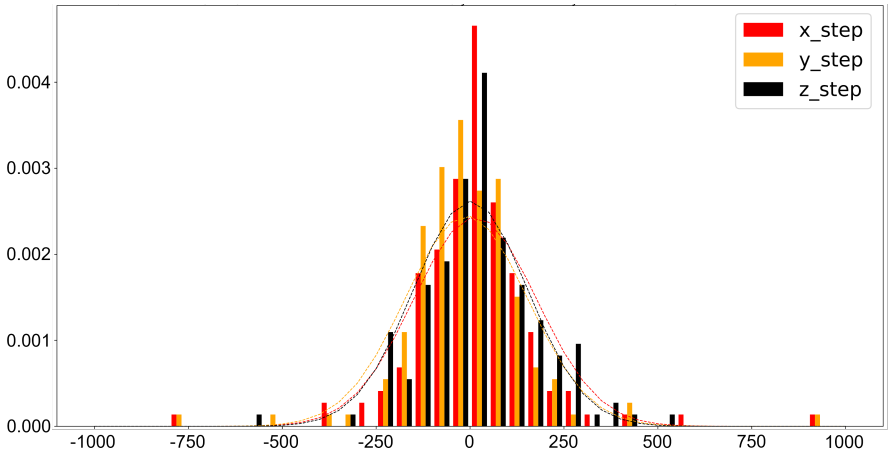

Figure 3.22: Histogram of displacements within 100 ms of trajectory in Fig.3.19.

In the following lines, we consider and discuss the role of SWCNTs' orientation along their motion when diffusing in a medium. SWCNTs' absorption and fluorescence dipoles are aligned with their long axis [130, 131]. Therefore, if we consider that all SWCNTs in the sample are evenly excited, then we are able to observe them for as long as they are not aligned with $\vec{k}$, propagation direction of the excitation laser, which is parallel to z, nor we can observe them when their angle with z is too small, as shown in Fig.3.23.a. In addition, ellipsoidal bodies following Brownian motion move faster in the direction parallel to their longer axis. In fact, when the length of the NT is considered to be infinite in relation with its diameter, the MSD for motion parallel to its long axis is twice bigger than the MSD for motion perpendicular to its long axis [132].

Also, during the analysis process, we have selected trajectories that are mainly anisotropic given that they spend more time in the (x, y) plane than in z. Therefore, we might wonder if this anisotropy is linked to the anisotropy of SWCNTs themselves. To clarify this query, we must consider the rotational dynamics during the image acquisition of diffusing SWCNTs. Rotation of SWCNTs also has its implications on signal variation as it changes from 100% when they perpendicular to $\vec{k}$ to 0% when they are parallel to $\vec{k}$, passing through all the possible angles of rotation and therefore through different intensity values (Fig.3.23.c).

Let us introduce the fluorescence *autocorrelation time*, i.e. the minimum time resolution necessary to observe intensity fluctuations due to rotation, which is about 30 ms for nanotubes of lengths below 0.5 μm, see ref. [127]. The autocorrelation time implies that we need an exposure time of 30 ms or less to observe intensity variations.

Since the exposure time used in the following diffusion experiments is 100 ms, then there is already an average of different angular positions in one frame acquired. Therefore, neither the problem of orientation-dependent diffusion nor orientation-dependent detection play a role in the trajectories acquired during these experiments, allowing us to consider nanotubes' diffusion as isotropic.

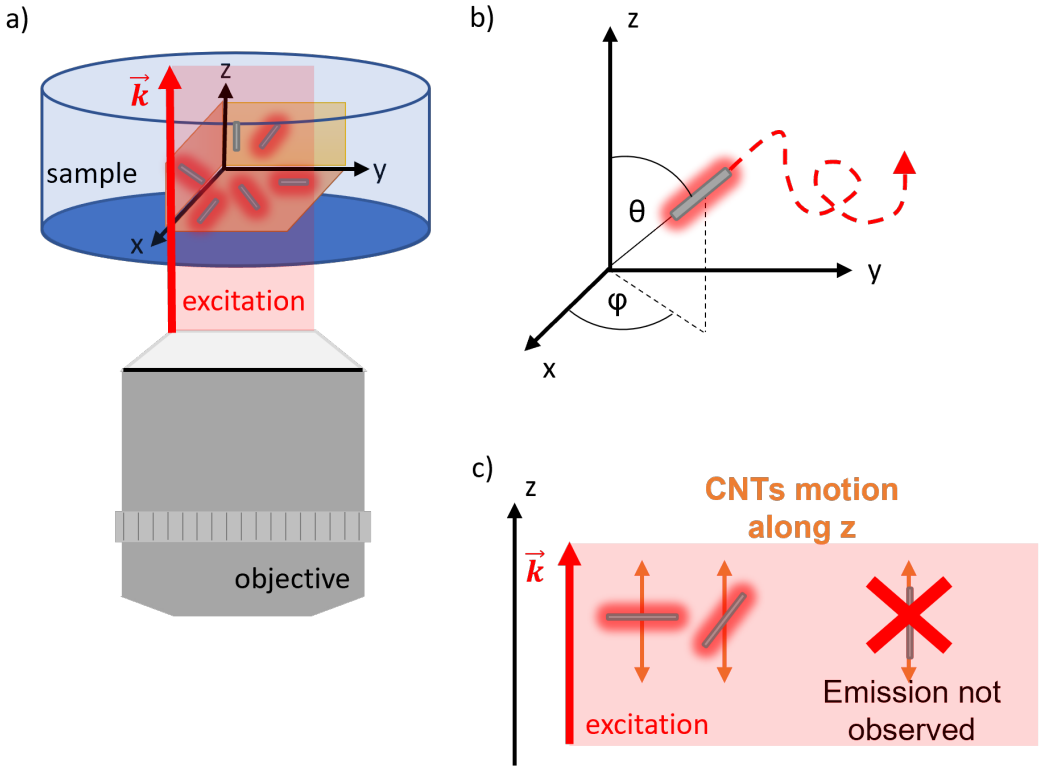

Figure 3.23: a) Different possible dispositions of SWCNTs in space. The (x, y) plane represents the sample surface, and z is the optical axis. SWCNTs parallel to z cannot be observed since they do not emit light through their extremes. b) Observable motions in z of SWCNTs. When the NT moves parallel to z, it is not seen by the observer. c) Initial angular orientation of NT.

The results obtained in this section have demonstrated the successful performance of SELFI for 3D SPT in the near-infrared window. We have determined that from the 3D trajectories we can extract information in 3D about the dynamics of the media explored by the carbon nanotubes either by means of the MSD or by the displacements distribution.

3.3.2 3D single-particle tracking of carbon nanotubes in anisotropic medium

In the present section, we present experiments of 3D SPT of SWCNTs in agarose gel. We chose agarose gel because when it solidifies, a 3D web of channels is formed by

helical fibers composed by agarose polymer chains. These channels have diameters going from ∼50 nm to > 200 nm. Therefore, SWCNTs move within them in a characteristic manner: back-and-forth, and on and on, following the paths defined by the gel structure. If the 3D SPT of SWCNTs is working, we should be able to reconstruct trajectories that look similar to Fig.3.24.

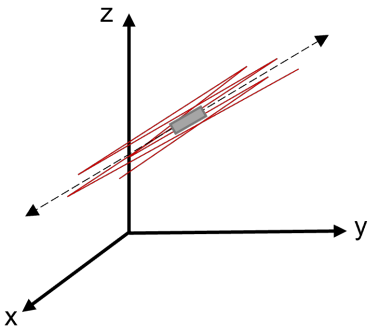

Figure 3.24: Back-and-forth motion of SWCNTs when diffusing in agarose gel.

3.3.2.1 Sample preparation and imaging protocol

The samples were made by using HiPco DOC SWCNTs 5% concentrated in 1% agarose gel. Agarose is first solubilized in water by heating it until the mixture boils. Right after, SWCNTs are added into the agarose solution, and mixed with a pipette. After, the 200 μL of the solution are added on a coverslip. The gel solidifies after one hour, only then we proceed with the imaging process. Images were taken 10 μm deep into the sample to avoid surface constrains in the motion. Fig.3.25 depicts a schematic of these samples. The optical setup used is the same one as portrayed in Fig.3.9, where SWCNTs were excited with an 845 nm laser. Different exposure times were used (30, 50, and 100 ms) to play with two different factors: first, higher exposure time means higher photon budget per frame, and second, shorter exposure time means more resolution in capturing the movement of SWCNTs.

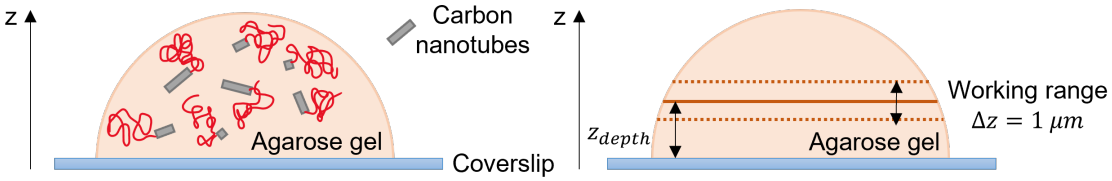

Figure 3.25: Sample of diffusing carbon nanotubes in 1% agarose gel. Tracks represented by red trails. Images are taken ∼ 10 μm deep into the sample, while the working range of SELFI is 1 μm centered at focus.

3.3.2.2 Results and discussions

Fig.3.26 shows four consecutive frames of a cropped movie of nanotubes diffusing in 1% agarose gel. We observe that the marked nanotube moves out of the focus as the movie evolves along the frames.

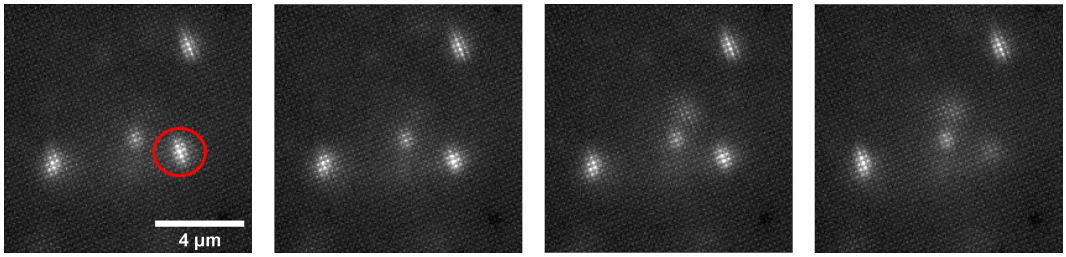

Figure 3.26: Four consecutive frames of a cropped movie of HiPco DOC carbon nanotubes diffusing in 1% agarose gel. The marked nanotube moves along z as it defocuses throughout the frames. Exposure time: 100 ms.

The information concerning the calibration nanotube is shown in Fig.3.27. We observe that, for a signal of $\sim$ 14000 photons, the average precision (SD) in a 1 μm range centered at the focus is $\sim$ 6 nm in (x, y), and $\sim$41 nm in z. The average accuracy (RMSE) is $\sim$42 nm in z. These values correspond to the ideal case of a high-signal point-like nanotube fixed in the center of the field of view.

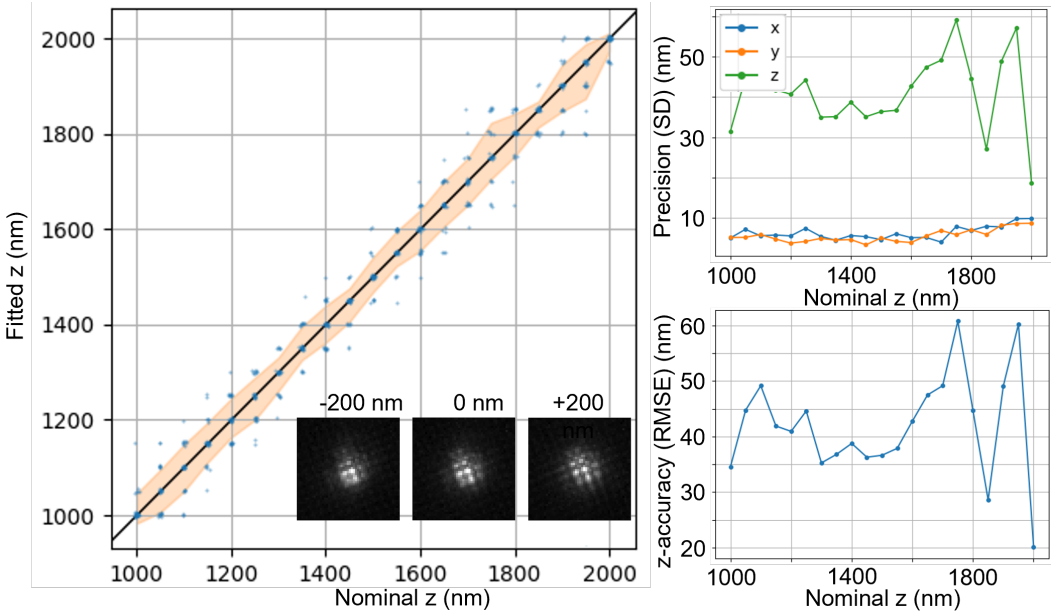

Figure 3.27: z-localization of the calibration nanotube fixed in the center of the field of view, the accuracy and precision are also show. Number of photons: $\sim$ 14000.

The calibration stack is used to localize the moving nanotubes. Fig.3.28, 3.29, and 3.30 are examples of reconstructed three-dimensional trajectories where we show

the projections of the tracks in the planes (x, z), (y, z), and (x, y), as well as the 3D trajectory where the color represents the time evolution. Fig.3.28 and 3.29 show a clear back-and-forth motion of SWCNTs in the (x, y) projection of the trajectories. When looking at the (x, z) and (y, z) projections, Fig.3.28 shows a back-and-forth motion as well, whereas Fig.3.29 shows an interesting curved trajectory shape which is consistent with a realistic track when having channeled structures. Fig.3.30 shows a different type of track, where the CNT seems to be more stuck in the channels and does not moves as much as the SWCNTs in the other two examples.

The trajectories reconstructed in this section validate the performance of SELFI for applications on 3D SPT of SWCNTs as we are able to observe the back-and-forth motion in 3D expected of SWCNTs when diffusing among the web of channels in the agarose gel. These results allows us to go one step further and demonstrate SELFI for 3D SPT of SWCNTs in more complex structures, such as the living brains.

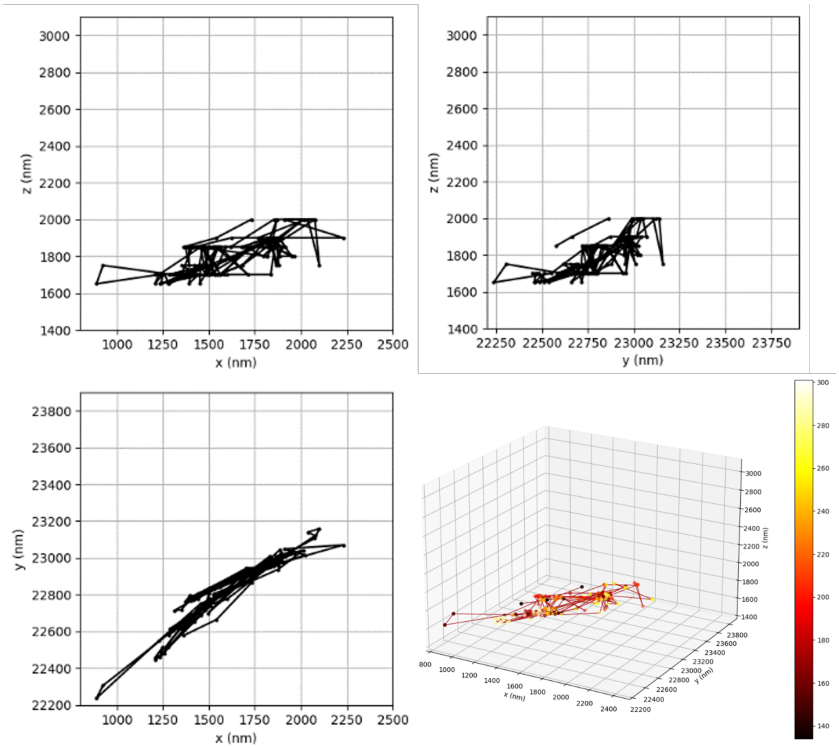

Figure 3.28: Trajectory reconstruction of a SWCNT diffusing in 1% agarose gel. Exposure time: 30 ms.

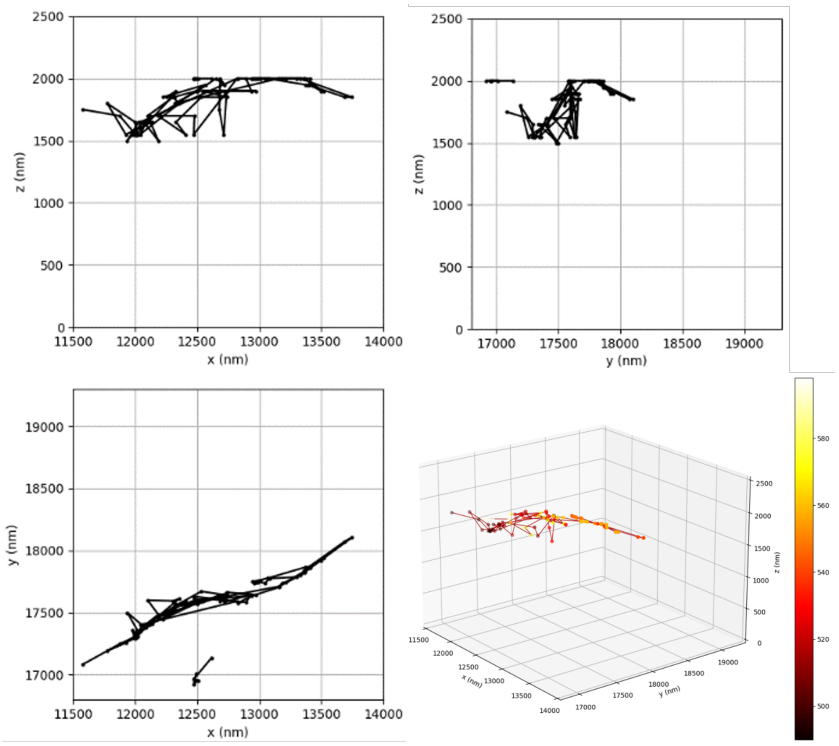

Figure 3.29: Trajectory reconstruction of a SWCNT diffusing in 1% agarose gel. Exposure time: 50 ms.

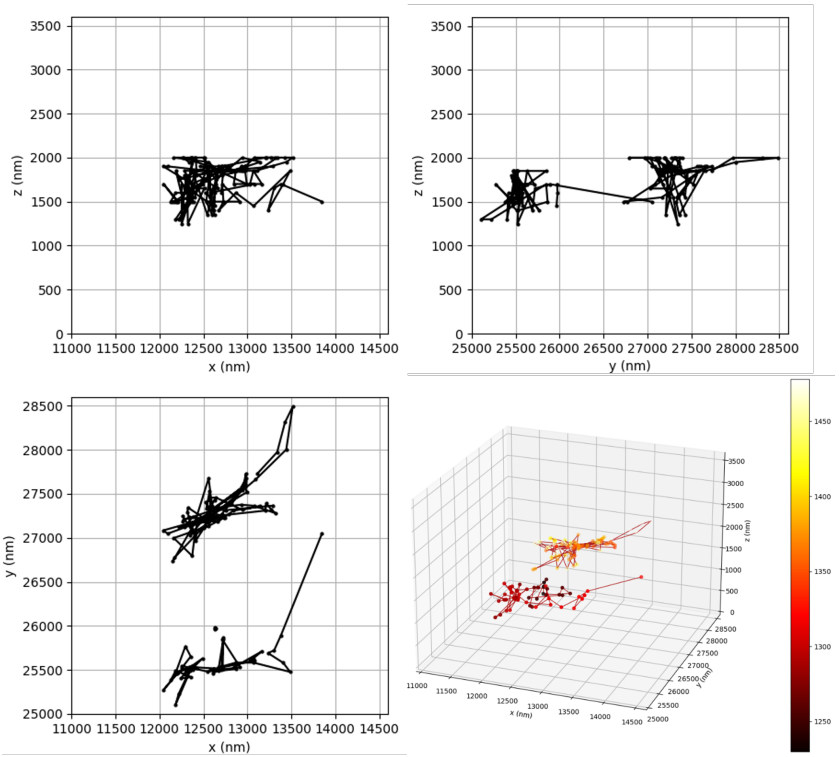

Figure 3.30: Trajectory reconstruction of a SWCNT diffusing in 1% agarose gel. Exposure time: 50 ms.

3.3.3 Single-particle tracking in the brain extracellular space

In this section, we discuss the results obtained on the experiments performed on 3D SPT of SWCNTs in the brain extracellular space (ECS) of organotypic brain slices (OBS), which has been the main motivation to develop this thesis project. We have used OBS as they offer a three-dimensional model of the brain with preservation of cytoarchitecture that is physiologically appropriate [133, 134]. What is more, OBS have shown to be highly helpful in the *in vitro* analysis of brain cellular and molecular processes [135]. In our research team, we focus our studies on the application of SWCNTs on SPT for the exploration of the brain ECS. The importance of understanding the morphology and physiology of the brain ECS, comprising the space in between brain cells, is crucial yet still poorly understood, although it occupies one fifth of the brain volume. In the following pages, we present the first results obtained on 3D SPT in the brain ECS of organotypic brain slices.

3.3.3.1 Sample preparation

The experiments were performed in organotypic brain slices, and we followed the experimental protocol described in reference [30].

Slices were provided by Morgane Meras from the team of Laurent Groc, our collaborator in the Interdisciplinary Institute for Neuroscience (IINS) in Bordeaux, France. Slices were taken from postnatal days 5 to 7 Sprague-Dawley rats and cut to have a thickness of 350 μm. After, they were cultured during 12–14 days in vitro (DIV). For SWCNT incubation, we have used pristine CoMoCAT PL-PEG SWCNTs, a suspention prepared with 3 μL SWCNTs solution and 10 μL of culture medium was added to the slices for 2 hours at 35 °C. After, slices were imaged in imaging medium containing (in mM): 130 NaCl, 2.5 KCl, 2.2 $CaCl_2$, 1.5 $MgCl_2$, 10 HEPES, and 10 D-glucose. Each slice is imaged during 1 hour to ensure that we work on healthy slices. Fig.3.31 summarizes the preparation of brain slices.

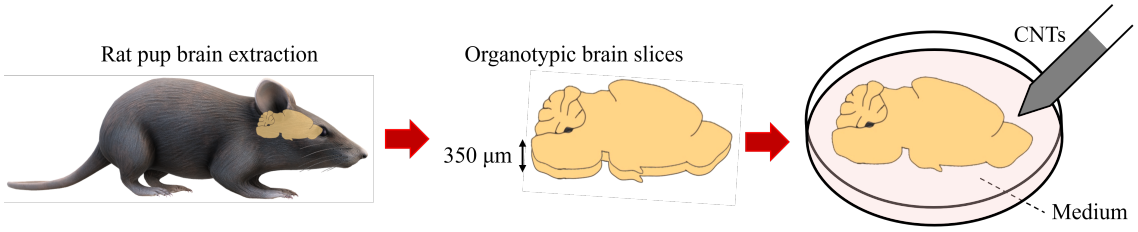

Figure 3.31: Schematic of brain slices for extracellular space exploration through single-particle tracking of carbon nanotubes.

3.3.3.2 Imaging protocol

To perform SPT experiments of SWCNTs in brain slices, we not only imaged SWCNTs but also brain autofluorescence. In fact, we use the autofluorescence to know we are inside the tissue, and to identify brain cells. Autofluorescence may come from intrinsic components of the brain cells, such as Lipofuscin [136] and other different types of lipids [137] among different wavelength ranges. We imaged autofluorescence around 525 nm.

The setup was adapted to image the autofluorescence in another camera connected to another exit of the microscope so that we do not have auto-interference there. Fig.3.32 shows an schematic of the optical setup. To excite the tissue, a 470 nm LED from Thorlabs is used. The filter cube used was composed by: a 495 nm dichroic (FF495-Di03-25x36) from Semrock, a 472/30 nm single-band bandpass filter (FF02-472/30-25) from Semrock as well, and a 525/50 nm single-band bandpass filter (HQ525/50m) from Chroma. SWCNTs emission was acquired through the SELFI part of the optical setup, we used an 845 nm diode laser to excite them, and the cube filter described in section 1.2.3. The second detector used for autofluorescence imaging is a Ninox InGaAs camera which has extended detection in the visible, with a pixel size of 15 μm, from Raptor Photonics. The exposure time used for both autofluorescence and SWCNTs emission was 150 ms.

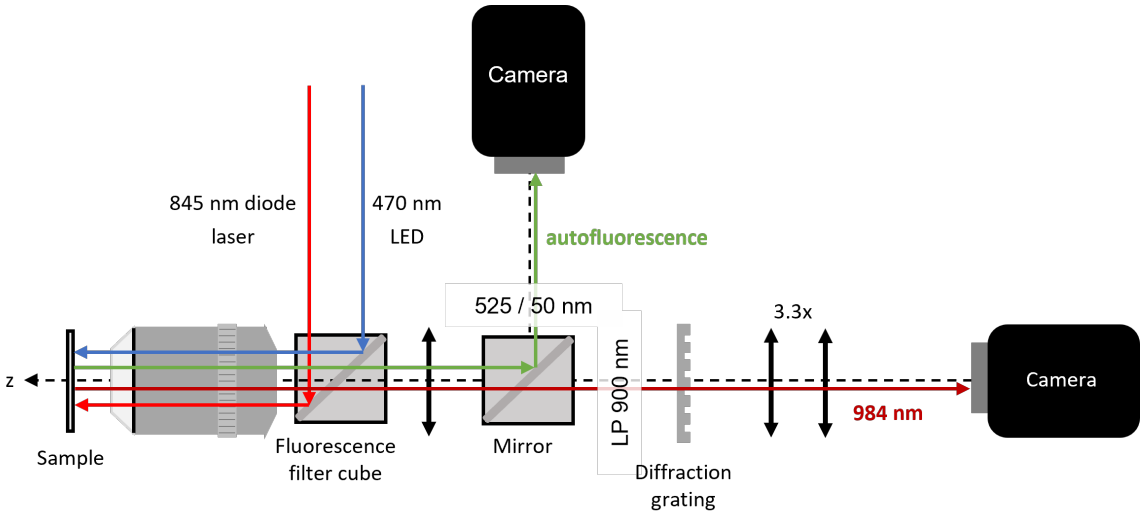

Figure 3.32: Two-cameras setup to image SELFI in the NIR plus brain tissue autofluorescence $\sim$ 525 nm.

3.3.3.3 Results and discussions

In the present section, we exhibit some examples of the trajectories followed by SWCNTs diffusing in the brain ECS of organotypic slices (Fig.3.33 - 3.39). As mentioned above, we used CoMoCAT PLPEG SWCNTs. It is important to keep in mind the

dimensions of the NTs imaged, (6,5) nanotubes. They present a diameter of 0.757 nm [138], however, after coating their diameter is of a few nanometers, still being them thin probes to diffuse through the ECS. Also, only the smallest bright nanotubes ($\sim 100 - 500$ nm) were the ones tracked as SELFI works in spherical objects with diffraction limited sizes. The photostability of CoMoCAT PL-PEG nanotubes allowed us to acquire long movies, from 1500 to 3000 frames, resulting in acquisitions up to 9 minutes long. Movies were taken deeper than 5 μm into the tissue as we want to avoid damaged cells in the surface, and reach untouched tissue. Table 3.1 enlists the depths at which the different trajectories shown here took place. We may notice that trajectories cover bigger lateral area as SWCNTs are closer to the surface. This is consistent with the fact that is more difficult for them to access deeper into the tissue. We may also observe again that diffusion in z is limited by the working range of SELFI. The resolution achieved depends on the number of photons emitted by each nanotube. In the case of bright SWCNTs (> 18000), precision in (x, y) is $<$ 10 nm, while accuracy and precision in z are both $\sim 20 - 40$ nm.

Trajectory	Fig.3.33	Fig.3.34	Fig.3.35	Fig.3.36	Fig.3.37	Fig.3.38	Fig.3.39
Depth (μm)	9	14	15	27	27	66	66

Table 3.1: Trajectories' depth inside the tissue.

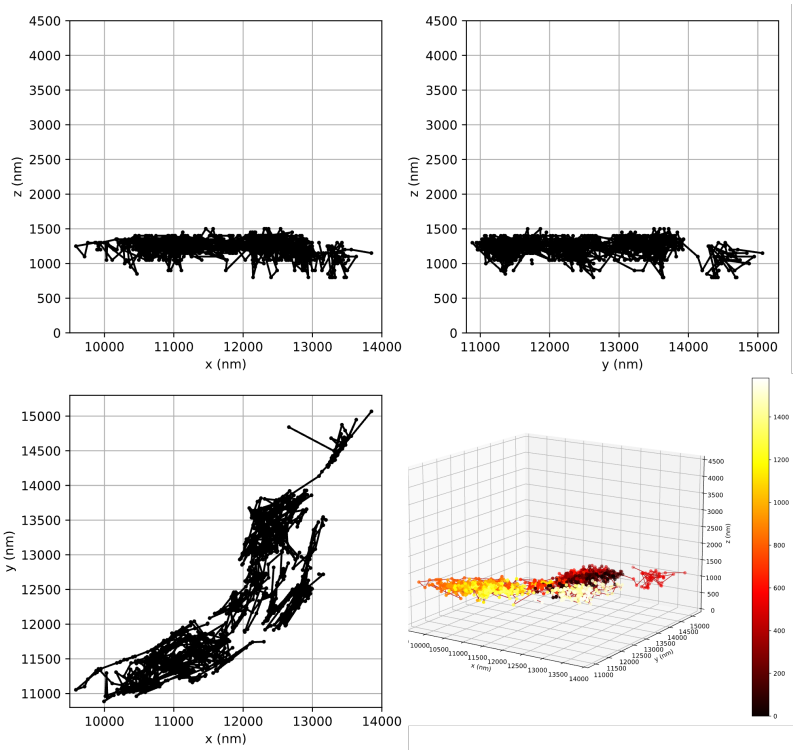

Figure 3.33: Example 1 of 3D trajectory of a single SWCNT diffusing in the ECS of organotypic brain slices. Depth into tissue: 9 μm.

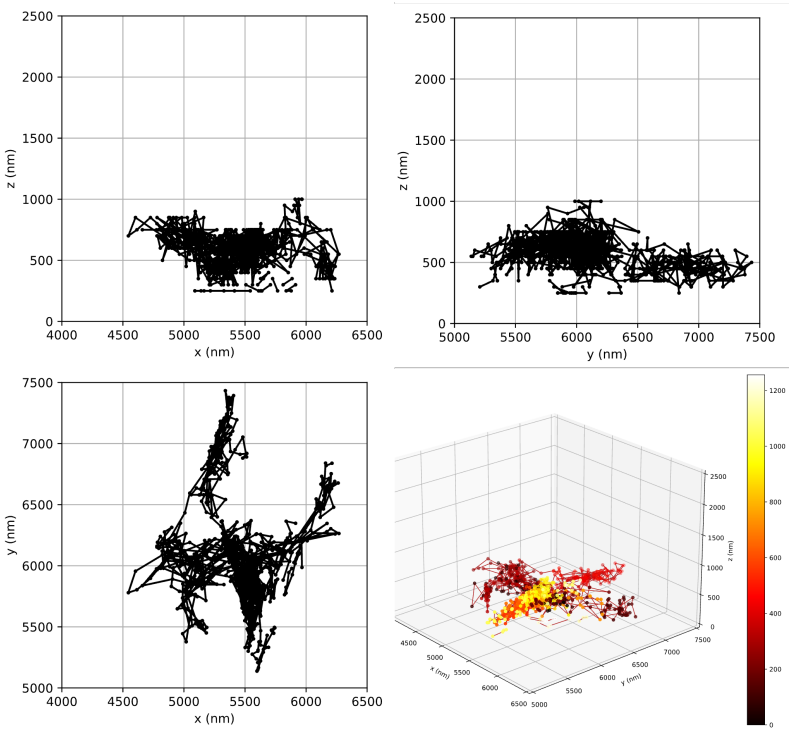

Figure 3.34: Example 2 of 3D trajectory of a single SWCNT diffusing in the ECS of organotypic brain slices. Depth into tissue: 14 μm.

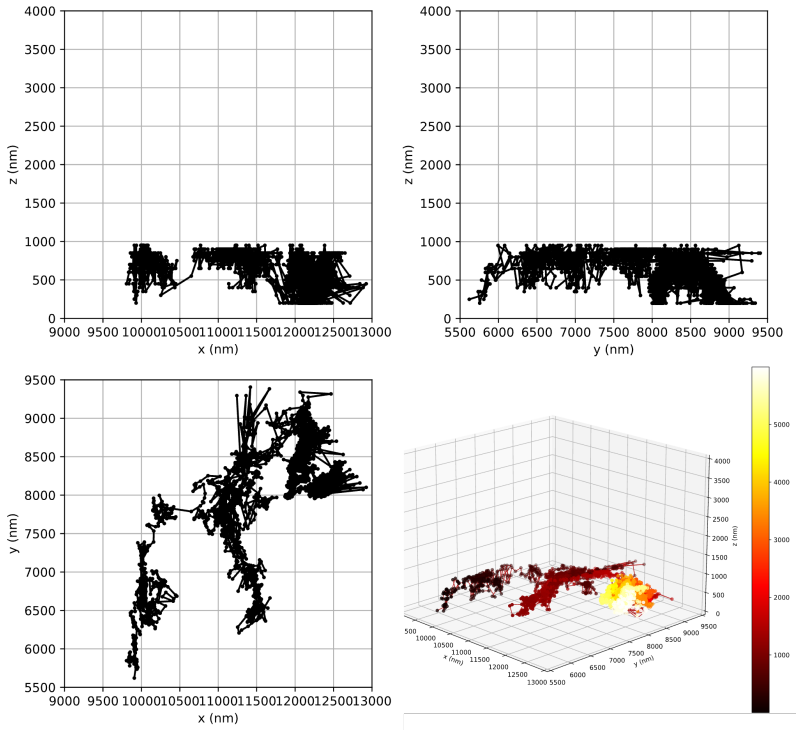

Figure 3.35: Example 3 of 3D trajectory of a single SWCNT diffusing in the ECS of organotypic brain slices. Depth into tissue: 15 μm.

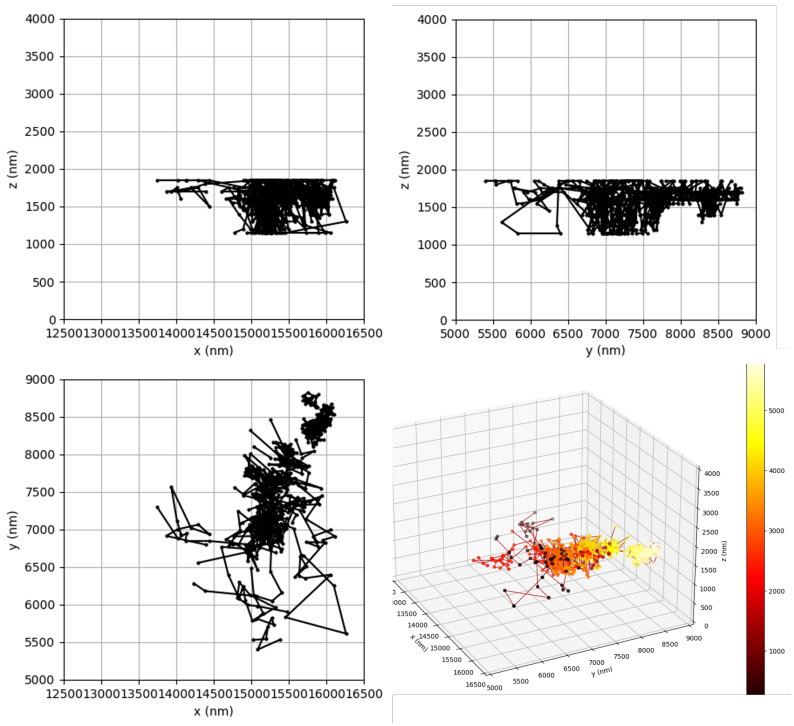

Figure 3.36: Example 4 of 3D trajectory of a single SWCNT diffusing in the ECS of organotypic brain slices. Depth into tissue: 27 μm.

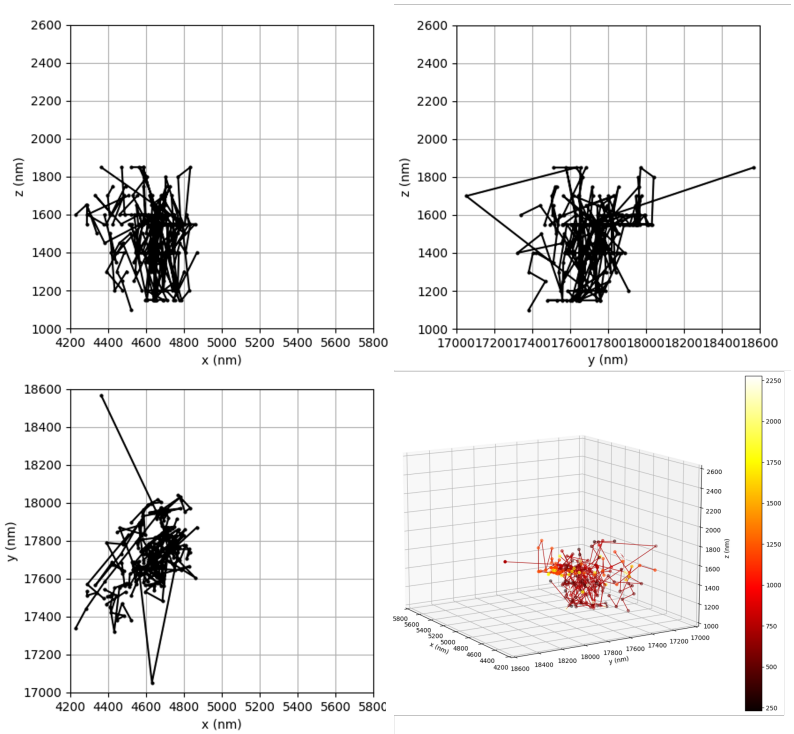

Figure 3.37: Example 5 of 3D trajectory of a single SWCNT diffusing in the ECS of organotypic brain slices. Depth into tissue: 27 μm.

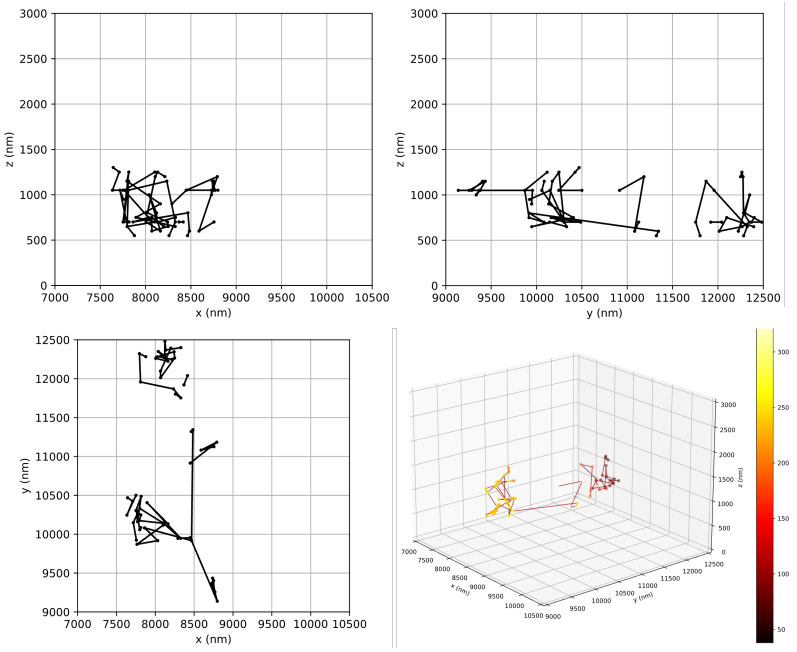

Figure 3.38: Example 6 of 3D trajectory of a single SWCNT diffusing in the ECS of organotypic brain slices. Depth into tissue: 66 μm.

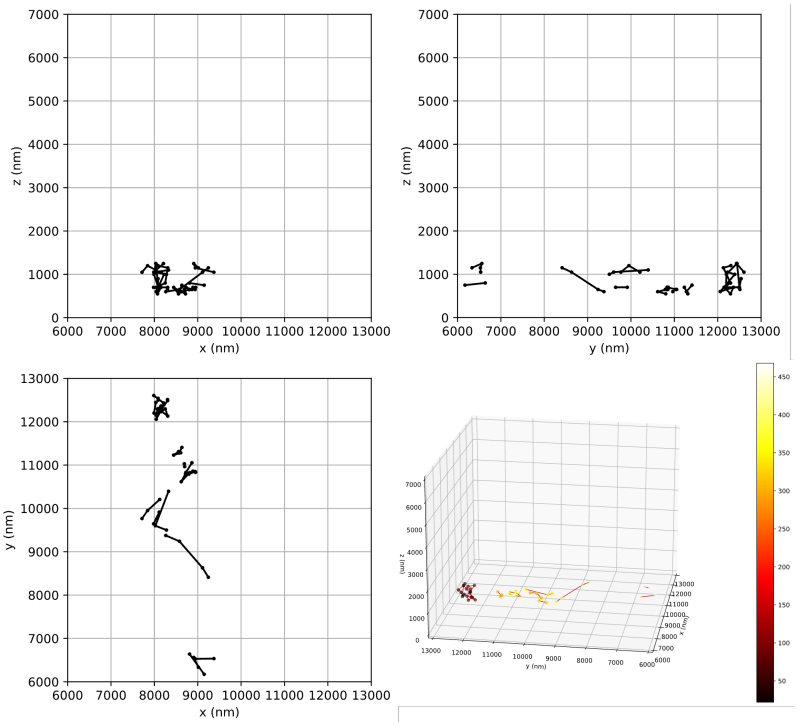

Figure 3.39: Example 7 of 3D trajectory of a single SWCNT diffusing in the ECS of organotypic brain slices. Depth into tissue: 66 μm.

In conclusion, SELFI in the near-infrared for deep tissue single-particle tracking of SWCNTs has been possible as we have been able to reconstruct 3D trajectories up

to 66 μm deep. Moreover, the availability to perform 3D SPT reveals the complexity and high content of information in one single trajectory. This is possible due to the bright signal of nanotubes almost unaffected by the bio-tissue. 3D SPT opens up interesting possibilities to study the morphology, spatial distribution, and dynamical properties of biological structures.

Conclusions

The work described in this manuscript has shown that SELFI in the near-infrared allows us to achieve 3D super-resolution localization and single particle tracking with a resolution of tens of nanometers at depths to up to 66 μm in living brain slices by using single-walled carbon nanotubes (SWCNTs) as luminescent nanoprobes. In the following pages, we discuss the conclusions we have made from the work presented in each chapter.

In the first chapter, we have introduced the principles of SELFI. We have shown that one way to extract the axial localization information of any single emitter is by accessing to the phase of the electromagnetic field of the light emitted by the particle in question. The phase is directly linked to the axial position of the emitter. One way to recover the phase is through interference of the signal emitted by the particle with itself, i.e. self-interference. We apply this principle to achieve 3D localization by placing a 2D phase-only diffraction grating a few hundreds of microns before the exit image plane of the microscope. Replicas of the signal are created and superpose, creating an interference pattern with almost the same size and shape as the one of particle's PSF. These concepts were explained through a conceptual and theoretical point of view. From equations, we have demonstrated that SELFI can be considered as an achromatic method. Besides, we have evidenced the dependency of the axial localization performance on the distance between the diffraction grating and the camera. After, we have established that, in order to extract the information enclosed in the interferogram, a demodulation in Fourier space can be used.

A single image generated with SELFI contains two independent variables: the intensity distribution from where we extract the intensity centroid to determine the lateral super-localization, and the phase leading us to get the axial super-localization. We have explained that the 3D localization routine consists on the following: fluorescent emitters are imaged with SELFI, each of them is analyzed separately. For a single image of a fluorophore, its Fourier transform is calculated. To determine the lateral position, we apply a low pass filter to the interferogram to retrieve the intensity distribution, and determine 2D super-localization. To determine the emitter axial position, we compare its FT to the calibration table of FTs obtained by making a z-stack of images of another reference fluorophore. The comparison is performed

through the calculation of Pearson coefficients.

The first chapter also exposes how the design of the SELFI optical setup for near-infrared emission was done. We have addressed the importance of having a proper signal sampling on the detector to achieve super-resolution. An ideal sampling is to have 3 pixels occupied either by the PSF or by fringe (of a SELFI image) to have 2D super-resolution or 3D super-resolution, respectively. In addition, we identified the instrumental considerations to make when choosing the parts conforming the SELFI setup.

A fundamental part of building SELFI is to identify where exactly to place the diffraction grating. This inquiry has been clarified and illustrated through a detailed experimental explanation. We have determined that the diffraction grating can be placed from 150 μm to 175 μm from the exit image plane of the microscope to have a good axial localization performance in the near-infrared and far-red regimes of emission.

The first chapter concludes with the performance characterization of 3D localization of nanoparticles in the near-infrared emission range (NIR) by using PbS/CdS quantum dots (QDs), and in the far-red by using TetraSpeck nanobeads. In the NIR the localization precision of a fixed QD emitting $\sim$ 10800 photons is both $<$ 10 nm along the lateral axes, while both precision and accuracy are $\sim$ 40 - 80 nm along z for a range of $\sim$ 1 μm around the focus. Furthermore, we have studied the effect of the photon budget as well as the distance from the center of the field of view on the localization resolution. We have determined that, in our setup, the resolution does not depend on the inverse square root of the photon budget as it would be expected by shot noise limited detection, but rather on the inverse of the photon budget as when the localization precision is limited by the background noise [65]. We have also demonstrated that the precision only depends on the number of photons but not on the distance of the emitter's position to the center of the field of view. Meanwhile, the accuracy does depend on both photon budget and distance from the center.

In the far-red emission range, we have determined the resolution for fixed particles with a photon budget of 10000 photons. The lateral precision is $\sim$ 5 nm, while in z is $<$ 50 nm. The z accuracy is $<$ 60 nm. We have compared the resolution of SELFI in the NIR and the far-red, and we have concluded that our SELFI setup, optimized for NIR wavelengths, is also robust in the far-red regime.

In the second chapter, we have explained the strategy developed to analyze 3D localization of fluorophores observed through the NIR SELFI setup. We have built two models that resemble the most two important features of SELFI PSFs: the intensity and the interferogram. These models are characterized by 14 independent parameters, two of them being the lateral position of the emitter. We have explained how we use super-localization to determine the (x, y) localization of the emitter. After, we have

shown how we use non-linear squares fitting to optimize the parameters. Then, we have presented the method we use for axial localization, which is the calculation of Pearson coefficients as a comparison method between the Fourier transform of the emitter to localize and a look-up-table of Fourier transforms of a calibration emitter. We have shown that Pearson coefficients is a useful analysis method as it is independent of the data scale, which is very practical given that, experimentally, we always deal with intensity fluctuations. Finally, we have introduced an alternative method for axial localization based on machine learning techniques. However, we have demonstrated that this method currently is not as robust as Pearson coefficients.

In the third chapter, we have presented the applications of near-infrared SELFI to carbon nanotubes emitting at 985 nm. First, we have demonstrated that SELFI successfully localizes immobilized short carbon nanotubes ($\sim$ 100 - 500 nm in length). We have determined that, for a bright nanotube ($\sim$ 18000 photons), the lateral precision is $<$ 10 nm, whereas both precision and accuracy in z are $\sim$ 20 - 40 nm for a 1 μm depth of field. Besides, we have characterized the setup performance as a function of the number of detected photons. We have concluded that the resolution depends on the inverse square root of the photon budget as it is expected by shot noise limited detection [65].

Results on 3D single-particle tracking (SPT) with carbon nanotubes are also presented in this chapter. We started with 3D SPT in glycerol-water mixture, which is an isotropic medium. We have recorded 3D trajectories, and we have demonstrated that, as expected, SWCNTs follow a isotropic motion when diffusing in isotropic media by calculating the mean square displacement of each trajectory in the three directions: x, y, and z. This result demonstrates the robustness of SELFI as a 3D super-resolution technique for 3D SPT applications. We also tested SELFI on 3D SPT of SWCNTs in anisotropic media, such as agarose gels. With SELFI, we have been able to identify some channel structures of agarose gel by tracking the motion of nanotubes trapped in these channels with resolutions up to 40 nm in z.

Our initial goal was to perform 3D SPT of biocompatible SWCNTs in the brain extracellular space (ECS) of organotypic brain slices. Due to the photostability of nanotubes, we have been able to acquire movies up to 9 minutes long at depths going from 9 μm to 66 μm inside the brain slices. Therefore, we have reconstructed 3D trajectories of nanotubes diffusing inside intact brain ECS. These pioneering results open up interesting possibilities to study the morphology, spatial distribution, and dynamical properties of intact biological structures in 3D.

Annexes
Calculation of vectorial point spread function in conjunction with self-interference

In the present chapter, we propose a theoretical description of the vectorial point spread function (PSF) of a point-like fluorescent emitter when observed through SELFI optical setup. Unlike section 1.1.3, this study allows us to have a better theoretical understanding on how the diffraction grating (DG) affects the PSF distribution.

In the first section, we start by describing the different parts that conform the SELFI PSF function. In the second section, we explain how to retrieve the PSF in the image space, i.e. the PSF that would be detected by the camera through wave propagation.

Theoretical model for high aperture PSF

The aim of this section is to find a theoretical equation that describes a PSF with and without passing through a DG. We should keep in mind that a PSF is nothing more than the light of an emitter interacting with the different parts of an optical setup. A PSF can be defined at any point in space, however, to have a PSF that represents an image caught in a detector, it has to be calculated at the focal plane.

To start, let's consider the image of a single emitter formed at the exit focal plane of the microscope, Fig.3.40. Here, $\mathbf{x} = (x, y, z)$ represents the focal region coordinates, and $\mathbf{m} = (m, n, s)$ are the pupil coordinates. The vectorial amplitude of the PSF ($\mathbf{E}(\mathbf{x})$) at the exit focal plane can be written as the inverse Fourier transform ($\mathcal{F}^{-1}$) of the axial projection of the forward propagation component of the complex vectorial pupil function, ($\mathbf{P}_+(m, n, \mathbf{x})$), as portrayed in Eq.3.10 [139].

$$\mathbf{E}(\mathbf{x}) = \mathcal{F}^{-1}\{\mathbf{P}_+(m, n, \mathbf{x})\} \tag{3.10}$$

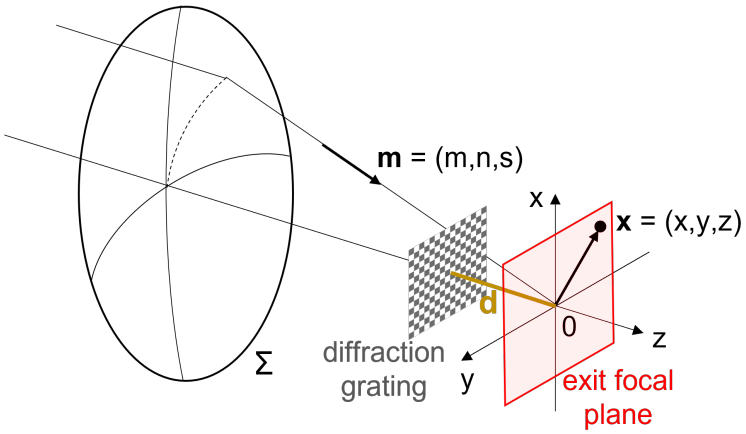

Figure 3.40: Diagram of the light focused in the exit focal plane of a microscope. **x** and **m** represent the focal region and pupil systems of coordinates, respectively.c

Considering the refractive index as constant in the focal region, from the Helmholtz equation for an homogeneous medium we can determine that the pupil function has non-zero values only on the surface of a sphere of radius $k = 2\pi/\lambda$, called Σ in Fig.3.40. Therefore, the integrals within the inverse Fourier transform of Eq.3.10 are calculated on Σ,

$$\mathbf{E}(\mathbf{x}) = -\frac{ik}{2\pi}\iint_{\Sigma} s_{+}\mathbf{P}_{+}(m,n,\mathbf{x})\exp\left(ik\mathbf{m}_{+}\cdot\mathbf{x}\right)dm\,dn, \tag{3.11}$$

where $\mathbf{m}_{+} = (m,n,s_{+})$, $s_{+} = \sqrt{1-l^2}$ when k is normalized to 1, and $l = \sqrt{m^2+n^2}$.

In the modelization of the pupil function, we introduce polarization ($\mathbf{a}(m,n)$), apodisation ($S(m,n)$), defocus ($T_d(m,n,z)$), and the transmittance function of the DG ($T(x,y)$) in the case of SELFI. Otherwise, we shall remove $T(x,y)$ from the equation. The vectorial pupil function for SELFI is therefore written as shown in Eq.3.12.

$$\mathbf{P}_{+}(m,n,\mathbf{x}) = \frac{1}{s_{+}}\mathbf{a}(m,n)S(m,n)T_d(m,n,z)T(x,y) \tag{3.12}$$

The vectorial pupil function describes how a lens alters the incident field's polarization, the complex value of any amplitude or phase filters across the aperture, and any additional aberrations in the lens' focusing behavior that differ from what results in a perfectly spherical wavefront convergent on the focal point [139]. Suppose the case of an incident light which is plane-polarised along the x axis, its vectorial strength function is written as follows [140–142]:

$$\mathbf{a}(m,n) = \begin{pmatrix} \left(m^2 s_{+} + n^2\right)/l^2 \\ -mn\left(1-s_{+}\right)/l^2 \\ -m \end{pmatrix}$$

Usually, microscope objectives are designed to obey the sine condition, giving aplanatic imaging [143], for which the apodisation is written as

$$S(m,n) = \sqrt{s_+}.$$

Defocus is equivalent to an axial shift, say z, of the point source being imaged relative to the focal point. A z translation of the PSF in the real space corresponds to a linear phase shift in the 3D pupil function. Thefore, the defocus function in the pupil space is written as

$$T_d(m,n,z) = \exp\left(i\,2\pi\,z s_+\right).$$

The transmittance function of the DG has already been explained in section 1.1.3 of this thesis. Let's recall it as

$$T(x,y) = \exp\left[i\pi\,\mathrm{rect}\left(\frac{x}{p}\right)\mathrm{rect}\left(\frac{y}{p}\right)\right]$$
$$\text{where} \quad \mathrm{rect}(\alpha) = \begin{cases} 1, & |\alpha| < \frac{1}{2}\bmod[1] \\ 0, & \text{else} \end{cases}.$$

By replacing all these functions in Eq.3.11, we obtain a full description of a self-interfered PSF.

PSF displacement from one plane to another

Once the SELFI PSF function is determined, it is important to understand how the PSF correlates from one plane in space to another. This process can be summarized as follows: we first calculate a standard PSF (no DG) in the exit focal plane, then move back to the plane where the DG is placed, introduce the transmittance function of the DG, and come back to the exit focal plane of the microscope. Prior to the mathematical explanation of this process, let's call d the distance between the DG and the exit focal plane. From Eq.3.10, the electromagnetic field of a PSF with no DG at the exit focal plane is given by the equation:

$$\mathbf{E}(x,y,0) = \mathcal{F}^{-1}\{\mathbf{P}_+(m,n,x,y,0)\},$$

while the electromagnetic field of a PSF at DG plane is given by

$$\mathbf{E}(x,y,-d) = \mathcal{F}^{-1}\{\mathbf{P}_+(m,n,x,y,-d)\}.$$

Through properties of the Fourier transform and inverse Fourier transform, we can determine the correlation between a standard PSF at the exit focal plane, and

the PSF at the DG plane that carries its interaction with the DG:

$$\begin{aligned}\mathbf{P}_+(m,n,x,y,d) &= \mathcal{F}\{\mathbf{E}(x,y,-d)\} \\ &= \mathbf{P}_+(m,n,x,y,0)\exp\left(-i\frac{2\pi}{\lambda}ds_+\right)\end{aligned}$$

Eq.3.13 represents the pupil function of a SELFI PSF at the exit focal plane of the microscope. By replacing this expression into Eq.3.10, we obtain the electromagnetic field of the SELFI PSF image that is detected by the camera.

$$\mathbf{P}_+(m,n,x,y,0) = \mathbf{P}_+(m,n,x,y,d)\exp\left(i\frac{2\pi}{\lambda}ds_+\right) \tag{3.13}$$

SELFI PSF simulation

We have used the equations presented in this annex to develop a program to simulate SELFI PSF images. In Fig.3.41, we show some of the results we have obtained when considering $\lambda = 980$ nm, $NA = 1.27$, $p = 10\mu$m, and a 20° inclination angle of the diffraction grating. Here, we observe how the PSF shape changes for different axial positions. In fact, the difference between positions -500 nm and $+500$ nm is very clear, as expected from SELFI images. This program can be modified to simulate optical setups with phase masks or other optical devices.

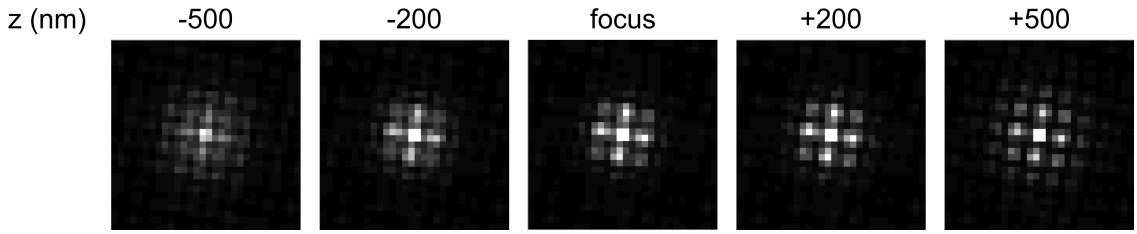

Figure 3.41: Simulated images of SELFI PSF. Parameters considered: $\lambda = 980$ nm, $NA = 1.27$, $p = 10\mu$m, and 20° inclination angle of the diffraction grating.

In future works, this description would be interesting to take into account polarization effects in high NA objectives.

Bibliography

[1] M. Sauer and M. Heilemann. Single-molecule localization microscopy in eukaryotes. *Chem. Rev.*, 117:7478–7509, 2017.

[2] Kim I. Mortensen, L. Stirling Churchman, James A. Spudich, and Henrik Flyvbjerg. Optimized localization analysis for single-molecule tracking and super-resolution microscopy. *Nature Methods*, 7:377–381, 2010.

[3] Antony Lee, Konstantinos Tsekouras, Christopher Calderon, Carlos Bustamante, and Steve Pressé. Unraveling the Thousand Word Picture: An Introduction to Super-Resolution Data Analysis. *Chem Rev.*, 117:7276–7330, 2017.

[4] S. Pujals, N. Feiner-Gracia, P. Delcanale, I. Voets, and L. Albertazzi. Super-resolution microscopy as a powerful tool to study complex synthetic materials. *Nat. Rev. Chem.*, 3:68–84, 2019.

[5] J. Feng, H. Deschout, S. Caneva, S. Hofmann, I. Lončarić, P. Lazić, and A. Radenovic. Imaging of optically active defects with nanometer resolution. *Nano Lett.*, 18:1739–1744, 2018.

[6] P. Delcanale, B. Miret-Ontiveros, M. Arista-Romero, S. Pujals, and L. Albertazzi. Nanoscale mapping functional sites on nanoparticles by points accumulation for imaging in nanoscale topography (PAINT). *ACS Nano*, 12:7629–7637, 2018.

[7] Miao Zhang, Martina Lihter, Tzu-Heng Chen, Michal Macha, Archith Rayabharam, Karla Banjac, Yanfei Zhao, Zhenyu Wang, Jing Zhang, Jean Comtet, Narayana R. Aluru, Magalí Lingenfelder, Andras Kis, and Aleksandra Radenovic*. Super-resolved optical mapping of reactive sulfur-vacancies in two-dimensional transition metal dichalcogenides. *ACS Nano*, 15:7168–7178, 2021.

[8] L. Cognet, D. A. Tsyboulski, and R. B. Weisman. Subdiffraction far-field imaging of luminescent single-walled carbon nanotubes. *Nano Lett.*, 8:749–753, 2008.

[9] Pierre Bon, Jeanne Linarès-Loyez, Maxime Feyeux, Kevin Alessandri, Brahim Lounis, Pierre Nassoy, and Laurent Cognet. Self-interference 3D super-

resolution microscopy for deep tissue investigations. *Nature Methods*, 15:449–454, 2018.

[10] M. Rust, M. Bates, and X. Zhuang. Sub-diffraction-limit imaging by stochastic optical reconstruction microscopy (STORM). *Nat. Methods*, 3:793–796, 2006.

[11] B. Huang, W. Wang, M. Bates, and X. Zhuang. Three-dimensional super-resolution reconstruction microscopy. *Science*, 319:810–813, 2008.

[12] E. Betzig, G. Patterson, R. Sougrat, O. Lindwasser, S. Olenych, J. Bonifacino, M. Davidson, J. Lippincott-Schwartz, and H. Hess. Imaging intracellular fluorescent proteins at nanometer resolution. *Science*, 313:1642–1645, 2006.

[13] S. Hess, T. Girirajan, and M. Mason. Ultra-high resolution imaging by fluorescence photoactivation localization microscopy. *Biophys. J.*, 91:4258–4272, 2006.

[14] A. G. York, A. Ghitani, A. Vaziri, M. W. Davidson, and H. Shroff. Confined activation and subdiffractive localization enables whole-cell PALM with genetically expressed probes. *Nat. Methods*, 8:327–333, 2011.

[15] C. Lin, R. Jungmann, A. M. Leifer, C. Li, D. Levner, G. M. Church, W.M. Shih, and P. Yin. Submicrometre geometrically encoded fluorescent barcodes self-assembled from DNA. *Nat. Chem.*, 4:832–839, 2012.

[16] N. Fakhri, F.C. MacKintosh, B. Lounis, L. Cognet, and M. Pasquali. Brownian motion of stiff filaments in a crowded environment. *Science*, 330:1804–1808, 2010.

[17] H. Shen, L. J. Tauzin, R. Baiyasi, W. Wang, N. Moringo, B. Shuang, and C. F. Landes. Single particle tracking: from theory to biophysical applications. *Chem. Rev.*, 117:7331–7376, 2017.

[18] S. Nandi, S. Parui, B. Jana, and K. Bhattacharyya. Local environment of organic dyes in an ionic liquid-water mixture: FCS and MD simulation. *J. Chem. Phys.*, 149:054501, 2018.

[19] S. Dominguez-Medina, S. Chen, J. Blankenburg, P. Swanglap, C. F. Landes, and S. Link. Measuring the hydrodynamic size of nanoparticles using fluctuation correlation spectroscopy. *Annu. Rev. Phys. Chem.*, 67:489–514, 2016.

[20] J. J. Neefjes and E. A. J. Reits. From fixed to FRAP: measuring protein mobility and activity in living cells. *Nat. Cell Biol.*, 3:E145–E147, 2001.

[21] G. J. Schütz, H. Schindler, and T. Schmidt. Single-molecule microscopy on model membranes reveals anomalous diffusion. *Biophys. J.*, 73:1073–1080, 1997.

[22] I. M. Peters, B. G. de Grooth, J. M. Schins, C. G. Figdor, and J. Greve. Three dimensional single-particle tracking with nanometer resolution. *Rev. Sci. Instrum.*, 69:2762–2766, 1998.

[23] C. A. Werley and W. E. Moerner. Single-molecule nanoprobes explore defects in spin-grown crystal. *J. Phys. Chem. B*, 110:18939–18944, 2006.

[24] A. Zürner, J. Kirstein, M. Döblinger, C. Bräuchle, and T. Bein. Visualizing single-molecule diffusion in mesoporous materials. *Nature*, 450:705–708, 2007.

[25] J. Kirstein, B. Platschek, C. Jung, R. Brown, T. Bein, and C. Bräuchle. Exploration of nanostructured channel systems with single-molecule probes. *Nat. Mater.*, 6:303–310, 2007.

[26] M. B. J. Roeffaers, B. F. Sels, H. Uji-i, F. C. De Schryver, P. A. Jacobs, D. E. De Vos, and J. Hofkens. Spatially resolved observation of crystal-face-dependent catalysis by single turnover counting. *Nature*, 439:572–575, 2006.

[27] N. Fakhri, A. D. Wessel, C. Willms, M. Pasquali, D. R. Klopfenstein F. C. MacKintosh, and C. F. Schmidt. High-resolution mapping of intracellular fluctuations using carbon nanotubes. *Science*, 344:1031–1035, 2014.

[28] Antoine G. Godin, Juan A. Varela, Zhenghong Gao, Noémie Danné, Julien P. Dupuis, Brahim Lounis, Laurent Groc, and Laurent Cognet. Single-nanotube tracking reveals the nanoscaleorganization of the extracellular space in thelive brain. *Nature Nanotechnology*, 12, 2017.

[29] S. Hrabetova, L. Cognet, D. A. Rusakov, and U. V. Nägerl. Unveiling the extracellular space of the brain: from super-resolved microstructure to in vivo function. *J. Neurosc.*, 38:9355–9363, 2018.

[30] Chiara Paviolo, Federico N. Soria, Joana S. Ferreira, Antony Lee, Laurent Groc, Erwan Bezard, and Laurent Cognet. Nanoscale exploration of the extracellular space in the live brain by combining single carbon nanotube tracking and super-resolution imaging analysis. *Methods*, 174, 2020.

[31] Federico N. Soria, Chiara Paviolo, Evelyne Doudnikoff, Marie-Laure Arotcarena, Antony Lee, Noémie Danné, Amit Kumar Mandal, Philippe Gosset, Benjamin Dehay, Laurent Groc, Laurent Cognet, and Erwan Bezard. Synucleinopathy alters nanoscale organization and diffusion in the brain extracellular space through hyaluronan remodeling. *Nat Commun*, 11, 2020.

[32] Chiara Paviolo and Laurent Cognet. Near-infrared nanoscopy with carbon-based nanoparticles for the exploration of the brain extracellular space. *Neurobiology of Desease*, 153:105328, 2021.

[33] M. Bourdenx, A. Nioche, S. Dovero, M. L. Arotcarena, S. Camus, G. Porras, M. L. Thiolat, N. P. Rougier, A. Prigent, P. Aubert, and et al. Identification of distinct pathological signatures induced by patient-derived α-synuclein structures in nonhuman primates. *Sci. Adv.*, 6:eaaz9165, 2020.

[34] B. Dong, B. T. Soetikno, X. Chen, V. Backman, C. Sun, and H. F. Zhang. Parallel three-dimensional tracking of quantum rods using polarization-sensitive spectroscopic photon localization microscopy. *ACS Photonics*, 4:1747–1752, 2017.

[35] D. Kim, Z. Zhang, and K. Xu. Spectrally resolved super-resolution microscopy unveils multipath reaction pathways of single spiropyran molecules. *J. Am. Chem. Soc.*, 139:9447–9450, 2017.

[36] J. Comtet, E. Glushkov, V. Navikas, J. Feng, V. Babenko, S. Hofmann, K. Watanabe, T. Taniguchi, and A. Radenovic. Wide-field spectral super-resolution mapping of optically active defects in hexagonal boron nitride. *Nano Lett.*, 19:2516–2523, 2019.

[37] Lexy von Diezmann, Yoav Shechtman, and W. E. Moerner. Three-dimensional localization of single molecules for super-resolution imaging and single-particle tracking. *Chem. Rev.*, 117:7244–7275, 2017.

[38] H.P. Kao and A.S. Verkman. Tracking of single fluorescent particles in three dimensions: use of cylindrical optics to encode particle position. *Biophysical Journal*, 67:1291–1300, 1994.

[39] Sri Rama Prasanna Pavani, Michael A. Thompson, Julie S. Biteen, Samuel J. Lord, Na Liu, Robert J. Twieg, Rafael Piestun, and W. E. Moerner. Three-dimensional single-molecule fluorescence imaging beyond the diffraction limit by using a double-helix point spread function. *Proceedings of the National Academy of Sciences*, 106:2995–2999, 2009.

[40] Bassam Hajj, Mohamed El Beheiry, Ignacio Izeddin, Xavier Darzacqbc, and Maxime Dahan. Accessing the third dimension in localizationbased super-resolution microscopy. *Phys. Chem. Chem. Phys.*, 16:16340, 2014.

[41] P. Prabhat, S. Ram, E. S. Ward, and R. J. Ober. Simultaneous imaging of different focal planes in fluorescence microscopy for the study of cellular dynamics in three dimensions. *IEEE Transactions on NanoBioscience*, 3:237–242, 2004.

[42] Sripad Ram, Prashant Prabhat, Jerry Chao, E. Sally Ward, and Raimund J. Ober. High accuracy 3D quantum dot tracking with multifocal plane microscopy for the study of fast intracellular dynamics in live cells. *Biophysical Journal*, 95:6025–6043, 2008.

[43] Gleb Shtengel, James A. Galbraith, Catherine G. Galbraith, Jennifer Lippincott-Schwartz, Jennifer M. Gillette, Suliana Manley, Rachid Sougrat, Clare M.Waterman, Pakorn Kanchanawong, Michael W. Davidson, Richard D. Fetter, and Harald F. Hess. Interferometric fluorescent super-resolution microscopy resolves 3D cellular ultrastructure. *Proceedings of the National Academy of Sciences*, 106:3125–3130, 2009.

[44] Stefan Hell and Ernst H.K. Stelzer. Fundamental improvement of resolution with a 4pi-confocal fluorescence microscope using two-photon excitation. *Optics Communications*, 93:277–282, 1992.

[45] Daniel Aquino, Andreas Schonle, Claudia Geisler, Claas v Middendorff, Christian A. Wurm, Yosuke Okamura, Thorsten Lang, Stefan W. Hell, and Alexander Egner. Two-color nanoscopy of three-dimensional volumes by 4pi detection of stochastically switched fluorophores. *Nature Methods*, 8:277–282, 2011.

[46] J. Deschamps, M. Mund, and J. Ries. 3D super-resolution microscopy by supercritical angle detection. *Opt. Express*, 22:29081–29091, 2014.

[47] N. Bourg, C. Mayet, G. Dupuis, T. Barroca P. Bon, S. Lecart, E. Fort, and S. Leveque-Fort. Direct optical nanoscopy with axially localized detection. *Nat. Photonic*, 9:587–593, 2015.

[48] Hans-Ulrich Dodt, Ulrich Leischner, Anja Schierloh, Nina Jahrling, Christoph Peter Mauch, Katrin Deininger, Jan Michael Deussing, Matthias Eder, Walter Zieglgansberger, and Klaus Becker. Ultramicroscopy: three-dimensional visualization of neuronal networks in the whole mouse brain. *Nature Methods*, 4, 2007.

[49] Fei Chen, Paul W. Tillberg, and Edward S. Boyden. Expansion microscopy. *Science*, 347:543–548, 2015.

[50] Douglas S. Richardson and Jeff W. Lichtman. Clarifying Tissue Clearing. *Cell*, 162:246–257, 2015.

[51] Juan A. Varela, Julien P. Dupuis, Laetitia Etchepare, Agnès Espana, Laurent Cognet, and Laurent Groc. Targeting neurotransmitter receptors with nanoparticles in vivo allows single-molecule tracking in acute brain slices. *Nat Commun*, 14, 2016.

[52] Amit Kumar Mandal, Xiaojian Wu, Joana S. Ferreira, Mijin Kim, Lyndsey R. Powell, Hyejin Kwon, Laurent Groc, YuHuang Wang, and Laurent Cognet. Fluorescent sp3 defect-tailored carbon nanotubes enable NIR-II single particle imaging in live brain slices at ultra-low excitation doses. *Sci Rep*, 10, 2020.

[53] Britton C. Near-infrared images using continuous, phase-modulated, and pulsed light with quantitation of blood and blood oxygenation. *Ann N Y Acad Sci*, 838:29–45, 1998.

[54] Kevin Welsher, Zhuang Liu, Sarah P. Sherlock, Joshua Tucker Robinson, Zhuo Chen, Dan Daranciang, and Hongjie Dai. A route to brightly fluorescent carbon nanotubes for near-infrared imaging in mice. *Nature Nanotech.*, 4:773–780, 2009.

[55] Steven L. Jacques. Optical properties of biological tissues: a review. *Phys. Med. Biol.*, 58:R37–R61, 2013.

[56] Laurent Cognet, Dmitri A. Tsyboulski, John-David R. Rocha, Condell D. Doyle, James M. Tour, and R. Bruce Weisman. Stepwise quenching of exciton fluorescence in carbon nanotubes by single-molecule reactions. *Science*, 316:1465–1468, 2007.

[57] Sofie Cambré, Silvia M. Santos, Wim Wenseleers, Ahmad R. T. Nugraha, Riichiro Saito, Laurent Cognet, and Brahim Lounis. Luminescence properties of individual empty and water-filled single-walled carbon nanotubes. *ACS Nano*, 6:2649–2655, 2012.

[58] Noémie Danné, Antoine G. Godin, Zhenghong Gao, Juan A. Varela, Laurent Groc, Brahim Lounis, and Laurent Cognet. Comparative Analysis of Photoluminescence and Upconversion Emission from Individual Carbon Nanotubes for Bioimaging Applications. *ACS Photonics*, 5:359–364, 2018.

[59] L. Rayleigh. Investigations in optics with special reference to the spectroscope. *Philos. Mag.*, 8:261–274, 1879.

[60] Colin J. R. Sheppard. The Development of Microscopy for Super-Resolution: Confocal Microscopy, and Image Scanning Microscopy. *Appl. Sci.*, 11, 2021.

[61] Takeo Ogama. A beginner's guide to improving image acquisition in fluorescence microscopy. *Biochem*, 42:22–27, 2020.

[62] A. G. Godin, B. Lounis, and L. Cognet. Super-resolution microscopy approaches for live cell imaging. *Biophys. J.*, 107:1777–1784, 2014.

[63] P. Padmanabhan, A. Kneynsberg, and J. Götz. Super-resolution microscopy: a closer look at synaptic dysfunction in Alzheimer disease. *Nat. Rev. Neurosci.*, 22:723–740, 2021.

[64] C.E. Shannon. Communication in the presence of noise. *Proceedings of the IRE*, 37:10–21, 1949.

[65] Russell E. Thompson, Daniel R. Larson, and Watt W. Webb. Precise nanometer localization analysis for individual fluorescent probes. *Biophys. J.*, 82:2775–2783, 2002.

[66] Rüdiger Paschotta. *Field guide to lasers*. SPIE Press, 2007.

[67] Jeff W. Lichtman and José-Angel Conchello. Fluorescence microscopy. *Nature Methods*, 2:910–919, 2005.

[68] Eugene Hecht. *Optics*. Pearson, 2017.

[69] A. Yu Meshalkin, V. V. Podlipnov, A. V. Ustinov, and E. A. Achimova. Analysis of diffraction efficiency of phase gratings in dependence of duty cycle and depth. *J. Phys.: Conf. Ser.*, 1368, 2019.

[70] I. H. Malitson. Interspecimen comparison of the refractive index of fused silica. *J. Opt. Soc. Am.*, 55:1205–1209, 1965.

[71] Sumio Iijima and Toshinari Ichihashi. Single-shell carbon nanotubes of 1-nm diameter. *Nature*, 363:603–605, 1993.

[72] D. S. Bethune, C. H. Kiang, M. S. de Vries, G. Gorman, R. Savoy, J. Vazquez, and R. Beyers. Cobalt-catalysed growth of carbon nanotubes with single-atomic-layer walls. *Nature*, 363:605–607, 1993.

[73] Michael J. O'Connell, Sergei M. Bachilo, Chad B. Huffman, Valerie C. Moore, Michael S. Strano, Erik H. Haroz, Kristy L. Rialon, Peter J. Boul, William H. Noon, Carter Kittrell, Jianpeng Ma, Robert H. Hauge, R. Bruce Weisman, and Richard E. Smalley. Band gap fluorescence from individual single-walled carbon nanotubes. *Science*, 297:593–596, 2002.

[74] Catalin D. Spataru, Sohrab Ismail-Beigi, Rodrigo B. Capaz, and Steven G. Louie. Theory and Ab Initio Calculation of Radiative Lifetime of Excitons in Semiconducting Carbon Nanotubes. *Phys. Rev. Lett.*, 95, 2005.

[75] Luigia Pezzi, Alfredo Pane, Ferdinanda Annesi, Maria Adele Losso, Alexa Guglielmelli, Cesare Umeton, and Luciano De Sio. Antimicrobial Effects of

Chemically Functionalized and/or Photo-Heated Nanoparticles. *Materials*, 12, 2019.

[76] Nikita Gupta, Shipra Mital Gupta, and S. K. Sharma. Carbon nanotubes: synthesis, properties and engineering applications. *Carbon Letters*, 29:419–447, 2019.

[77] Khurshed A. Shah and Bilal A. Tali. Synthesis of carbon nanotubes by catalytic chemical vapour deposition: A review on carbon sources, catalysts and substrates. *Materials Science in Semiconductor Processing*, 41:67–82, 2016.

[78] P. Nikolaev, M. J. Bronikowski, R. K. Bradley, F. Rohmund, D. T. Colbert, K. A. Smith, and R. E. Smalley. Gas-phase catalytic growth of single-walled carbon nanotubes from carbon monoxide. *Chemical Physics Letters*, 313:91–97, 1999.

[79] J. Liu, S. Fan, and H. Dai. Recent advances in methods of forming carbon nanotubes. *MRS Bulletin*, 29:244–250, 2004.

[80] M. Cinke, J. Li, B. Chen, A. Cassell, L. Delzeit, J. Han, and M. Meyyappan. Pore structure of raw and purified HiPco single-walled carbon nanotubes. *Chemical Physics Letters*, 365:69–74, 2002.

[81] D. E. Resasco, W. E. Alvarez, F. Pompeo, L. Balzano, J. E. Herrera, B. Kitiyanan, and A. Borgna. A scalable process for production of single-walled carbon nanotubes (SWNTs) by catalytic disproportionation of CO on a solid catalyst. *Journal of Nanoparticle Research*, 4, 2002.

[82] Feng Yang, Meng Wang, Daqi Zhang, Juan Yang, Ming Zheng, and Yan Li. Chirality pure carbon nanotubes: growth, sorting, and characterization. *Chem. Rev.*, 120:2693–2758, 2020.

[83] R. Saito, G. Dresselhaus, and M. S. Dresselhaus. *Physical properties of carbon nanotubes*. Imperial College Press, 1998.

[84] Ali Eatemadi, Hadis Daraee, Hamzeh Karimkhanloo, Mohammad Kouhi, Nosratollah Zarghami, Abolfazl Akbarzadeh, Mozhgan Abasi, Younes Hanifehpour, and Sang Woo Joo. Carbon nanotubes: properties, synthesis, purification, and medical applications. *Nanoscale Res Lett*, 9, 2014.

[85] C. Journet, W. K. Maser, P. Bernier, A. Loiseau, M. Lamy de la Chapelle, S. Lefrant, P. Deniard, R. Lee, and J. E. Fischer. Large-scale production of single-walled carbon nanotubes by the electric-arc technique. *Nature*, 388:756–758, 1997.

[86] Jean-Christophe Charlier, Xavier Blase, and Stephan Roche. Electronic and transport properties of nanotubes. *Reviews of Modern Physics*, 79:677–732, 2007.

[87] J. W. Mintmire and C. T. White. Universal density of states for carbon nanotubes. *Physical Review Letters*, 81:2506–2509, 1998.

[88] C. T. White and J. W. Mintmire. Density of states reflects diameter in nanotubes. *Nature*, 394:29–30, 1998.

[89] J. W. Mintmire, D. H. Robertson, and C. T. White. Properties of fullerene nanotubules. *Journal of Physics and Chemistry of Solids*, 54:1835–1840, 1993.

[90] R. Saito, G. Dresselhaus, and M. S. Dresselhaus. Trigonal warping effect of carbon nanotubes. *Physical Review B*, 61:2981–2990, 2000.

[91] S. M. Bachilo, M. S. Strano, C. Kittrell, R. H. Hauge, R. E. Smalley, and R. B. Weisman. Structure-assigned optical spectra of single-walled carbon nanotubes. *Science*, 298:2361–2366, 2002.

[92] J. W. Mintmire, B. I. Dunlap, and C. T. White. Are fullerene tubules metallic? *Physical Review Letters*, 68:631–634, 1992.

[93] N. Hamada, S. Sawada, and A. Oshiyama. New one-dimensional conductors: Graphitic microtubules. *Physical Review Letters*, 68:1579–1581, 1992.

[94] R. Saito, M. Fujita, G. Dresselhaus, and M. S. Dresselhaus. Electronic structure of chiral graphene tubules. *Applied Physics Letters*, 60:2204–2206, 1992.

[95] T. Ando. Excitons in Carbon Nanotubes. *Journal of the Physical Society of Japan*, 66:1066–1073, 1997.

[96] J. Maultzsch, R. Pomraenke, S. Reich, E. Chang, D. Prezzi, A. Ruini, E. Molinari, M. S. Strano, C. Thomsen, and C. Lienau. Exciton binding energies in carbon nanotubes from two-photon photoluminescence. *Physical Review B*, 72:241402, 2005.

[97] V. Perebeinos, J. Tersoff, and P. Avouris. Scaling of Excitons in Carbon Nanotubes. *Physical Review Letters*, 92:257402, 2004.

[98] Eduardo B. Barros, Rodrigo B. Capaz, Ado Jorio, Georgii G. Samsonidze, Antonio G. Souza Filho, Sohrab Ismail-Beigi, Catalin D. Spataru, Steven G. Louie, Gene Dresselhaus, and Mildred S. Dresselhaus. Selection rules for one- and two-photon absorption by excitons in carbon nanotubes. *Physical Review B*, 73:241406(R), 2006.

[99] Catalin D. Spataru, Sohrab Ismail-Beigi, Lorin X. Benedict, and Steven G. Louie. Excitonic effects and optical spectra of single-walled carbon nanotubes. *Physical Review Letters*, 92:077402, 2004.

[100] Robert S. Knox. *Theory of excitons.* Academic Press, 1963.

[101] Stéphane Berciaud, Laurent Cognet, and Brahim Lounis. Luminescence Decay and the Absorption Cross Section of Individual Single-Walled Carbon Nanotubes. *Phys. Rev. Lett.*, 101, 2008.

[102] O. N. Torrens, M. Zheng, and J. M. Kikkawa. Energy of K-momentum dark excitons in carbon nanotubes by optical spectroscopy. *Physical Review Letters*, 101, 2008.

[103] R. B. Weisman, S. Ghosh, and S. M. Bachilo. Advanced sorting of single-walled carbon nanotubes by nonlinear density-gradient ultracentrifugation. *Nature Nanotechnology*, 5:443–450, 2010.

[104] Jared Crochet, Michael Clemens, and Tobias Hertel. Quantum yield heterogeneities of aqueous single-wall carbon nanotube suspensions. *J. Am. Chem. Soc.*, 129:8058–8059, 2007.

[105] Gregory D. Scholes, Sergei Tretiak, Timothy J. McDonald, Wyatt K. Metzger, Chaiwat Engtrakul, Garry Rumbles, and Michael J. Heben. Low-Lying Exciton States Determine the Photophysics of Semiconducting Single Wall Carbon Nanotubes. *J. Phys. Chem. C*, 111:11139–11149, 2007.

[106] Vasili Perebeinos and Phaedon Avouris. Phonon and Electronic Nonradiative Decay Mechanisms of Excitons in Carbon Nanotubes. *Phys. Rev. Lett.*, 101, 2008.

[107] Shigeo Maruyama, Michael S. Arnold, Ralph Krupke, and Lian-Mao Peng. Physics and applications of nanotubes. *Journal of Applied Physics*, 131, 2022.

[108] Ming Zheng, Anand Jagota, Ellen D. Semke, Bruce A. Diner, Robert S. Mclean, Steve R. Lustig, Raymond E. Richardson, and Nancy G. Tassi. DNA-assisted dispersion and separation of carbon nanotubes. *Nature Materials*, 2:338–342, 2003.

[109] Naotoshi Nakashima, Shingo Okuzono, Hiroto Murakamiand Tonau Nakai, and Kenichi Yoshikawa. DNA dissolves single-walled carbon nanotubes in water. *Chem. Lett.*, 32:456–457, 2003.

[110] Kefu Fu, Weijie Huang, Yi Lin, Donghui Zhang, Timothy W. Hanks, Apparao M. Rao, and Ya-Ping Sun. Functionalization of carbon nanotubes with bovine serum albumin in homogeneous aqueous solution. *J. Nanosci. Nanotechnol.*, 2:457–461, 2002.

[111] Christopher A. Dyke and James M. Tour. Overcoming the insolubility of carbon nanotubes through high degrees of sidewall functionalization. *Chemistry – A European Journal*, 10:812–817, 2004.

[112] V. C. Moore, M. S. Strano, E. H. Haroz, R. H. Hauge, R. E. Smalley, J. Schmidt, and Y. Talmon. Individually suspended single-walled carbon nanotubes in various surfactants. *Nano Lett.*, 3:1379–1382, 2003.

[113] J. G. Duque, A. N. G. Parra-Vasquez, N. Behabtu, M. J. Green, A. L. Higginbotham, B. K. Price, A. D. Leonard, H. K. Schmidt, B. Lounis, J. M. Tour, S. K. Doorn, L. Cognet, and M. Pasquali. Diameter-dependent solubility of single-walled carbon nanotubes. *ACS Nano*, 4:3063–3072, 2010.

[114] Z. Liu, S. M. Tabakman, Z. Chen, and H. Dai. Preparation of carbon nanotube bioconjugates for biomedical applications. *Nat. Protocols*, 4:1372–1381, 2009.

[115] Zhenghong Gao, Juan A. Varela, Laurent Groc, Brahim Lounis, and Laurent Cognet. Toward the suppression of cellular toxicity from single-walled carbon nanotubes. *Biomater. Sci.*, 4:230–244, 2016.

[116] Christoph Bräuchle, Don Carroll Lamb, and Jens Michaelis. *Single particle tracking and single molecule energy transfer*. Wiley-VCH: Weinheim, 2009.

[117] L. S. Barak and W. W. Webb. Diffusion of low density lipoprotein-receptor complex on human fibroblasts. *J. Cell Biol.*, 95:846–852, 1982.

[118] J. Gelles, B. J. Schenapp, and M. P. Sheetz. Tracking kinesin-driven movements with nanometre-scale precision. *Nature*, 331:450–453, 1988.

[119] T. Schmidt, G. J. Schutz, W. Baumgartner, H. J. Gruber, and H. Schindler. Imaging of single molecule diffusion. *Proc. Natl. Acad. Sci. U. S. A.*, 93:2926–2929, 1996.

[120] M. J. Saxton and K. Jacobson. Single-particle tracking: applications to membrane dynamics. *Annu. Rev. Biophys. Biomol. Struct.*, 26:373–399, 1997.

[121] A. Kusumi, T. A. Tsunoyama, K. M. Hirosawa, and R. S. Kasai. Tracking single molecules at work in living cells. *Nat. Chem. Biol.*, 10:524–532, 2014.

[122] P. P. Mathai, J. A. Liddle, and S. M. Stavis. Optical tracking of nanoscale particles in microscale environments. *Appl. Phys. Rev.*, 3, 2016.

[123] J. Deich, E. M. Judd, H. H. McAdams, and W. E. Moerner. Visualization of the movement of single histidine kinase molecules in live Caulobacter cells. *Proc. Natl. Acad. Sci. U. S. A.*, 101:15921–15926, 2004.

[124] L. Niu and P. Yu. Investigating intracellular dynamics of FtsZ Cytoskeleton with photoactivation single-molecule tracking. *Biophys. J.*, 95:2009–2016, 2008.

[125] S. Manley, J. M. Gillette, G. H. Patterson, H. Shroff, H. F. Hess, E. Betzig, and J. Lippincott-Schwartz. High-density mapping of single-molecule trajectories with photoactivated localization microscopy. *Nat. Methods*, 5:155–157, 2008.

[126] Marija Vrljic, Stefanie Y. Nishimura, and W. E. Moerner. *Single-molecule tracking. In Lipid Rafts.* Humana Press, 2009.

[127] Antony Lee and Laurent Cognet. Length measurement of single-walled carbon nanotubes from translational diffusion and intensity fluctuations. *Journal of Applied Physics*, 128, 2020.

[128] N. Fakhri, D. A. Tsyboulski, L. Cognet, R. B. Weisman, and M. Pasquali. Diameter-dependent bending dynamics of single-walled carbon nanotubes in liquids. *Proc. Natl. Acad. Sci. U.S.A.*, 106:14219–14223, 2009.

[129] Xavier Michalet. Mean square displacement analysis of single-particle trajectories with localization error: Brownian motion in isotropic medium. *Phys Rev E Stat Nonlin Soft Matter Phys*, 82, 2010.

[130] Jason E. Riggs, Zhixin Guo, David L. Carroll, and Ya-Ping Sun. Strong Luminescence of Solubilized Carbon Nanotubes. *J. Am. Chem. Soc.*, 122:5879–5880, 2000.

[131] Zhenghong Gao, Laura Oudjedi, Romain Faes, Fabien Moroté, Christèle Jaillet, Philippe Poulin, Brahim Lounis, and Laurent Cognet. Optical detection of individual ultra-short carbon nanotubes enables their length characterization down to 10 nm. *Sci Rep*, 5:5879–5880, 2015.

[132] Y. Han, A. M. Alsayed, M. Nobili, J. Zhang, T. C. Lubensky, and A. G. Yodh. Brownian motion of an ellipsoid. *Science*, 314:626–630, 2006.

[133] Cara L. Croft and Wendy Noble. Preparation of organotypic brain slice cultures for the study of Alzheimer's disease. *F1000Res*, 15, 2018.

[134] C. L. Croft, H. S. Futch, B. D. Moore, and T. E. Golde. Organotypic brain slice cultures to model neurodegenerative proteinopathies. *Molecular Neurodegeneration*, 14, 2019.

[135] C. Humpel. Organotypic brain slices cultures: a review. *Neuroscience*, 305:86–98, 2015.

[136] Yasuhiro Mochizuki, Min Kyun Park, Takao Mori, and Seiichiro Kawashima. The difference in autofluorescence features of lipofuscin between brain and adrenal. *Zoological Science*, 12:283–288, 1995.

[137] Raju Tomer, Li Ye, Brian Hsueh, and Karl Deisseroth. Advanced CLARITY for rapid and high-resolution imaging of intact tissues. *Nature Protocols*, 9:1682–1697, 2014.

[138] R. Bruce Weisman and Sergei M. Bachilo. Dependence of Optical Transition Energies on Structure for Single-Walled Carbon Nanotubes in Aqueous Suspension: An Empirical Kataura Plot. *Nano Lett.*, 3:1235–1238, 2003.

[139] Matthew Arnison, Carol Cogswell, Colin Sheppard, and Peter Török. *Wavefront Coding Fluorescence Microscopy Using High Aperture Lenses*, pages 143–165. 2003.

[140] M. Mansuripur. Distribution of light at and near the focus of high-numerical aperture objectives. *J. Opt. Soc. Am. A*, 3:2086–2093, 1986.

[141] B. Richards and E. Wolf. Electromagnetic diffraction in optical systems II. Structure of the image field in aplanatic systems. *Proc. Roy. Soc. A*, 253:358–379, 1959.

[142] C. J. R. Sheppard and K. G. Larkin. Vectorial pupil functions and vectorial transfer functions. *Optik*, 107:79–87, 1997.

[143] H. H. Hopkins. The Airy disc formula for systems of high relative aperture. *Proc. Phys. Soc.*, 55, 1943.